

Washington University in St. Louis

## Washington University Open Scholarship

---

All Theses and Dissertations (ETDs)

---

1-1-2011

### Through-the-Wall Imaging and Multipath Exploitation

Marija Nikolic

*Washington University in St. Louis*

Follow this and additional works at: <https://openscholarship.wustl.edu/etd>

---

#### Recommended Citation

Nikolic, Marija, "Through-the-Wall Imaging and Multipath Exploitation" (2011). *All Theses and Dissertations (ETDs)*. 626.

<https://openscholarship.wustl.edu/etd/626>

This Dissertation is brought to you for free and open access by Washington University Open Scholarship. It has been accepted for inclusion in All Theses and Dissertations (ETDs) by an authorized administrator of Washington University Open Scholarship. For more information, please contact [digital@wumail.wustl.edu](mailto:digital@wumail.wustl.edu).

WASHINGTON UNIVERSITY IN ST. LOUIS

School of Engineering and Applied Science  
Department of Electrical & Systems Engineering

Dissertation Examination Committee:

Dr. Arye Nehorai, Chair

Dr. Mark Anastasio

Dr. Martin Arthur

Dr. Hiro Mukai

Dr. Joseph O'Sullivan

Dr. Lihong Wang

Through-the-Wall Imaging and Multipath Exploitation

by

Marija Nikolic

A dissertation presented to the Graduate School of Arts and Sciences  
of Washington University in partial fulfillment of the  
requirements for the degree of

DOCTOR OF PHILOSOPHY

December 2011

Saint Louis, Missouri

# **Abstract**

Through-the-Wall Imaging and Multipath Exploitation

by

Marija Nikolic

Doctor of Philosophy in Electrical Engineering

Washington University in St. Louis, December 2011

Research Advisor: Dr. Arye Nehorai

We consider the problem of using electromagnetic sensing to estimate targets in complex environments, such as when they are hidden behind walls and other opaque objects. The often unknown electromagnetic interactions between the target and the surrounding area, make the problem challenging. To improve our results, we exploit information in the multipath of the objects surrounding both the target and the sensors.

First, we estimate building layouts by using the jump-diffusion algorithm and employing

prior knowledge about typical building layouts. We also take advantage of a detailed physical model that captures the scattering by the inner walls and efficiently utilizes the frequency bandwidth.

We then localize targets hidden behind reinforced concrete walls. The sensing signals reflected from the targets are significantly distorted and attenuated by the embedded metal bars. Using the surface formulation of the method of moments, we model the response of the reinforced walls, and incorporate their transmission coefficients into the beamforming method to achieve better estimation accuracy.

In a related effort, we utilize the sparsity constraint to improve electromagnetic imaging of hidden conducting targets, assuming that a set of equivalent sources can be substituted for the targets. We derive a linear measurement model and employ  $l_1$  regularization to identify the equivalent sources in the vicinity of the target surfaces. The proposed inverse method reconstructs the target shape in one or two steps, using single-frequency data. Our results are experimentally verified.

Finally, we exploit the multipath from sensor-array platforms to facilitate direction finding. This in contrast to the usual approach, which utilizes the scattering close to the targets. We analyze the effect of the multipath in a statistical signal processing framework, and compute the Cramer-Rao bound to obtain the system resolution. We conduct experiments on a simple array platform to support our theoretical approach.

# Acknowledgements

I am sincerely grateful to my advisor, Dr. Arye Nehorai, for his valuable guidance throughout my doctoral research. I thank him for encouraging me to immerse in a research field that was completely new to me and leading me to interesting topics that I found truly exciting. I feel privileged to be a part of his excellent research group.

I am very thankful to Dr. Antonije Djordjevic from University of Belgrade, Serbia for his support and many useful discussions in my research.

I would like to thank my dissertation committee members, Dr. Joseph A. O'Sullivan, Dr. Martin R. Arthur, Dr. Hiro Mukai, Dr. Lihong Wang, and Dr. Mark Anastasio, for care-fully revising and providing constructive comments to this dissertation. I especially thank James Ballard for his editorial suggestions on this dissertation.

My sincere gratitude goes to my instructors, including Dr. Dibyen Majumdar, Dr. Dan Schonfeld, and Dr. Rashid Ansari from University of Illinois at Chicago for helping me to build a strong background of my research work. I would also like to thank all the staff members of the Preston M. Green Electrical & Systems Engineering Department at Washington University for their time and help.

I convey my heartiest thanks and warm regards to all my past and present labmates. Because of them, our lab was not only a place for research but also a place for fun and friendship. I am also thankful to my friends from Chicago and Saint Louis for making this a wonderful period of my life.

I offer my deepest gratitude to my parents and family in Serbia for their endless love and support. This dissertation is dedicated to them.

Marija Nikolic

*Washington University in Saint Louis,  
December 2011*

# Contents

<b>Abstract</b> .....	<b>ii</b>
<b>Acknowledgements</b> .....	<b>iv</b>
<b>List of Tables</b> .....	<b>viii</b>
<b>List of Figures</b> .....	<b>ix</b>
<b>List of Abbreviations</b> .....	<b>xiv</b>
<b>List of Notations</b> .....	<b>xv</b>
<b>Chapter 1 Introduction</b> .....	<b>1</b>
1.1 Background .....	1
1.2 Estimating Building Layouts .....	3
1.3 Estimating Targets Hidden behind Reinforced Concrete Walls .....	4
1.4 Estimating Hidden PEC Targets Using Sparsity .....	6
1.5 Estimating Direction of Arrival Using Multipath from Array Platforms .....	8
1.6 Dissertation Outline .....	10
<b>Chapter 2 Forward Electromagnetic Modeling</b> .....	<b>11</b>
2.1 Introduction.....	11
2.2 Surface Equivalence Theorem .....	11
2.3 Electric Field Integral Equation .....	15
2.4 Numerical Solution .....	16
2.5 Matrix Parameters .....	19
<b>Chapter 3 Estimating Building Layouts Using Jump-Diffusion Algorithm</b> .....	<b>21</b>
3.1 Introduction.....	21
3.2 Electromagnetic Modeling.....	22
3.3 Jump-Diffusion Algorithm.....	23
3.4 Measurement Model .....	26
3.5 Multiple-Frequency Approach.....	27
3.6 Numerical Results.....	30
3.7 Summary .....	36
<b>Chapter 4 Estimating Targets behind Reinforced Concrete Walls</b> .....	<b>38</b>
4.1 Introduction.....	38

4.2	Electromagnetic Model.....	39
4.3	Measurement Model .....	40
4.4	Estimating Wall Parameters.....	41
4.5	Estimating Target Positions .....	44
4.5.1	Unknown Bar Parameters.....	45
4.5.2	Known Bar Parameters .....	46
4.6	Results.....	48
4.6.1	Unknown Bar Parameters.....	50
4.6.2	Known Bar Parameters .....	52
4.7	Summary .....	58
<b>Chapter 5 Electromagnetic Imaging of Hidden 2D PEC Targets Using Sparse Signal Modeling.....</b>		<b>60</b>
5.1	Introduction.....	60
5.2	Electromagnetic Modeling.....	63
5.3	Sparse Signal Processing .....	66
5.3.1	Measurement Model .....	66
5.3.2	Current Distribution Model .....	69
5.3.3	Single Step Algorithm.....	72
5.3.4	Two-Step Algorithm .....	73
5.4	Numerical Experiments .....	77
5.4.1	One-Step Estimation .....	77
5.4.2	Two-Step Estimation.....	90
5.5	Experiment.....	97
5.5.1	Theoretical Model.....	97
5.5.2	Inverse Method.....	100
5.6	Summary .....	106
<b>Chapter 6 Estimating Direction of Arrival Using Multipath from Array Platforms .....</b>		<b>108</b>
6.1	Introduction.....	108
6.2	Measurement Model .....	109
6.3	Electromagnetic Model.....	112
6.4	Cramer-Rao Bound .....	114
6.5	DOA Estimation.....	117
6.5.1	Single Source.....	119
6.5.2	Two sources.....	123
6.6	Experiment.....	126
6.7	Summary .....	132
<b>Chapter 7 Conclusions.....</b>		<b>134</b>
7.1	Contributions.....	134
7.2	Future work.....	136
<b>Appendix.....</b>		<b>138</b>

<b>References</b> .....	<b>141</b>
<b>Vitae</b> .....	<b>158</b>



# List of Tables

TABLE I Computational times of inverse algorithms .....	90
TABLE II Probability distributions for transformations. ....	140

# List of Figures

Fig. 2.1:	Cross-section of a 2D electromagnetic system. ....	12
Fig. 2.2:	Application of the equivalence theorem (a) exterior problem and (b) interior problem. ....	14
Fig. 3.1:	Building layout and the four-sensor array. ....	22
Fig. 3.2:	Merge transformation.....	24
Fig. 3.3:	(a) First step: $f_1 = 10\text{MHz}$ , 400 iterations, (b) second step: $f_1 = 10\text{MHz}$ , $f_2 = 100\text{ MHz}$ , 200 iterations, (c) third step: $f_1 = 10\text{MHz}$ , $f_2 = 100\text{ MHz}$ , $f_3 = 200\text{ MHz}$ , 100 iterations. The results are shown jointly for 10 independent simulations. The wall permittivity is $3-j0.45$ . ....	33
Fig. 3.4:	(a) First step: $f_1 = 10\text{MHz}$ , $f_2 = 50\text{MHz}$ , 400 iterations, (b) second step: $f_1 = 10\text{MHz}$ , $f_2 = 50\text{MHz}$ , $f_3 = 100\text{ MHz}$ , 200 iterations, (c) third step: $f_1 = 10\text{MHz}$ , $f_2 = 50\text{MHz}$ , $f_3 = 100\text{ MHz}$ , $f_4 = 150\text{ MHz}$ , 100 iterations. The results are shown jointly for 10 independent simulations. The wall permittivity is $3-j0.45$ . ....	33
Fig. 3.5:	(a) First step: $f_1 = 50\text{MHz}$ , 400 iterations, (b) second step: $f_1 = 50\text{MHz}$ , $f_2 = 100\text{ MHz}$ , 300 iterations, (c) third step: $f_1 = 50\text{MHz}$ , $f_2 = 100\text{ MHz}$ , $f_3 = 150\text{ MHz}$ , 200 iterations. The wall permittivity is $\epsilon_r = 7 + 15/(1 + j(f[\text{MHz}]/20)^{0.7})$ . ....	34
Fig. 3.6:	(a) Estimation with erroneous wall thickness: true and assumed values are 0.2 m and 0.15 m, respectively. The third-step estimate, $f_1 = 10\text{MHz}$ , $f_2 = 50\text{MHz}$ , $f_3 = 100\text{ MHz}$ , and $f_4 = 150\text{ MHz}$ . (b) Estimation with erroneous wall permittivity: true and assumed values are $3-j0.45$ and $3.45-j0.55$ , respectively. The second-step estimate, $f_1 = 10\text{MHz}$ , $f_2 = 50\text{MHz}$ , and $f_3 = 75\text{ MHz}$ .....	35
Fig. 4.1:	Cross section of the reinforced concrete wall. ....	40

Fig. 4.2:	Scheme used for (a) wall-permittivity estimation and (b) wall-thickness permittivity estimation.....	42
Fig. 4.3:	Target position estimation.....	45
Fig. 4.4:	Numerical calculation of the wall transmission coefficients. ....	47
Fig. 4.5:	Estimation of wall thickness: correlation of focused electric field and reference pulse.....	50
Fig. 4.6.	Scene consisting of two metal targets (circles) placed behind the reinforced wall and clutter objects (rectangles). Image was computed using $\epsilon_r = 3$ , $f_0 = 0$ , and (a) $w = 0.2$ (real wall thickness) and (b) $w = 0.3$ (erroneous wall thickness). The waveform distortion was not taken into account. The adopted <i>SNR</i> was 30 dB. ....	52
Fig. 4.7:	Scene consisting of two metal targets (circles) placed behind the reinforced wall and clutter objects (rectangles). Image was computed using $\epsilon_r = 3$ , $f_0 = 0$ , and (a) $w = 0.2$ (real wall thickness) and (b) $w = 0.3$ (erroneous wall thickness). The waveform distortion was taken into account. The rebar period ( $d_{\text{bar}} = 0.15$ m) was assumed to be known. The adopted <i>SNR</i> was 30 dB.....	53
Fig. 4.8:	Scene consisting of two metal targets (circles) placed behind the reinforced wall and clutter objects (rectangles). Image was computed for <i>SNR</i> = 10 dB, $\epsilon_r = 3$ , $w = 0.2$ , $d_{\text{bar}} = 0.15$ m, and $f_0 = 0$ . The waveform distortion was (a) taken into account, and (b) not taken into account.....	54
Fig. 4.9:	Scene consisting of two metal targets (circles) placed behind the reinforced wall and clutter objects (rectangles). Image was computed for <i>SNR</i> = 10 dB, $\epsilon_r = 3$ , $w = 0.2$ , $d_{\text{bar}} = 0.15$ m, and (a) $f_0 = 0.5$ GHz and (b) and $f_0 = 1$ GHz. The waveform distortion was not taken into account. ....	55
Fig. 4.10:	Scene consisting of two metal targets (circles) placed behind the reinforced wall and clutter objects (rectangles). Image was computed for <i>SNR</i> = 15 dB, $\epsilon_r = 3$ , $w = 0.2$ , $d_{\text{bar}} = 0.1$ m, and $f_0 = 0.75$ GHz. The waveform distortion was (a) taken into account, and (b) not taken into account. ....	56
Fig. 4.11:	Scene consisting of two metal targets (circles) placed behind the reinforced wall and clutter objects (rectangles). Image was computed for <i>SNR</i> = 20 dB, $\epsilon_r = 3$ , $w = 0.2$ , $d_{\text{bar}} = 6$ cm, and $f_0 = 1$ GHz. The waveform distortion was (a) taken into account, and (b) not taken into account.....	57

Fig. 4.12:	Scene consisting of two metal targets (circles) placed behind the reinforced wall and clutter objects (rectangles). Image was computed for $SNR = 10$ dB, $\epsilon_r = 3$ , $w = 0.2$ , $d_{\text{bar}} = 15$ cm, and $f_0 = 0$ GHz. Waveform distortion was modeled using an erroneous bar period ( $d_{\text{bar}} = 10$ cm). . . . .	58
Fig. 5.1:	(a) Hidden PEC objects inside dielectric body and sensor array, (b) equivalent sources representing the target, and (c) grid of equivalent sources. . . . .	61
Fig. 5.2:	Equivalence theorem: (a) exterior problem and (b) interior problem. . . . .	64
Fig. 5.3:	Reconstruction of cross-like cylinder (“noiseless” model). Results were computed using (a) $\gamma^{(1)} = 1.4$ , (b) $\gamma^{(1)} = 1.8$ , and (c) $\gamma^{(1)} = 2$ . . . . .	78
Fig. 5.4:	(a) L-curve and (b) $l_0$ -curve for target of Fig. 5.3. . . . .	81
Fig. 5.5:	Reconstruction of cross-like cylinder computed using (a) LSM and (b) MUSIC. “Noiseless” model. . . . .	84
Fig. 5.6:	Reconstruction of cross-like cylinder computed using (a) sparse signal processing and (b) MUSIC for $SNR = 20$ dB. . . . .	84
Fig. 5.7:	Reconstruction of two metallic targets computed using (a) sparse signal processing ( $\gamma^{(1)} = 1.4$ , $L = 21^2$ , $V = 1$ ), (b) MUSIC, and (c) LSM. “Noiseless” model. . . . .	86
Fig. 5.8:	Reconstruction of two metallic targets computed using (a) sparse signal processing ( $\gamma^{(1)} = 1.4$ , $L = 21^2$ , $V = 1$ ), (b) MUSIC, and (c) LSM for $SNR = 10$ dB. . . . .	87
Fig. 5.9:	Reconstruction of two star-shaped cylinders computed using (a) single-step sparse processing ( $\gamma^{(1)} = 1.4$ , $L = 32^2$ , $V = 4$ ), (b) LSM, (c) and MUSIC for $SNR = 20$ dB. . . . .	89
Fig. 5.10:	Reconstruction of U-shaped target computed using single-step sparse processing for (a) $\gamma^{(1)} = 1.4$ , $L = 21^2$ , $V = 1$ and (b) $\gamma^{(1)} = 1.8$ , $L = 21^2$ , $V = 1$ ( $SNR = 20$ dB). . . . .	91
Fig. 5.11:	Reconstruction of U-shaped target computed using two-step sparse processing for $\gamma^{(1)} = 1.8$ , $L = 21^2$ , $V = 1$ and (a) $\gamma^{(2)} = 1.4$ and (b) $\gamma^{(2)} = 1.6$ ( $SNR = 20$ dB). . . . .	91

Fig. 5.12:	Reconstruction of U-shaped target computed using two-step sparse processing for $\gamma^{(1)} = 1.8$ , $\gamma^{(2)} = 1.4$ and (a) $L = 21^2, V = 1$ and (b) $L = 24^2, V = 3$ ( $SNR = 10$ dB). .....	92
Fig. 5.13:	Image of thick U-shaped cylinder computed using (a) LSM and (b) MUSIC ( $SNR = 20$ dB). .....	92
Fig. 5.14:	Image of thin U-shaped cylinder computed using (a) LSM, (b) MUSIC, and (c) two-step sparse processing ( $L = 24^2, V = 3$ ) for $SNR = 20$ dB. ....	94
Fig. 5.15:	Image of thin U-shaped cylinder computed using (a) LSM, (b) MUSIC, and (c) two-step sparse processing ( $L = 24^2, V = 3$ ) for $SNR = 10$ dB. ....	95
Fig. 5.16:	Reconstruction of thick U-shaped cylinder computed using erroneous dielectric permittivity ( $\epsilon_r = 3.3 - 0.33j$ ) in the two-step sparse algorithm for $\gamma^{(1)} = 1.8$ , $\gamma^{(2)} = 1.4$ , $SNR = 20$ dB, and (a) $L = 21^2, V = 1$ and (b) $L = 24^2, V = 3$ . .....	96
Fig. 5.17:	An example of a 2D electromagnetic system. ....	97
Fig. 5.18:	The equivalent 3D model of the electromagnetic system of Fig. 5.17. ....	98
Fig. 5.19:	The measurement setup. ....	99
Fig. 5.20:	Admittance parameter $\bar{Y}_{56}$ obtained by 2D simulation, 3D simulation, and measurements. ....	100
Fig. 5.21:	Reconstruction of the U-shape target using the system of Fig. 20. Results are obtained using (a) synthetic data and (b) measured data at $f = 1.2$ GHz for $\gamma^{(1)} = 1.4$ . ....	104
Fig. 5.22:	Reconstruction of the U-shape target using the system of Fig. 20. Results are obtained using (a) synthetic data and (b) measured data at $f = 1.1$ GHz for $\gamma^{(1)} = 1.4$ . ....	105
Fig 6.1:	Geometrical model of the Predator with the adopted coordinate system. We show the uniform linear array of monopoles mounted on the bottom of the UAV and the multipath due to the diffraction (black arrows). ....	113
Fig. 6.2:	Ratio of cross-polar and co-polar components of the radiation pattern of a sensor mounted on the UAV, computed using WIPL-D Pro at 1 GHz. ....	118

Fig. 6.3:	The lower bound for MSAE computed for a uniform linear array of seven monopoles mounted on the (a) Predator and (b) PEC using $N = 1$ frequency sample. The adopted $SNR$ is 15 dB.....	121
Fig. 6.4:	The lower bound for MSAE computed for a uniform linear array of seven monopoles mounted on the (a) Predator and (b) PEC using $N = 15$ frequency samples. The adopted $SNR$ is 15 dB. ....	121
Fig. 6.5:	Square root of MSAE for (a) $\theta = 50^\circ$ and (c) $\phi = 50^\circ$ . Results are obtained by 200 independent Monte Carlo simulations with $SNR = 15$ dB. ....	123
Fig. 6.6:	Square root of lower bound for MSAE of the first wave as a function of its DOA. The DOA of the second wave is $\theta_2 = \theta_1$ , $\phi_2 = \phi_1 + \delta$ , $\delta = 8^\circ$ . Computations are performed for the array of monopoles on the UAV with $SNR = 15$ dB and $N = 20$ .....	125
Fig. 6.7:	Resolution of the array of monopoles on the UAV computed by CRB and MDL with $SNR = 15$ dB and $N = 20$ .....	126
Fig. 6.8:	The receiving array on the plate and the adopted coordinate system. ....	127
Fig. 6.9:	The experimental verification of the 3D localization by means of diffraction. ( $\phi = 90^\circ$ , $\theta = 75^\circ$ ) was computed using single-frequency measurements at (a) 0.75 GHz, (b) 1 GHz, (c) 1.5 GHz, and (d) 2 GHz. ....	129
Fig. 6.10:	The experimental verification of the 3D localization by means of diffraction. ( $\phi = 45^\circ$ , $\theta = 75^\circ$ ) was computed using single-frequency measurements at (a) 0.75 GHz, (b) 1 GHz, (c) 1.5 GHz, and (d) 2 GHz. ....	130
Fig. 6.11:	The experimental verification of the 3D localization by means of diffraction. ( $\phi = 0^\circ$ , $\theta = 75^\circ$ ) was computed using single-frequency measurements at (a) 0.75 GHz, (b) 1 GHz, (c) 1.5 GHz, and (d) 2 GHz. ....	131
Fig. 6.12:	Diffacted rays and direct ray for DOA: (a) ( $\phi = 90^\circ$ , $\theta = 75^\circ$ ), (b) ( $\phi = 45^\circ$ , $\theta = 75^\circ$ ), and (c) ( $\phi = 0^\circ$ , $\theta = 75^\circ$ ). ....	132

# List of Abbreviations

2D	Two-dimensional
3D	Three-dimensional
DBIM	Distorted Born iterative method
DOA	Direction-of-arrival
GO	Geometrical optics
EFIE	Electric field integral equation
LSM	Linear Sampling Method
MDL	Minimum-description length
MLE	Maximum likelihood estimate
MoM	Method of moments
PEC	Perfect electric conductor
PO	Physical optics
RT	Ray tracing
SNR	Signal-to-noise ratio
TM	Transverse magnetic
UAV	Unmanned Aerial Vehicle

# List of Notations

$a$	lowercase italic denotes a scalar
$\mathbf{a}$	lowercase bold italic denotes a column-matrix (vector) $\mathbf{a} \in C^n$
$\mathbf{A}$	uppercase bold italic denotes a matrix $\mathbf{A} \in C^{m \times n}$
$ A $	determinant of $A$
$A(i, j)$	$(i, j)$ -th element of $A$
$\mathbf{a}(i)$	$i$ -th element of $\mathbf{a}$
$A^*$	conjugate of $A$
$A^H$	conjugate-transpose (Hermitian) of $A$
$\text{diag}(\dots)$	square matrix with non-zero entries on the main diagonal
$\text{blkdiag}(\dots)$	block-diagonal matrix with non-zero blocks on the main diagonal
$I_n$	identity matrix of dimension $n$
$\text{Re}\{\cdot\}$	real part of a complex quantity
$\text{Im}\{\cdot\}$	imaginary part of a complex quantity
$\ \cdot\ _0$	number of non-zero elements in a vector
$\ \cdot\ _p$	$p$ -th norm of a vector, $p = 1, 2$
$\mathbf{A}$	bold roman denotes a physical vector



# Chapter 1

## Introduction

### 1.1 Background

Estimating the location, number, and shape of hidden targets using electromagnetic sensing is an inverse scattering problem with many applications, such as in nondestructive testing, subsurface probing, and through-the-wall imaging. Solving this problem is difficult because of the complex and often unknown environment. In through-the-wall imaging, for example, the targets are located inside buildings of unknown layout and material. Sensor arrays receive signals which are distorted due to the electromagnetic interaction among the targets, unidentified walls, and furniture.

The unwanted scattering from nearby objects is usually considerably stronger than the back-scattered signals from the targets. In addition, the physical modeling of electrically large structures, such as buildings, is computationally intensive, thus limiting the practical aspects of the estimation. The estimation accuracy and the computational speed

are dictated by the operating frequency. Hence, efficient usage of the bandwidth is critical for real-life implementations. In a similar way, the useful scattering from a buried target is substantially disguised by the reflections at the interfaces of the embedding medium. The unwanted multiple reflections may also originate from the corners of the target itself. These multiple scattered signals introduce difficulties in the target imaging, causing artifacts in the reconstructed images. Yet, the electromagnetic interaction between the target and the environment contains data useful in inferring the target. The multipath from the objects surrounding the target, as well as from the sensor array, enlarges the illumination zone of the targets and increases the effective aperture of the array. The resultant electromagnetic field in the multipath environment changes rapidly with the frequency. This increased frequency sensitivity, compared to situations without the multipath, is useful in resolving the ambiguity of the inverse scattering problems.

Hence, the role of electromagnetic modeling in target estimation is twofold: to provide an accurate representation of the measurement scene and to extract additional pieces of information due to the multipath. In this dissertation, we address both aspects of electromagnetic sensing in the complex environments. We focus our work on the following examples: building layout estimation, identification of targets hidden behind reinforced concrete walls, buried target imaging, and exploitation of the multipath from sensing arrays.

## 1.2 Estimating Building Layouts

Estimating building layouts is an important task in urban warfare. If the positions of the inner walls have been previously revealed, the localization of humans or other objects hidden inside buildings is much facilitated. Moreover, the scattering of the transmitted signals inside the building provides additional “views” of the target that are helpful in the classification. Reconstruction of the building interior belongs to the broad area of inverse scattering. To solve this problem using purely electromagnetic (deterministic) tools is difficult because the investigated domain is very large in terms of wavelengths. At the same time, inner walls have some a-priori known information that we take advantage of [1], [2].

In general, procedures for solving inverse scattering problems can be classified into deterministic and stochastic. Among deterministic algorithms, many applications use iterative techniques based on the linearization around a current estimate [3]-[5]. Because the inverse scattering problems are intrinsically ill-posed [6]-[8], the reconstruction methods may diverge or converge to a false solution. A globally convergent stochastic algorithm for the inverse scattering based on simulated annealing is given in [9]. The algorithm of [9] is extremely time consuming, and cannot be applied for the estimation of electrically large structures such as buildings.

Here, we exploit the knowledge of typical building layouts to improve the estimation. Instead of dividing the unknown area into uniform cells with unknown properties [9], we consider more natural division into “walls” and “rooms.” We use a stochastic algorithm

that enables efficient inclusion of the prior knowledge – the jump-diffusion algorithm [10], [11]. Prior information reduces the parameter space, and consequently expedites the convergence. Jump-diffusion has been widely used for solving problems where the dimensionality of the parameter space is unknown. However, most of its applications lie in image processing, e.g., [12] and [13]. We adapt that algorithm to solve the inverse electromagnetic problem. At the same time, we take advantage of the detailed physical model that captures the multipath from the inner walls and efficiently utilizes the frequency bandwidth.

Works that exploit rectangular floor plans and employ graph theory to estimate the rooms are [14] and [15]. In [14], the solutions are generated via a Markov chain Monte Carlo procedure, whereas in [15] a constrained least squares approach is used.

### **1.3 Estimating Targets Hidden behind Reinforced Concrete Walls**

The goal of through-the-wall imaging is to find targets located behind opaque obstacles, using exterior electromagnetic sensing. There are many civilian and military applications that benefit from the research in this field, such as saving hostages and earthquake victims. The presence of the walls significantly influences the estimation process. If the walls are not included in the model, due to the refraction of the electromagnetic waves, the target estimates are delocalized from their true positions. In addition, only a fraction of the transmitted power reaches the targets because of the absorption and refraction

losses in the walls. The attenuation and dispersion of the transmitted waveforms are particularly pronounced in the case of the inhomogeneous walls, such as reinforced and cinder-block walls. The periodic structure of these walls poses significant difficulties in hidden target imaging. Typically, images are blurred with ghost target estimates.

In prior studies, the walls were treated as homogeneous dielectric slabs of known thickness and permittivity. In [16] and [17], a beamforming imaging scheme that accommodates the refractions from a single wall was presented. In [18] and [19], the linear Born model was applied to obtain the image of targets hidden inside the known building. The case in which the parameters of the homogeneous wall were unknown was tackled in [20]. Radar imaging through a wall made of cinder blocks was addressed in [21]. Recently, methods based on the compressive sensing were suggested for the through-the-wall imaging [22]-[25].

In this dissertation, we consider the estimation of targets hidden behind concrete walls reinforced by parallel steel bars [26]. Electromagnetic propagation through reinforced concrete walls is well covered in the literature for the purpose of mobile channel modeling [27]-[29]. Here, the goal is to take advantage of accurate electromagnetic modeling to improve imaging accuracy. We model the response of the reinforced walls using the surface formulation of the method of moments (MoM) [30], [31]. We investigate the cases of known and unknown wall parameters. To localize the targets, we incorporate the near-field transmission coefficients of the reinforced walls into the beamforming method. Significant improvement is achieved when the bar characteristics are taken into account. This improvement is particularly pronounced when the

signal-to-noise ratio is low.

## 1.4 Estimating Hidden PEC Targets Using Sparsity

Another important problem in inverse scattering is the estimation of conducting targets concealed inside a dielectric domain. The general algorithms for restoring dielectric profiles, such as the distorted Born iterative method (DBIM) and equivalent Gauss-Newton methods, are not suitable for the imaging of non-penetrable objects, due to the high contrast in the electromagnetic properties between the target and surroundings (e.g., [3]-[5]). The electric currents induced on the metallic targets are typically concentrated in small areas around the so-called scattering centers. These currents rapidly decrease towards the interior of the targets, due to the small penetration depth of conducting objects. Hence, the induced currents are sparse throughout the domain in which the targets are hidden. Herein, we study the utilization of a sparsity constraint ( $l_1$  regularization [32]-[40]) in the electromagnetic imaging of hidden conducting targets [42]-[44].

Algorithms used in the inverse scattering of perfect electrically conducting (PEC) targets include the following, among others. In the equivalent-source method [45]-[47], the metallic cylinders are replaced by equivalent sources whose locations and currents are unknown. The equivalent sources are restored iteratively, through a non-linear optimization process. If the targets are embedded in a dielectric medium, the volume

equivalence theorem is usually applied [48]. Examples of direct methods based on the volume formulation of the electric field integral equation are given in [49], [50]. Estimated volume equivalent currents are used as indicators of the target existence. The prominent non-iterative, single-frequency methods are linear sampling (LSM) [51]-[59] and MUSIC [60]-[66]. The advantages of LSM and MUSIC are the computational efficacy, straight-forward implementation, and applicability to both metallic and dielectric targets. The physical optics (PO) method is also widely used in high-frequency imaging of PEC targets [67]-[69]. However, the PO approximation neglects multiple scattering and therefore is typically associated with smooth-target imaging. There is also a group of model-based algorithms that iteratively estimate the parameterized contours of targets [70], [71]. Recently, sparse signal processing has been successfully applied in radar imaging (see e.g., [41] and references therein). Sparse localization of buried targets and targets behind walls was considered in [72] and [22]-[25], respectively. The underlying electromagnetic models assumed far-field measurements and point-like targets. The joint application of  $l_1$  and  $l_2$  regularizations with the DBIM algorithm was proposed in [73] for medical imaging purposes. This general estimation scheme restores the permittivity of the 3D domain with arbitrary heterogeneities. However, the DBIM algorithm does not converge for highly conductive scatterers such as metals, which we consider here.

We develop an inverse algorithm that is based on the equivalent-source method [45]-[47] and the surface formulation of the electric-field integral equation (EFIE) [30], [31]. We define a grid of the equivalent sources uniformly spread in the interior of the known

embedding medium. The currents of the equivalent sources are unknown. However, we suppose that there are only a few equivalent sources with non-zero currents, and that those equivalent sources are located close to the target contours. We derive a linear measurement model and employ  $l_1$  regularization to emphasize the equivalent sources in the vicinity of the target surfaces and thus provide information about their shape. The proposed inverse method allows reconstructing the target shape in one or two steps, using single frequency data. We verify our results experimentally.

## **1.5 Estimating Direction of Arrival Using Multipath from Array Platforms**

In the previous examples, the intricacy of estimation stems from the complex target environment. Moreover, sensors are often mounted on platforms which may be seen as a significant source of the scattering. We examine whether the scattering (multipath) from sensing systems alone can be exploited in target localization. This approach is in contrast to investigations in which the multipath from the target surroundings is utilized for improving the localization characteristics of sensing arrays [74]-[79]. Although the multipath from the sensors (to the best of our knowledge) has not been used in electromagnetic sensing, it holds great advantage over using the multipath close to the targets: the platform response is usually completely known, whereas the target environment is only partially known. A preliminary study [80] proved that placing ideal reflectors near an isotropic sensor lowered the variance of the DOA estimation.



Some examples of the exploitation of the multipath close to the targets include the following. In [74]-[79], the reflections from land or buildings are taken into account to improve source localization. The phenomenon of “super-resolution” in a complex propagation medium using phase conjugation and time reversal was studied in [81] and [82]-[84], respectively. In [85], it was demonstrated that the number of measurements needed for inferring the radiation pattern of a two-dimensional current source is reduced if the source is situated between two parallel plates instead of in a free space. Similar exploitation of propagation complexity and multipath has also been used in telecommunications, for example in [86].

We consider an example of a realistic airborne platform, the Unmanned Aerial Vehicle (UAV) Predator. We show here that exploiting the multipath from the sensing platforms allows estimating both azimuth and elevation of multiple unknown incident signals, even at a single frequency, which would otherwise be impossible with uniform linear arrays. A substantial body of previous work considered the performance of antenna (sensing) arrays in the presence of mounting structures [87]-[92]. These efforts typically went in two directions: reducing the interaction between the array and the platform, or optimizing the array pattern in the presence of the platform. In the first approach ([87], [88]), the maximum field level in the array’s surrounding was controlled by imposing the constraint that the electric field be zero for a suitable set of points. In the second group are algorithms (e.g., [89]-[92]) in which the influence of the platform is taken into account in the pattern synthesis and directivity optimization. Moreover, the results in [89]-[92] demonstrated that high-performance radiation patterns can be achieved by including the

presence of mounting platforms.

Unlike previous work that is focused on beamshaping in the presence of the platform, the present work aims to demonstrate the positive impact of the platform on DOA estimation. We study the effect of the multipath in the framework of statistical signal processing and compute the Cramer-Rao bound (CRB) to solve the theoretical resolution of the system. To determine the empirical resolution of the system, we use the maximum likelihood (ML) [93] and the minimum description length (MDL) [94]. Finally, we verify experimentally the proposed approach by considering a uniform linear array mounted on a finite plate.

## **1.6 Dissertation Outline**

The organization of the dissertation is as follows. In Chapter 2, we explain the physical model that we used throughout the thesis. We study the building layout estimation in Chapter 3. In Chapter 4, we investigate the localization of the targets behind reinforced walls. We describe the sparse estimation of buried targets and targets behind walls in Chapter 5. In Chapter 6, we examine the exploitation of the multipath from sensor platforms. Finally, in Chapter 7 we summarize our contributions and discuss some possible future work.

## Chapter 2

# Forward Electromagnetic Modeling

### 2.1 Introduction

In this chapter we describe the electromagnetic model that we have used in the thesis, with the exception of Chapter 6. We refer to the computation of the electromagnetic response of a completely known system as the forward electromagnetic problem. We consider two-dimensional (2D) electromagnetic systems, because the three-dimensional (3D) electromagnetic modeling of electrically large objects, such as buildings, is still inadmissibly time-consuming. However, if an efficient 3D analysis is feasible, it can be smoothly incorporated into the recognition procedures.

The computational model used in this thesis is based on the surface equivalence theorem and the method of moments (MoM).

### 2.2 Surface Equivalence Theorem

We consider an electromagnetic system that consists of  $N$  dielectric bodies placed in a vacuum. The dielectric bodies are made of linear homogenous materials. The

permittivity and permeability of the  $i$ th body are  $\varepsilon_i$  and  $\mu_i$ ,  $i = 1, \dots, N$ , respectively. Inside the dielectric bodies there may be hidden metallic objects. An example of the system that we study is depicted in Fig. 2.1.

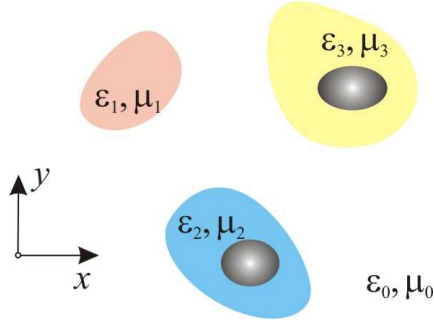


Fig. 2.1: Cross-section of a 2D electromagnetic system.

We model the excitation of the system by impressed electric fields. The impressed fields can exist only inside the bodies. We assume that the impressed fields are axial and independent of the  $z$ -coordinate. However, instead of directly specifying the impressed fields, we define the sources of these fields. The sources are uniform solenoidal magnetic currents, which wrap individual bodies. We denote the density of these currents by  $\mathbf{M}_{\text{si}}$ . If the cross-sectional dimensions of a body are small in terms of the wavelength, the impressed electric field is practically uniform within the body. As a result of the excitation, axial currents (electric currents and polarization currents), also independent of the  $z$ -coordinate, are induced in all bodies. The goal of the computations is to determine these currents and, subsequently, evaluate the electromagnetic fields they radiate.

In the numerical solution of this electromagnetic problem, we first homogenize the medium by means of the equivalence theorem [95]. The application of the equivalence

theorem is illustrated in Fig. 2.2. We denote the domain outside the bodies as the exterior region, the domains inside the bodies as the interior regions, and the boundary surfaces of the bodies as the interfaces. The electromagnetic field in the exterior region remains intact if we replace the bodies (along with the hidden objects inside) with equivalent surface electric and magnetic currents, whose densities are

$$\mathbf{J}_s = \mathbf{n} \times \mathbf{H}, \quad (2.1)$$

$$\mathbf{M}_s = -\mathbf{n} \times \mathbf{E}, \quad (2.2)$$

where  $\mathbf{J}_s$  is the vector of the equivalent surface electric currents,  $\mathbf{M}_s$  is the vector of the equivalent surface magnetic currents,  $\mathbf{H}$  is the magnetic-field vector at the interface,  $\mathbf{E}$  is the electric-field vector at the interface, and  $\mathbf{n}$  is the normal unit vector pointing outside the body. We consider the TM polarization; the electric currents are axial, and the magnetic currents are circumferential. The surface magnetic currents that are the sources of the impressed field ( $\mathbf{M}_{si}$ ), remain in the exterior region, on top of the equivalent currents.

In the equivalent system thus obtained, the electromagnetic field in all interior regions is zero. Hence, we can substitute the interior regions with an arbitrary medium, because this medium does not have any influence on the electromagnetic field. If we assume that a vacuum is inside the zero-field regions, we obtain an electromagnetic system with a homogeneous medium everywhere [95] (i.e., a vacuum). In this case, which we refer to as the exterior problem (Fig. 2.2a), the field sources are the surface electric and magnetic

currents on the bodies ( $\mathbf{J}_s, \mathbf{M}_s$ ).

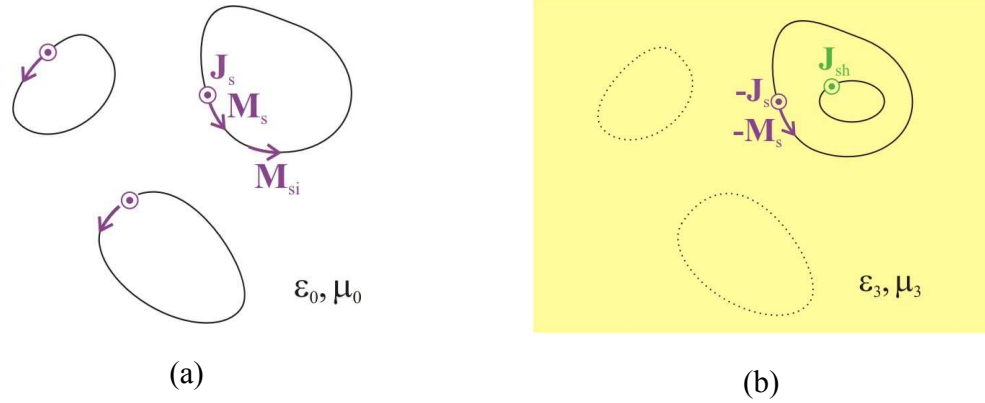


Fig. 2.2: Application of the equivalence theorem (a) exterior problem and (b) interior problem.

In the second problem, we consider only one body of Fig. 2.1 at a time. On the surface of that body, there is a layer of electric and magnetic currents with the same magnitude as in the exterior problem, but opposite in direction ( $-\mathbf{J}_s, -\mathbf{M}_s$ ) [95]. Those currents, along with all other field sources which are within this body, produce the exact field in the interior region of that body, but zero field outside the body. Hence, we substitute the zero-field region with the same medium as of that body. Assuming that the hidden objects inside that body are perfectly conducting, we replace these objects with their surface electric currents ( $\mathbf{J}_{sh}$ ). Hence, the sources of the electromagnetic field in the interior problem are the equivalent electric and magnetic currents on the surface of the body ( $-\mathbf{J}_s, -\mathbf{M}_s$ ) and the electric currents on the surfaces of the hidden objects ( $\mathbf{J}_{sh}$ ). All these currents are placed in a homogeneous medium, as shown in Fig. 2.2b.

## 2.3 Electric Field Integral Equation

We compute the unknown equivalent surface currents by applying the method of moments [30] on an electric-field integral equation (EFIE) [31]. To formulate the EFIE, we express the electric field in terms of the potentials as

$$\mathbf{E} = -\text{grad}V - j\omega\mathbf{A} - \frac{1}{\varepsilon}\text{rot}\mathbf{F} + \mathbf{E}_i, \quad (2.3)$$

where  $V$  is the electric scalar-potential,  $\mathbf{A}$  is the magnetic vector-potential,  $\mathbf{F}$  is the electric vector-potential,  $\omega$  is the angular frequency, and  $\varepsilon$  is the permittivity of the medium. The electric currents are  $z$ -directed, with no  $z$ -variation. Because of the continuity equation [95], there are no electric charges associated with such currents. Consequently, the  $\text{grad}V$  term is zero. The vector potentials are given by

$$\mathbf{A}(\mathbf{r}) = \mu \int_s \mathbf{J}_s(\mathbf{r}') g(r) ds, \quad (2.4)$$

$$\mathbf{F}(\mathbf{r}) = \varepsilon \int_s \mathbf{M}_s(\mathbf{r}') g(r) ds, \quad (2.5)$$

where  $g$  is Green's function,  $\mathbf{r}$  is the position vector of the point in which we compute the potentials (field point),  $\mathbf{r}'$  is the position vector of the current element (source point),  $r$  is the distance between the field point and the source point, and  $s$  is the circumference of the boundary surfaces where the currents are located. In the exterior problem, the medium is a vacuum. so that Green's function is

$$\mathbf{g}(r) = -\frac{j}{4} H_0^{(2)}(\beta_0 r), \quad \beta_0 = \omega \sqrt{\varepsilon_0 \mu_0}, \quad (2.6)$$

where  $H_0^{(2)}$  is the Hankel function of the second kind and order zero,  $\varepsilon_0$  is permittivity of a vacuum,  $\mu_0$  is the permeability of a vacuum, and  $\beta_0$  is the phase coefficient in a vacuum. In the interior problems, Green's functions are

$$\mathbf{g}_i(r) = -\frac{j}{4} H_0^{(2)}(-j\gamma_i r), \quad (2.7)$$

$$\gamma_i = j\omega \sqrt{\varepsilon_i \mu_i}, \quad i = 1, \dots, N, \quad (2.8)$$

where  $\varepsilon_i$ ,  $\mu_i$ , and  $\gamma_i$  are the respective permittivity, permeability, and propagation coefficient of the  $i$ th body.

## 2.4 Numerical Solution

We use pulse expansion (basis) functions to approximate the unknown current distribution [30], [31]. To that purpose, we divide all interfaces into a number of straight-line segments and assume that the surface currents are uniformly distributed along each segment:

$$J_s(x, y) \approx \sum_{k=1}^K J_{s,k} f_k(x, y), \quad (2.9)$$



$$M_s(x, y) \approx \sum_{k=1}^K M_{s,k} f_k(x, y), \quad (2.10)$$

$$f_k(x, y) = \begin{cases} 1 & \text{on the } k\text{th segment,} \\ 0 & \text{otherwise.} \end{cases} \quad (2.11)$$

In (2.11),  $J_{s,k}$  is the electric-current density on the  $k$ th segment,  $M_{s,k}$  is the magnetic-current density on the  $k$ th segment, and  $K$  is the total number of the segments on all interfaces. Similarly, we denote by  $J_{sh,l}$ ,  $l = 1, \dots, L$ , the electric-current densities on the segments belonging to the hidden objects. The total number of the unknown current coefficients is  $2K + L$ .

The electric field due to the unit electric-current source (surface electric currents) and unit magnetic-current source is (surface magnetic currents) is, respectively,

$$\mathbf{E}(\mathbf{r}) = -j\omega\mu \mathbf{i}_z \int_{s_k} g(r) ds, \quad (2.12)$$

$$\mathbf{E}(\mathbf{r}) = \int_{s_k} \frac{dg}{dr} (\mathbf{u}_k \times \mathbf{u}_r) ds, \quad (2.13)$$

where  $s_k$  denotes the  $k$ th segment where the currents are located,  $\mathbf{u}_r$  is the unit vector in the direction of the distance  $r$  (pointing from the source point towards the field point), and  $\mathbf{u}_k$  is the unit vector in the direction of the segment  $s_k$ . The cross-product  $\mathbf{u}_k \times \mathbf{u}_r$  is parallel to the  $z$ -axis. Hence, the electric field has only the  $z$ -component, which is in accordance with the assumed TM polarization.

We use the point-matching technique [30], [31] to compute the unknown current coefficients. For the exterior region, we impose the condition that the electric field is zero on the inner faces of the surfaces of all bodies (EFIE constraint). The overall number of matching points is  $K$ . After substituting the current approximations (2.9) and (2.10) into (2.3), we obtain the first set of linear equations,

$$-\sum_{k=1}^K J_{s,k} \left( j\omega\mu_0 \int_{s_k} g(r) ds \right) + \sum_{k=1}^K M_{s,k} \left( \int_{s_k} \frac{dg}{dr} (\mathbf{u}_k \times \mathbf{u}_r) \cdot \mathbf{i}_z ds \right) = -E_i(\mathbf{r}_k), \quad (2.14)$$

where  $\mathbf{r}_k$  is the  $k$ th matching point,  $k = 1, \dots, K$ , and  $E_i(\mathbf{r}_k)$  is the impressed electric field at the  $k$ th matching point. The matching points are located at the midpoints of the segments.

The remaining set of  $K + L$  linear equations is obtained from the interior problems. In this case, we derive equations separately for each body. We impose the condition that the electric field is zero on the outer face of the surface of the considered body and on the surfaces of the objects hidden in that body. The EFIE constraint applied on the  $i$ th body yields

$$\begin{aligned} & -\sum_{k=1}^{K_i} J_{s,k} \left( j\omega\mu_i \int_{s_k} g(r) ds \right) + \sum_{k=1}^{K_i} M_{s,k} \left( \int_{s_k} \frac{dg}{dr} (\mathbf{u}_k \times \mathbf{u}_r) \cdot \mathbf{i}_z ds \right) + \\ & + \sum_{l=1}^{L_i} J_{sh,l} \left( \int_{s_l} j\omega\mu_i g(r) ds \right) = 0, \end{aligned} \quad (2.15)$$

$$\sum_{i=1}^N K_i = K, \quad \sum_{i=1}^N L_i = L, \quad (2.16)$$

where  $K_i$  is the number of the segments on the surface of the  $i$ th body,  $L_i$  is the number of the segments on the surfaces of the hidden objects in the  $i$ th body, and  $\mathbf{r}_k$  is the  $k$ th matching point,  $k = 1, \dots, K_i + L_i$ . (The impressed electric field is zero at the considered matching points, because the sources of the impressed field remained in the exterior region.)

The integrals in (2.14) and (2.15) are computed numerically. Equations (2.14) and (2.15) constitute a complete system of the linear equations for the unknown densities of the electric and magnetic currents. This system is solved using LU decomposition.

## 2.5 Matrix Parameters

The response of an electromagnetic system is typically represented using matrix parameters, such as the impedance ( $\mathbf{Z}$ ), admittance ( $\mathbf{Y}$ ), or scattering parameters ( $\mathbf{S}$ ) [96]. In the 2D systems under consideration, the admittance parameters relate the induced currents in the bodies to the excitation modeled by the impressed electric fields,

$$\mathbf{i} = \mathbf{Y}\mathbf{e}, \quad (2.17)$$

$$\mathbf{i} = [I_1 \quad \dots \quad I_N]^T, \quad (2.18)$$

$$\mathbf{e} = [E_1 \quad \cdots \quad E_N]^T, \quad (2.19)$$

where  $\mathbf{i}$  is the vector of the net electrical currents in the bodies,  $\mathbf{e}$  is the vector of the impressed electric fields in the bodies, and  $\mathbf{Y}$  is the admittance-parameter matrix. The element  $[\mathbf{Y}]_{(m,n)}$  is the net current induced in the  $n$ th body when the  $m$ th body is excited by a unit impressed electric field. The net current in the  $n$ th body is computed as

$$I_n = \sum_k J_{s,k} l_k, \quad (2.20)$$

where  $l_k$  is the length of the  $k$ th segment, and the summation is performed over all segments that belong to that body. The impedance matrix is obtained from the admittance matrix as  $\mathbf{Z} = \mathbf{Y}^{-1}$ .

# **Chapter 3**

## **Estimating Building Layouts Using Jump-Diffusion Algorithm**

### **3.1 Introduction**

The ultimate goal in through-the-wall imaging is to find the objects of interest (i.e., targets) hidden inside buildings. However, the performance of the estimation, detection and classification algorithms depends greatly on the knowledge of building layouts. The simplified models that comprise only outer walls neglect the electromagnetic interaction between the target and inner walls. If this interaction is not properly modeled, the important piece of information about the target is lost.

Reconstruction of the dielectric profile of electrically large objects such as buildings is a severely ill-posed problem. Instead of looking for a general solution, we take advantage of the prior knowledge on typical building layouts [1], [2]. We assume that the unknown domain may be suitably represented by rectangular walls. We use the jump-diffusion algorithm [10]-[13] to estimate the number, position and the length of the unknown inner walls.

The forward modeling has an important role in the estimation. It influences the accuracy and computational efficiency of the solution. To compute the electromagnetic response of the considered system, we use the numerical procedure based on the method of moments described in Chapter 2.

We investigate the application of the jump-diffusion algorithm with wideband data. We obtain the rough estimates at the low-frequency part of the bandwidth that are later used to initiate more accurate estimation at higher frequencies.

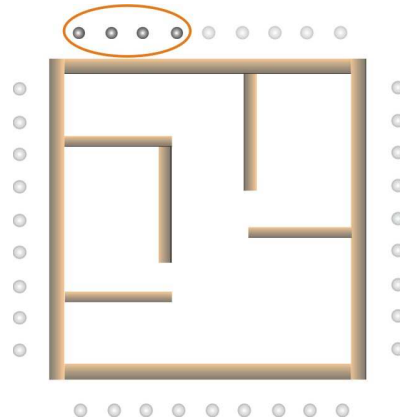


Fig. 3.1: Building layout and the four-sensor array.

## 3.2 Electromagnetic Modeling

We show an example of a building layout and a moving sensor array in Fig. 3.1. The array consists of  $M$  sensors taking measurements at  $N$  known positions and at  $L$  frequencies. In Fig. 3.1, the discrete measurement locations of the supposed four-sensor array are represented by dots.

### 3.3 Jump-Diffusion Algorithm

The building layout estimation belongs to the group of problems with unknown dimensionality, since besides position and characteristics of the walls, their number is also unknown. The application of the jump-diffusion algorithm in the cases where the dimensionality of the parameter space is not fixed was studied in e.g., [11], [12]. The jump-diffusion allows traversing through parameter space by two types of transformations: jumps between subspaces of different dimensionality and stochastic diffusions within continuous subspaces.

In the problem we consider, the dimensionality of the subspace is equal to the number of walls. Within each subspace, the unknown parameters for each wall are: center coordinates  $(x, y)$ , length  $(l)$ , and orientation  $(\alpha)$ . We assume that the thickness and the dielectric permittivity of the walls are known. However, we also consider cases in which these parameters are not exactly known. In the subspace with  $k$  walls, the vector of the unknown parameters is  $\theta^{(k)} \in \mathfrak{R}^{4k}$ . We represent the pair  $(k, \theta^{(k)})$  as  $X$ . Generally,  $X$  varies within parameter space  $\mathfrak{S} = \bigcup_{k \in k_{\max}} \mathfrak{S}_k$ , where  $\mathfrak{S}_k = \{k\} \times \mathfrak{R}^{4k}$  and  $k_{\max}$  is the maximum number of walls.

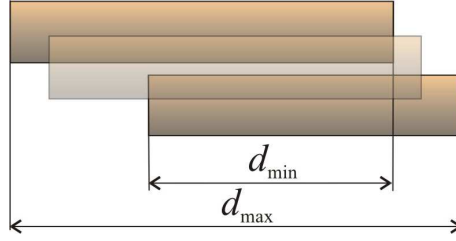


Fig. 3.2: Merge transformation.

We seek for the solution  $\hat{X}$  that maximizes the likelihood function. To explore the parameter space  $\mathfrak{S}$ , we use two types of transformations: transformations that change the number of walls (jumps), and transformations that only perturb the parameters of the existing walls (diffusion). Some of the transformations are inspired by [12], where the segmentation of radar images of urban areas is considered. In the first group of transformations, we have:

- Birth: A new wall is added to the current configuration. The parameters of the new wall are  $(x', y', l', \alpha')$ . We assume walls with the orientation:  $\alpha \in \{0, \pm 45^\circ, 90^\circ\}$ .
- Death: A randomly selected inner wall is removed from the current configuration.
- Merge: A randomly selected inner wall is merged with a nearby wall (Fig. 3.2). The number of the walls is decreased, and the parameters of the merged wall are  $(x', y', l', \alpha')$ .

In the second group are the transformations that change one or more parameters of a randomly selected wall from the current layout:



- Translation: The position of the wall is perturbed  $(x', y')$ .
- Elongation: The length of the wall is perturbed  $(l')$ .
- Rotation: The orientation of the wall is perturbed  $(\alpha')$ .
- Regeneration: All parameters of the wall are perturbed  $(x', y', l', \alpha')$ .
- Optimization: The parameters of the wall  $(x', y', l')$  are optimized using simplex algorithm [97].

In each iteration, one of the transformations is selected according to the adopted probability distribution. The probabilities for transformations are chosen empirically and depend on the current scene estimate,  $X$ . The details for the above transformations and their probabilities are given in Appendix. The selected transformation is applied on a randomly chosen wall (unless birth is selected), where the probability of the drawing is the same for all walls. The result of the transformation is a proposed layout  $X'$ . This layout may be accepted or rejected, depending on the definition of transition kernel. The popular solution is the Metropolis-Hastings algorithm [98], [99] that enables escaping from local minima. However, we decided for the greedy algorithm since it is faster, and the speed of the algorithm is critical for practical applications of building layout estimation. Nevertheless, the probability for falling into local minima is reduced by proper frequency selection and wide exploration of the parameter space. The proposed layout will be accepted depending on the likelihood function only: if the likelihood for the proposed layout  $X'$  is larger than the likelihood for the current layout  $X$ , the proposed

layout will be accepted. Otherwise the current layout  $X$  remains.

### 3.4 Measurement Model

Sensor arrays can be considered as multiport networks. Therefore, measurements may be represented by impedance, admittance or scattering parameters [96]. Here, we use the impedance parameters. Hence, in the sensors, the known excitations are the currents and the observed variables are the induced electric fields. The measured signal at the  $i$ th sensor, when the  $j$ th sensor is transmitting reads,

$$E(i, j, n, f_l) = z_{ij}(i, j, n, f_l)I_j + w, \\ i, j = 1, \dots, M, \quad n = 1, \dots, N, \quad l = 1, \dots, L, \quad (3.1)$$

where  $f_l$  is the operating frequency,  $n$  is the index of the measurement position,  $z_{ij}$  is the mutual impedance parameter between the  $i$ th and  $j$ th sensor,  $I_j$  is the feeding current of the  $j$ th sensor and is  $w$  additive noise.

We assume that the noise is a complex zero-mean Gaussian random variable with variance  $\sigma^2$ . In this case, the likelihood function is given by

$$p(\mathbf{e} | X) \sim \exp\left(-\sum_{l=1}^L \sum_{i=1}^M \sum_{j=1}^M \sum_{n=1}^N |E(i, j, n, f_l) - z_{ij}(n, f_l | X)I_j|^2 / \sigma^2\right), \quad (3.2)$$

where  $\mathbf{e}$  is the  $LM^2N$  dimensioned vector in which we stack all the measurements

$E(i, j, n, f_i)$ . We seek for the solution  $\hat{X}$  that maximizes the likelihood (3.2).

For a given current estimate  $X$ , the summary of the algorithm is given below.

#### Summary of the Single-Frequency Algorithm

- Draw a transformation according to the probability distribution  $p_T(X)$ .
- Draw a wall from  $X$ , where the probability is the same for all walls (unless the birth is selected).
- Calculate the proposed layout,  $X'$ .
- Compare the likelihood functions for both layouts. If  $p(e | X') > p(e | X)$ , accept the proposition. Reject it otherwise. (The algorithm also rejects absurd layouts such as building with two crossing walls.)
- Repeat the procedure, unless the maximal number of the iterations is reached or the improvement becomes negligible.

### **3.5 Multiple-Frequency Approach**

For sensing through the walls, a wideband approach is necessary to achieve the desired feature resolution. The positive influence of the multiple frequencies on the inverse scattering algorithms has been widely studied [8], [100]-[106]. The inverse problems are ill-posed due to the finite dimensionality of the scattered field [7]. Consequently, the number of parameters that can be estimated from the scattered field is limited. If the

number of sought parameters exceeds the dimensionality of the scattered field, the solution is not unique and the procedure diverges. The dimensionality increases with frequency; nevertheless the inverse scattering at high frequencies is easily trapped at a false solution. The multifrequency data processing mitigates the ill-posedness and improves the robustness against false solutions. A common multi-frequency approach is frequency hopping where the low-frequency solution is used to initialize the high-frequency solution (e.g., [100]). However, the frequency hopping technique is suitable to the problems where the low-frequency spectrum of the unknown profile has significant contribution to the overall spectrum content [7]. Otherwise the procedure may yield erroneous results. The alternative is to perform simultaneous analyses of multi-frequency data [8], [106]. Finally, a hybridization of above methods is possible.

Previous results were derived using deterministic analysis. However, similar conclusions hold when the unknown profile is reconstructed using the jump-diffusion algorithm. The low-frequency measurements are not very sensitive to small perturbations of the building layout. Consequently, the probability of acceptance of the proposed transformation is high. The jump-diffusion algorithm applied at low frequencies traverses quickly through different building layouts, converging to the solutions that are close to the exact layout. The method of moments models are also very efficient at low frequencies. However, the low-frequency estimation with jump-diffusion lacks desired resolution, and might detect false walls, etc. At high frequencies, the probability of acceptance of the proposed layout is small unless it is very close to the exact solution (probability of adding a new wall is particularly low). Therefore, the proposed algorithm remains in one state too long unless

the proposed state is very close to the exact solution. Consequently the convergence at high frequencies is very slow. In addition, the forward calculations are exceptionally time-consuming. Hence, we use low frequencies for the initial estimation.

We investigated the application of frequency hopping, joint processing, and hybrid approach for the building layout estimation. The best results were achieved using the hybrid approach. The estimation was performed in steps, where we use the estimates obtained at lower frequencies to feed the estimation at higher frequencies. We start at the lowest frequency in the available frequency band, initially assuming there are no inner walls. The algorithm converges to the first-step estimate  $\hat{X}_1$ . We use this estimate to initiate the second-step jump-diffusion, which is performed simultaneously at frequencies  $(f_1, f_2)$ , where  $f_2 > f_1$ . The selection of the next frequency has important role in the estimation process. If the next frequency is too close to the previous frequency, the estimate improvement is negligible. On the other hand, if it is much higher, the analysis diverges. In the latter case, the algorithm removes walls from the scene unless they are almost identical to true walls. At the same time, the acceptance rate for transformations other than death is very low. Therefore, the next frequency should be chosen adaptively based on the transformation acceptance rate.

We repeat those steps, each time including a new higher frequency into the set of the operating frequencies. Keeping lower frequencies instead of just jumping to higher frequencies does not increase the calculation time significantly, but it is essential for the robustness of the algorithm. Similar behavior is recorded in [8] where deterministic

approach is applied.

As we increase the frequency, we accordingly reduce the space for the parameter search. The probabilities of the transformations are also frequency dependent, e.g., as the frequency increases, the probability of fine transformations, such as optimization, becomes higher. We give the practical details of the algorithm in the Appendix.

The summary of the multiple-frequency version of the algorithm is given below.

#### Summary of the multiple-frequency algorithm

- Given the estimate from the step  $i-1$  ( $\hat{X}_{i-1}$ ), in the step  $i$ :
- Select the frequency  $f_i$ , where  $f_i > f_{i-1} > \dots > f_1$ .
- Update the transformations and their probabilities.
- Apply the jump-diffusion algorithm at frequencies  $(f_1, f_2, \dots, f_i)$  where the initial estimate is  $\hat{X}_{i-1}$ .
- Repeat the procedure, unless the maximal frequency is reached or the improvement becomes negligible.

## **3.6 Numerical Results**

We examined the performance of the proposed method through many numerical experiments. We estimated the number, positions, orientations, and lengths of the inner

walls in a  $4\text{ m} \times 4\text{ m}$  building. For simplicity, we assumed that the thickness and the relative permittivity of the walls were known. However, we addressed the cases in which those parameters were not exactly known. Besides walls, there were unknown clutter objects in the building simulating furniture. The adopted thicknesses of the exterior and interior walls were 20 cm and 15 cm, respectively. The clutter objects had square cross section (side 20-30 cm) and circular cross sections (diameter 20-30 cm). We tested the algorithm in a wide range of wall permittivities. We considered both simplified and realistic models for wall permittivity. The permittivity of the clutter objects was the same as the permittivity of the walls. In our simulations, the measurements were taken by a 4-sensor array ( $M=4$ ). There were 25 measurement locations at each side of the building. The separation between the adjacent sensor was 15 cm. We define the signal-to-noise ratio ( $SNR$ ) as

$$SNR = |\mathbf{e} - \mathbf{e}_s|^2 / \sigma^2. \quad (3.3)$$

where  $\mathbf{e}_s$  is the vector of the induced electrical fields in the sensors located in a free space.

As the first example, we considered the layout with five unknown walls and three square clutter objects (Fig. 3.3). The assumed wall permittivity was  $\epsilon_r = 3 - j0.45$ . The first-step estimate was computed at  $f_1 = 10\text{MHz}$ , the second-step estimate at  $f_1 = 10\text{MHz}$  and  $f_2 = 100\text{MHz}$ , and the third-step estimate at  $f_1 = 10\text{MHz}$ ,  $f_2 = 100\text{MHz}$ , and  $f_3 = 200\text{MHz}$ . The number of iterations for each step was,

respectively, 400, 200, and 100. We performed 10 independent estimations. We overlapped the results obtained in different simulations and showed them jointly in Fig. 3.3. The estimated walls are represented as the gray rectangles, while the black lines denote the true layout. We did not estimate the clutter objects. Dark areas correspond to more probable layouts. The parameters of the estimated walls fluctuate around their true values. As the frequency increases, the variances of the estimated parameters decrease. The third-step layout is very close to the exact solution, and it suffices to perform deterministic optimization at higher frequencies if more accurate estimate is needed.

In the second example, we considered the layout with oblique walls. Since the layout is more complex, there are more unknown parameters. We initiated the estimation at  $f_1 = 10\text{MHz}$ , but the algorithm converged slowly. We added a higher frequency  $f_2 = 50\text{MHz}$ , which is sufficiently separated from  $f_1$ . Therefore, we computed the first-step estimate at  $f_1 = 10\text{MHz}$  and  $f_2 = 50\text{MHz}$ , the second-step estimate at  $f_1 = 10\text{MHz}$ ,  $f_2 = 50\text{MHz}$ , and  $f_3 = 100\text{MHz}$ , and the third-step estimate at  $f_1 = 10\text{MHz}$ ,  $f_2 = 50\text{MHz}$ ,  $f_3 = 100\text{MHz}$ , and  $f_4 = 150\text{MHz}$ . The number of iterations for each step was 400, 200, and 100. The results are presented in Fig. 3.4. The parameters of the walls oscillate around their true values, due to the presence of clutter.



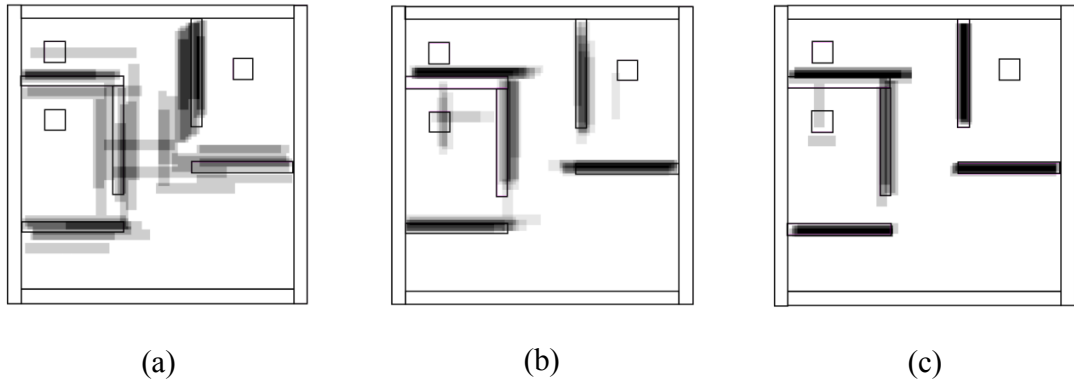


Fig. 3.3: (a) First step:  $f_1 = 10\text{MHz}$ , 400 iterations, (b) second step:  $f_1 = 10\text{MHz}$ ,  $f_2 = 100\text{MHz}$ , 200 iterations, (c) third step:  $f_1 = 10\text{MHz}$ ,  $f_2 = 100\text{MHz}$ ,  $f_3 = 200\text{MHz}$ , 100 iterations. The results are shown jointly for 10 independent simulations. The wall permittivity is  $3-j0.45$ .

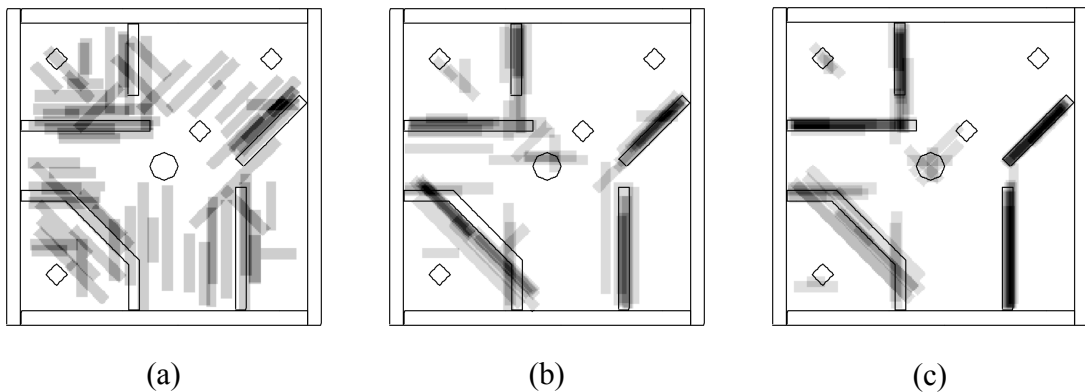


Fig. 3.4: (a) First step:  $f_1 = 10\text{MHz}$ ,  $f_2 = 50\text{MHz}$ , 400 iterations, (b) second step:  $f_1 = 10\text{MHz}$ ,  $f_2 = 50\text{MHz}$ ,  $f_3 = 100\text{MHz}$ , 200 iterations, (c) third step:  $f_1 = 10\text{MHz}$ ,  $f_2 = 50\text{MHz}$ ,  $f_3 = 100\text{MHz}$ ,  $f_4 = 150\text{MHz}$ , 100 iterations. The results are shown jointly for 10 independent simulations. The wall permittivity is  $3-j0.45$ .

We also considered concrete walls with realistic models for permittivity. The permittivity of concrete changes significantly at low frequencies [107], [108]. We used the Cole-Cole model [108]

$$\varepsilon_r = \varepsilon_\infty + (\varepsilon_s - \varepsilon_\infty) / (1 + j(f / f_0)^{1-\alpha}), \quad (3.4)$$

to fit the experimental data for concrete provided in [107]. We obtained values:  $\varepsilon_\infty = 7$ ,  $\varepsilon_s = 22$ ,  $\alpha = 0.3$ , and  $f_0 = 20$  MHz. The algorithm performed similarly as in the case with the constant permittivity. The algorithm also detected clutter objects, as illustrated in Fig. 3.5. The first step estimate was computed at  $f_1 = 50$  MHz, the second-step estimate at  $f_1 = 50$  MHz, and  $f_2 = 100$  MHz, and the third-step estimate at  $f_1 = 50$  MHz,  $f_2 = 100$  MHz, and  $f_3 = 150$  MHz. The number of iterations for each step was 400, 300, and 200.

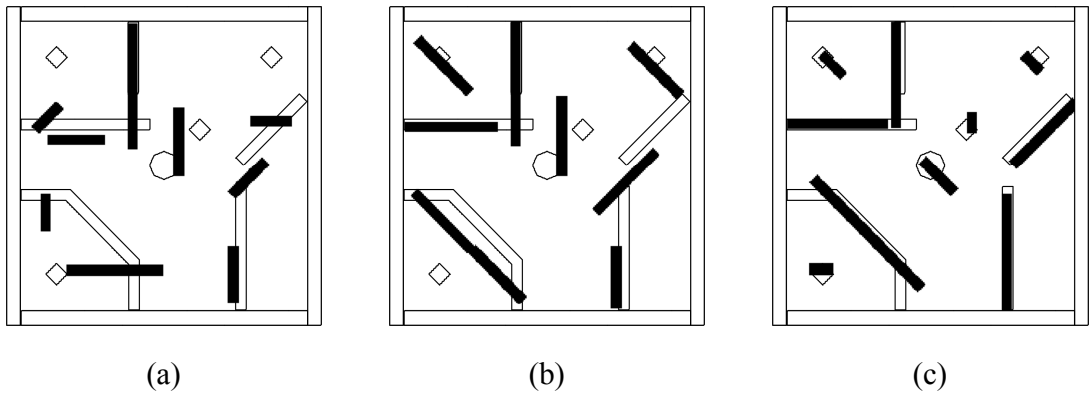


Fig. 3.5: (a) First step:  $f_1 = 50$  MHz, 400 iterations, (b) second step:  $f_1 = 50$  MHz,  $f_2 = 100$  MHz, 300 iterations, (c) third step:  $f_1 = 50$  MHz,  $f_2 = 100$  MHz,  $f_3 = 150$  MHz, 200 iterations. The wall permittivity is  $\varepsilon_r = 7 + 15 / (1 + j(f[\text{MHz}] / 20)^{0.7})$ .

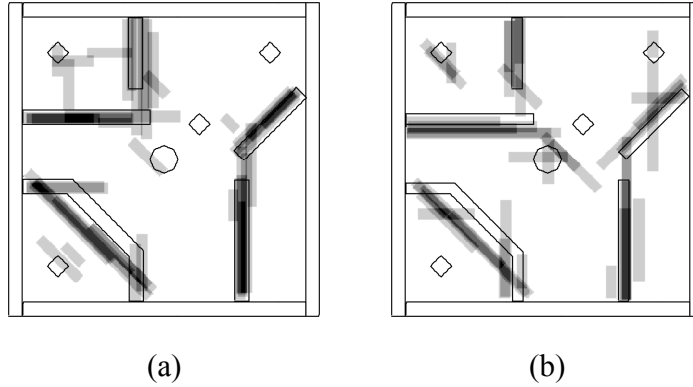


Fig. 3.6: (a) Estimation with erroneous wall thickness: true and assumed values are 0.2 m and 0.15 m, respectively. The third-step estimate,  $f_1 = 10\text{MHz}$ ,  $f_2 = 50\text{MHz}$ ,  $f_3 = 100\text{ MHz}$ , and  $f_4 = 150\text{ MHz}$ . (b) Estimation with erroneous wall permittivity: true and assumed values are  $3-j0.45$  and  $3.45-j0.55$ , respectively. The second-step estimate,  $f_1 = 10\text{MHz}$ ,  $f_2 = 50\text{MHz}$ , and  $f_3 = 75\text{ MHz}$ .

We also examined the robustness of the algorithm to the errors in the wall thickness. Various experiments showed that the algorithm is capable to estimate properly the layout in the case where the wall thickness was known only approximately. We considered the case in which the true thickness of the walls was 20 cm, whereas in simulations we assumed that it was 15 cm. We used the same frequencies and the same number of iterations as in the case of exact wall parameters. The results for the third-step estimate, obtained by 5 independent simulations, are shown in Fig. 3.6a. The estimated layouts provided a good initial representation of the exact solution. Due to the thickness error, the variance of estimated parameters was larger. However, the algorithm was able to provide useful insight into the building layout.

Finally, we investigated the case when the dielectric permittivity was known only approximately. In the considered example, the exact permittivity was  $\epsilon_r = 3 - j 0.45$  and

the assumed permittivity was  $\epsilon_r = 3.45 - j0.55$ . (The relative error was 15 %.) In the first step, computed at  $f_1 = 10\text{MHz}$  and  $f_2 = 50\text{MHz}$ , the algorithm performed similarly to the case without the error. However, in the second step, calculated at  $f_1 = 10\text{MHz}$ ,  $f_2 = 50\text{MHz}$ , and  $f_3 = 100\text{ MHz}$ , the number of accepted moves was extremely low. Therefore we decreased the third frequency to  $f_3 = 75\text{ MHz}$ . In the third step we choose new frequency to be  $f_4 = 100\text{ MHz}$ . However, the improvement in the third step was insignificant. In Fig. 3.6b we show results for the second-step estimate, obtained by 5 independent simulations. Compared to the case with the exact wall parameters, lower frequencies were used and less accuracy was achieved.

### 3.7 Summary

We have developed a scheme for estimating unknown building layouts. The proposed approach uses the jump-diffusion algorithm with a moving sensor system to determine the number and parameters of the unknown inner walls (position, length, orientation). We demonstrated that the jump-diffusion algorithm is an efficient tool for solving inverse electromagnetic scattering problems for which we have some prior knowledge.

We designed an adaptive procedure that uses low-frequency (low-resolution) estimates to initiate high-frequency (high-resolution) estimation. The choice of the operating frequency has significant influence on the convergence of the jump-diffusion algorithm. Accurate estimates may be obtained using only a few frequencies, thus making possible

the use of jump-diffusion in real scenarios. We examined the robustness of our approach in the presence of unknown clutter objects. The algorithm proved capable of discriminating between walls and smaller-size clutter objects. We also showed that the algorithm was not sensitive to small errors in the wall thickness or material relative permittivity.

# **Chapter 4**

## **Estimating Targets behind Reinforced Concrete Walls**

### **4.1 Introduction**

In Chapter 3, we estimated building layouts using stochastic geometry and electromagnetic sensing. Once we have determined the displacement of the inner walls, we may be able to find the targets more easily. Nevertheless, the interaction between electromagnetic waves and walls can be far more complex than that predicted by simple wall models such as homogeneous dielectric slabs [16], [17]. The difficulties in target imaging are particularly pronounced in the case of walls reinforced by parallel steel bars or cinder-block walls. Typically, target spreads are large and false targets appear. The localization of the targets behind cinder blocks is tackled in [21]. Here, we investigate the case of reinforced concrete walls [26].

Rigorous analyses of the transmission and reflection properties of reinforced walls for far-field incidence have been carried out in [27]-[29]. In contrast, we assume an arbitrary distance of the sensors and targets from the wall. Moreover, our focus is on estimating

the targets hidden behind reinforced walls rather than computing the electromagnetic response of such walls.

We compare the cases of known and unknown wall parameters. We compute the near-field transmission and reflection characteristics of the wall using the forward electromagnetic model of Chapter 2, then incorporate these parameters in a beamforming imaging method for improved results.

## 4.2 Electromagnetic Model

Wall reinforcements are either bars or mesh. When the incident electromagnetic field is parallel to vertical bars, the horizontal bars (cross bars) have only a small influence on the wall response [27]. The same reasoning applies when the incident electric field is parallel to the horizontal bars. Therefore, without loss of generality, we will consider a wall reinforced with vertical bars.

Fig. 4.1 depicts the cross section of a system comprising the sensor array and the target hidden behind the wall. The distance between adjacent bars (bar period) is  $d_{\text{bar}}$ , the bar diameter is  $D_{\text{bar}}$ , and the wall thickness is  $w$ . The bars are perfectly conducting and immersed in a homogeneous material of relative dielectric permittivity  $\epsilon_r$ . We model the sensors as thin, perfect conductors, excited one at a time by known currents. We compute the array response using the forward model described in Chapter 2.

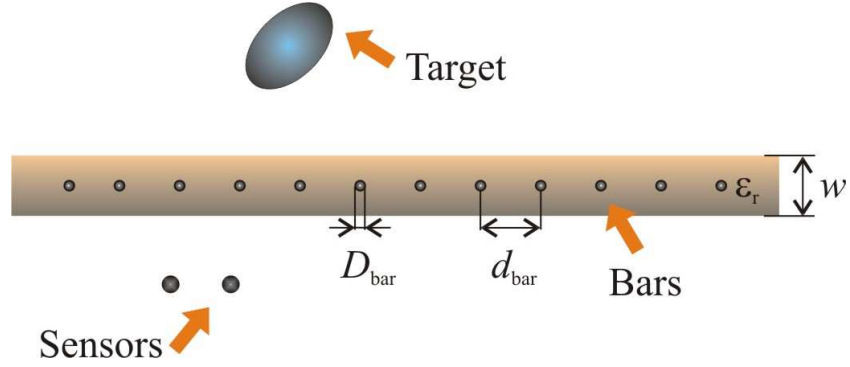


Fig. 4.1: Cross section of the reinforced concrete wall.

### 4.3 Measurement Model

We suppose that a uniform linear array of  $M$  sensors is positioned in front of the reinforced wall. The array moves along the wall and takes measurements at  $N$  known positions. The measurements are performed in a wide frequency range at  $L$  frequencies. In the considered scenario, one sensor transmits at a time and all sensors receive the reflected signals. The observed variables are the electric fields induced in the sensors. The measured signal in the  $i$ th sensor when the  $j$ th sensor is excited reads

$$E_{ij}(n, f_l) = z_{ij}(n, f_l)I_j(f_l) + u, \quad (4.1)$$

$$i, j = 1, \dots, M, \quad n = 1, \dots, N, \quad l = 1, \dots, L,$$

where  $f_l$  is the operating frequency,  $n$  is the index of the measurement position,  $z_{ij}(n, f_l)$  is the mutual impedance parameter between the  $i$ th sensor and the  $j$ th sensor,  $I_j(f_l)$  is the feeding current of the  $j$ th sensor, and  $u$  is the additive noise. The feeding current is the



same for all sensors. We assume  $I_j(f_i)$  is the Fourier transform of a Gaussian pulse,  $G(f_i)$ .

## 4.4 Estimating Wall Parameters

Electromagnetic waves are reflected from interfaces of media with different electromagnetic properties. We can separate these reflections in the time domain if the measurements have sufficiently wide bandwidth. Hence, we perform a Fourier transform on (4.1) to obtain the time-domain waveforms of the received signals.

We compute the dielectric permittivity of reinforced walls in the same manner as the permittivity of homogeneous walls (see, e.g., [109]-[112]). The responses of both walls in the time domain are identical until the moment when the reflections from the bars reach the sensors [113]. In order to extract the reflection from the front side of the wall, the transmitted waveform should satisfy  $T \leq T_{\max} = 2d\sqrt{\epsilon_r}/c$ , where  $T$  is the waveform duration,  $d$  is the distance of the rebar from the front side of the wall, and  $c$  is the propagation speed of electromagnetic waves in a vacuum.

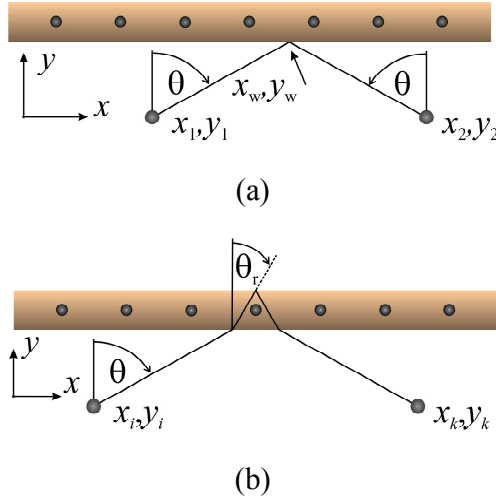


Fig. 4.2: Scheme used for (a) wall-permittivity estimation and (b) wall-thickness permittivity estimation.

In the case of small losses, the reflection coefficient of the TM wave at the air-dielectric interface is

$$R(\theta) = \frac{\cos\theta - \sqrt{\epsilon_r - \sin^2\theta}}{\cos\theta + \sqrt{\epsilon_r - \sin^2\theta}}, \quad (4.2)$$

where  $\theta$  is the incident angle, computed with respect to the wall normal. We assume that angle  $\theta$  is small; hence  $R(\theta) \approx R(0)$ . To estimate the permittivity, we coherently add the received signals. The time delay ( $\tau_{ik}$ ) between the  $i$ th and  $k$ th sensors, according to Fig. 4.2a, is given by:

$$s_{ik} = \sqrt{(x_i - x_w)^2 + (y_w - y_i)^2} + \sqrt{(x_k - x_w)^2 + (y_w - y_k)^2}, \quad \tau_{ik} = s_{ik} / c_0, \quad (4.3)$$

where  $(x_w, y_w)$  are the Cartesian coordinates of the reflection point on the wall. The focused signal reads

$$E_0(t) = \frac{1}{NM^2} \sum_{n=1}^N \sum_{i=1}^M \sum_{k=1}^M E_{ik}(n, t + \tau_{ik}) \sqrt{s_{ik}(n)}, \quad (4.4)$$

where  $E_{ik}(n, t)$  is the time-domain waveform of the electric field induced in the  $k$ th sensor when the  $i$ th sensor is excited, and  $n$  is the index of the measurement position. Multiplication by the factor  $\sqrt{s_{ik}(n)}$  ensures that all received signals have the same attenuation, corresponding to the attenuation at distance  $s = 1$  m. We calculate the reflection coefficient for small  $\theta$  as

$$\hat{R}(0) = \left( \int_0^T E_0(t) h(t) dt \right) / \left( \int_0^T h^2(t) dt \right), \quad (4.5)$$

where  $h(t)$  is the reference pulse. The delayed pulse,  $h(t - s/c_0)$ , is the induced electric field in the sensor that is separated by distance  $s = 1$  m from the transmitting sensor (sensors are in vacuum). We compute  $h(t)$  numerically, using the forward model of Chapter 2. The estimate of the wall permittivity from (4.2) is

$$\hat{\epsilon}_r = \left( \frac{1 - \hat{R}(0)}{1 + \hat{R}(0)} \right)^2. \quad (4.6)$$

In order to estimate the wall thickness, we focus the received signals in the time domain with respect to the delay of the reflection from the back side of the wall. If the wall is reinforced, this reflection is substantially concealed by the multiple reflections from the bars. We illustrate the signal path in this case in Fig. 4.2b. The signal transmitted by the  $i$ th sensor, reflected from the back side of the wall and received by the  $k$ th sensor, is

delayed for time

$$\tau_{ik}(w) = \left( (2y_w - y_i - y_k) / \cos \theta + 2w \varepsilon_r / \sqrt{\varepsilon_r - (\sin \theta)^2} \right) / c_0, \quad (4.7)$$

$$\theta = \arg \min_{\theta} \left\{ x_k - x_i - (2y_w - y_i - y_k) \tan \theta - 2w \sin \theta / \sqrt{\varepsilon_r - (\sin \theta)^2} \right\}. \quad (4.8)$$

The summation of the received signals, focused using delay  $\tau_{ik}(w)$ , is

$$E_0(t) = \frac{1}{NM^2} \sum_{n=1}^N \sum_{i=1}^M \sum_{k=1}^M E_{ik}(n, t + \tau_{ik}(w)). \quad (4.9)$$

We compute the correlation of the focused electric field and the reference pulse  $h(t)$  by

$$I(w) = \int_0^T E_0(t) h(t) dt \quad (4.10)$$

for different wall thicknesses,  $w$ . The estimate of the wall thickness is defined as the maximum of (4.10). Due to the periodicity of (4.9), the correlation does not yield a unique solution. Nonetheless, practical limits on the wall thickness reduce the number of estimates to only a few.

## 4.5 Estimating Target Positions

Assuming that measurements of the stationary scene (scene without moving targets) can be made, we obtain the signals reflected from the targets by subtracting the measurements of the stationary background from the measurements altered by the appearance of

the targets. The typical approach in localizing targets behind walls is to apply beamforming on the reflected signals [16]. Here, we adapt the beamforming to include the response of the reinforced wall. We compare the performances of the method when the wall parameters are known and when they are unknown.

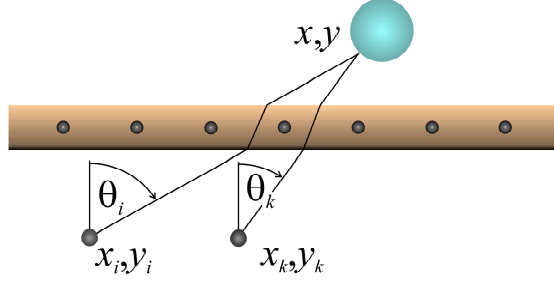


Fig. 4.3: Target position estimation.

#### 4.5.1 Unknown Bar Parameters

We first determine the target position without considering the influence of the reinforcement. Fig. 4.3 depicts the estimation setup. The delay of the signal reflected from the target when the  $i$ th sensor is transmitting and the  $k$ th sensor is receiving reads,

$$\tau_{ik}(x, y) = \tau_i(x, y) + \tau_k(x, y), \quad (4.11)$$

$$\tau_{i(k)}(x, y) = \left( (y - y_{i,k} - w) / \cos \theta_{i,k} + w \epsilon_r / \sqrt{\epsilon_r - (\sin \theta_{i,k})^2} \right) / c_0, \quad (4.12)$$

where  $\tau_i$  and  $\tau_k$  are the respective propagation times from the  $i$ th and the  $k$ th sensor to the target, and  $(x, y)$  are the Cartesian coordinates of the target. As illustrated in Fig. 4.3, the  $i$ th sensor launches the signal at angle  $\theta_i$  whereas the  $k$ th sensor receives the signal

from the target at angle  $\theta_k$ . We calculate those angles as

$$\theta_{i,k} = \arg \min_{\theta} \left\{ x - x_{i,k} - (y - y_{i,k} - w) \tan \theta - w \sin \theta / \sqrt{\epsilon_r - (\sin \theta)^2} \right\}. \quad (4.13)$$

The received signals are delayed for  $\tau_{ik}(x, y)$  and summed. The focused electric field is

$$\Delta E(t; x, y) = \sum_{n=1}^N \sum_{i=1}^M \sum_{k=1}^M \Delta E_{ik}(n, t + \tau_{ik}(x, y)), \quad \Delta E_{ik} = E_{ik} - E_{ik}^{\text{stat}}, \quad (4.14)$$

where  $E_{ik}^{\text{stat}}$  is the induced electric field in the stationary scene and  $E_{ik}$  is the induced electric field due to the appearance of the targets. We compute the target image as the correlation between the focused electric field and reference pulse  $h(t)$ :

$$I(x, y) = \int_0^T \Delta E(t; x, y) h(t) dt. \quad (4.15)$$

## 4.5.2 Known Bar Parameters

We now consider the computation of the reference pulse, which takes into account the waveform distortion due to the presence of the bars. We assume that the distance between the bars and the diameter of the bars are known. (The estimation of the unknown bar parameters is studied in [109] and [110].) The transmission coefficient of the reinforced wall for the plane wave incidence is given by

$$T(f, \theta) = E_t / E_i, \quad (4.16)$$

where  $\theta$  is the incident angle,  $E_i$  is the incident electric field at the front side of the wall, and  $E_t$  is the electric field transmitted through the wall. The computation of (4.16), which exploits the periodic structure of infinitely long reinforced walls, can be found in [27], [29].

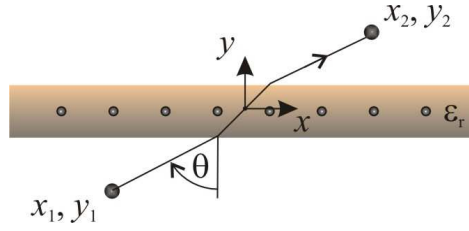


Fig. 4.4: Numerical calculation of the wall transmission coefficients.

In the considered problem, the reinforced wall is not necessarily in the far field of the sensors. Therefore, we compute the transmission coefficient exactly, using the forward procedure described in Chapter 2. We illustrate the corresponding model in Fig. 4.4. We assume that the sensor located at  $(x_1, y_1)$  is excited and compute the induced electric field in the sensor located at  $(x_2, y_2)$ . The near-field transmission coefficient is given by

$$T(f, \theta) = E_{12}(f, \theta) / E_{12}^0(f, \theta), \quad (4.17)$$

where  $E_{12}$  is the induced electric field with the wall present, and  $E_{12}^0$  is the induced electric field when the sensors are in a vacuum. The dependence of (4.17) on  $x_1$ ,  $x_2$ ,  $y_1$ , and  $y_2$  is assumed and suppressed.

The signal reflected from the target goes through the wall twice. For the target in Fig. 4.3, the signal transmitted at angle  $\theta_i$  passes through the wall, gets reflected from the target,

passes through the wall again, and reaches the sensor at angle  $\theta_k$ . In the receiving sensor, the induced electric field (neglecting the complex scaling constant) is approximately

$$E_{ik}(f) \sim H(f)T(f, \theta_i)T(f, \theta_k), \quad (4.18)$$

where  $H(f)$  is the Fourier transform of  $h(t)$ . Hence, we adopt a new reference pulse:

$$\tilde{h}(t) = \text{rect}\left(\frac{t}{T}\right) F^{-1}\{AH(f)T(f, \theta_i)T(f, \theta_k)\exp(j2\pi f\tau_0)\}, \quad (4.19)$$

where  $\tau_0$  is the time delay that assures that the reference pulse is centered at  $t = 0$ , and  $A$  is the normalization constant.

We showed in [26] that (4.19) does not vary notably with the angle. Hence, in the experiments we used an approximation of (4.19):

$$\tilde{h}(t) = \text{rect}\left(\frac{t}{T}\right) F^{-1}\{AH(f)(T(f, 0^\circ))^2 \exp(j2\pi f\tau_0)\}. \quad (4.20)$$

## 4.6 Results

We used the electromagnetic solver from Chapter 2 to simulate the measurements of the scene behind a reinforced wall. The number of the targets, as well as their properties, was unknown. The thickness of the wall was assumed to be 0.2 m and the length was similarly 8 m. We considered various bar periods:  $d_{\text{bar}} = 0.15$  m,  $d_{\text{bar}} = 0.1$  m, and



$d_{\text{bar}} = 0.05$  m . The bar diameter was set to  $D_{\text{bar}} = 1$  cm . The adopted relative permittivity of the wall material was  $\epsilon_r = 3 - j0.15$  . The targets were modeled as perfectly conducting cylinders of radius 0.2 m , with respective centers at (1 m, -1.5m) and (-1.5 m, 0.75m) . Besides the targets, there were clutter objects representing furniture and interior walls. We modeled the clutter as dielectric rectangles. The adopted relative permittivity for the clutter was the same as the wall permittivity.

The measuring system consisted of a uniform linear array of  $M = 3$  sensors. The separation between adjacent sensors was 0.4 m . The array moved parallel to the wall at a distance of 0.75 m from the front side of the wall. The array took measurements every 0.2 m, at a total of 32 measurement locations.

The sensors transmitted a Gaussian pulse,  $g(t) = e^{(-at)^2}$  , where  $a = 3e^{-9}\text{s}^{-1}$  . The pulse duration was  $T = 1.2$  ns , which allowed estimating the wall permittivity. We calculated the frequency response from 5 MHz to 2 GHz in 5 MHz steps. We also examined the cases in which the spectrum of the signal,  $G(f)$  , was centered at frequencies  $f_0$  , where  $0 \leq f_0 \leq 1\text{GHz}$  .

The measurements were corrupted with complex additive white Gaussian noise. We calculated the *SNR* with respect to the power of the electric field induced in the sensor. Most of the induced electric field was due to the direct coupling between the sensors. The power of the electric field scattered from the target was several orders of magnitude less than the total electric field induced in the sensor. For this reason, the signal-to-noise ratio

could not be very low.

### 4.6.1 Unknown Bar Parameters

In the first example we set  $d_{\text{bar}} = 15 \text{ cm}$  and  $f_0 = 0$ . We obtained  $\hat{\epsilon}_r = 3$  as the estimate of the wall permittivity. The wall thickness estimation is shown in Fig. 4.5. The dotted curve represents the correlation of the reference pulse and the focused electric field. There is a maximum corresponding to the real wall thickness,  $\hat{w} = 0.2 \text{ m}$ . There are also maxima for  $\hat{w} = 0.3 \text{ m}$  and  $\hat{w} = 0.4 \text{ m}$ . These other maxima are a consequence of the focusing reflections from the bars. The separation between the maxima depends on the bar period. For comparison, we repeated the analysis for the case in which the bar period is  $d_{\text{bar}} = 25 \text{ cm}$  and all other parameters are the same. The result is also shown in Fig. 4.5 (solid line). Again, we have a maximum corresponding to the real wall thickness,  $\hat{w} = 0.2 \text{ m}$ , as well as other spurious maxima. Hence, beamforming does not produce a unique value for the wall thickness.

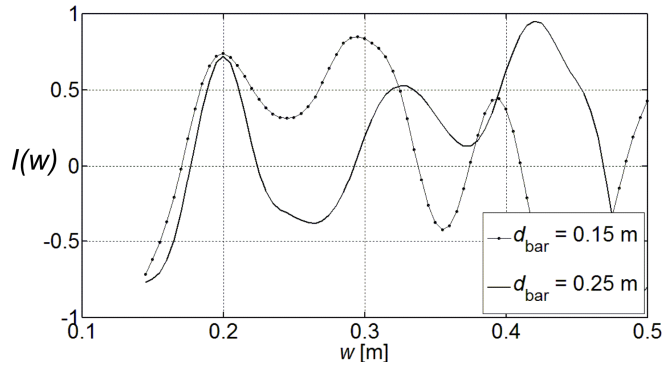
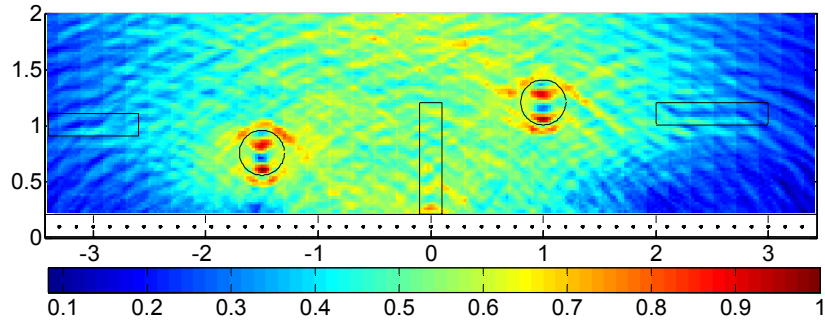
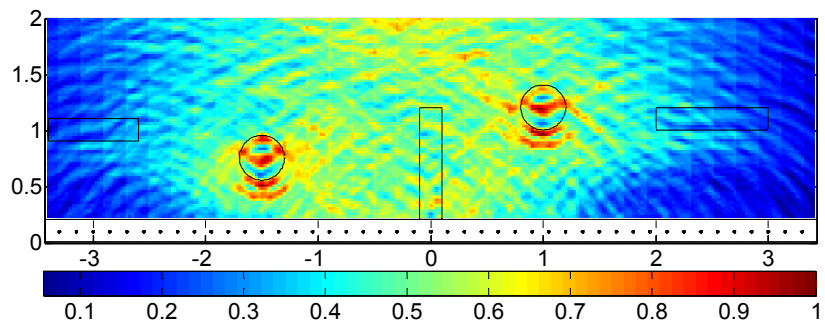


Fig. 4.5: Estimation of wall thickness: correlation of focused electric field and reference pulse.

We estimated the target positions, using the wall permittivity and thickness estimates  $\hat{\epsilon}_r = 3$ ,  $\hat{w} = 0.2$  m and  $\hat{\epsilon}_r = 3$ ,  $\hat{w} = 0.3$  m. We adopted  $SNR = 30$  dB. The power of the field reflected from the targets was 20 dB less than the power of the total field induced in the sensors. Fig. 4.6a shows the image calculated using the exact wall thickness, and Fig. 4.6b shows the image calculated using the first erroneous wall thickness. The circles denote the true positions of the targets, and the rectangles represent the clutter objects. Because the targets were metallic (non-penetrable), the sensors should have identified only small pieces of the targets' contours facing the wall. However, because of the oscillations in the reflected signal, the image resolution is poor even at high  $SNR$ . The contours of the targets are blurred, particularly when the erroneous wall thickness is used (Fig. 4.6b).



(a)



(b)

Fig. 4.6. Scene consisting of two metal targets (circles) placed behind the reinforced wall and clutter objects (rectangles). Image was computed using  $\epsilon_r = 3$ ,  $f_0 = 0$ , and (a)  $w = 0.2$  (real wall thickness) and (b)  $w = 0.3$  (erroneous wall thickness). The waveform distortion was not taken into account. The adopted  $SNR$  was 30 dB.

## 4.6.2 Known Bar Parameters

When the bar characteristics are unknown, the analysis reduces to the case in which the objects are hidden behind a homogeneous wall of the same permittivity. If information about the bars is available, we can refine the estimation by modeling the influence of the bars on the signal waveform. We examined this improvement for various bar periods and different frequency content of the excitation waveform. We repeated the experiment from

Fig. 4.6, assuming the bar parameters were known.

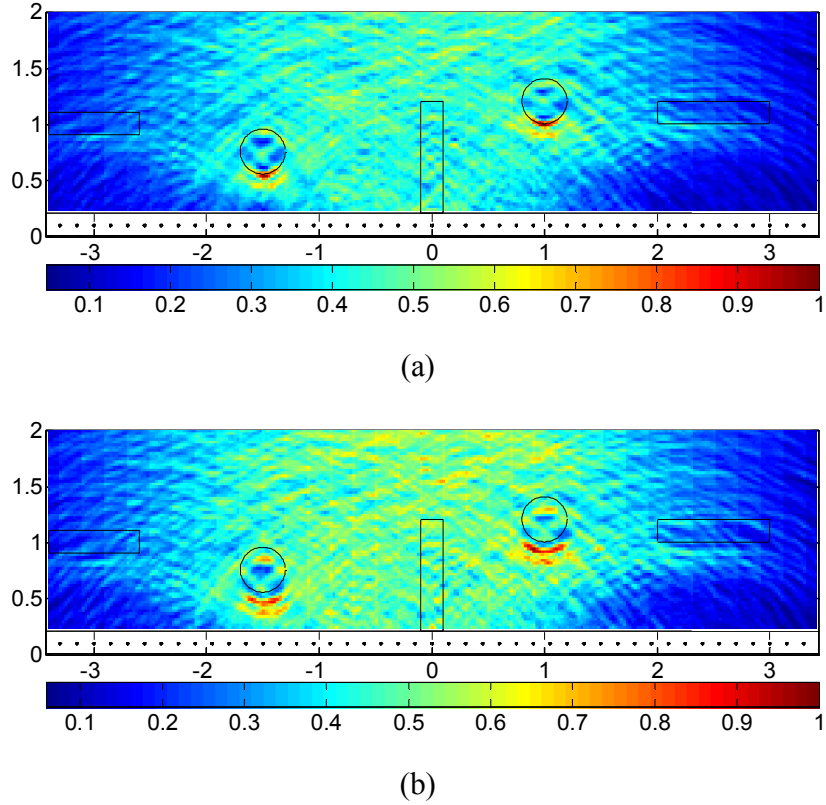


Fig. 4.7: Scene consisting of two metal targets (circles) placed behind the reinforced wall and clutter objects (rectangles). Image was computed using  $\varepsilon_r = 3$ ,  $f_0 = 0$ , and (a)  $w = 0.2$  (real wall thickness) and (b)  $w = 0.3$  (erroneous wall thickness). The waveform distortion was taken into account. The rebar period ( $d_{\text{bar}} = 0.15$  m) was assumed to be known. The adopted  $SNR$  was 30 dB.

We calculated the target positions using  $\hat{\varepsilon}_r = 3$ ,  $\hat{w} = 0.2$  m (Fig. 4.7a) and  $\hat{\varepsilon}_r = 3$ ,  $\hat{w} = 0.3$  m (Fig. 4.7b). The contour estimates (Fig. 4.7a) are significantly sharper when the corrected pulse shape  $\tilde{h}(t)$  is used compared with the case in which the distortion is not modeled (Fig. 4.6a). The pixels with the most intensive colors now clearly represent the pieces of the contours seen by the sensors. In the image obtained using the erroneous

wall thickness the targets are slightly misplaced (Fig. 4.7b).

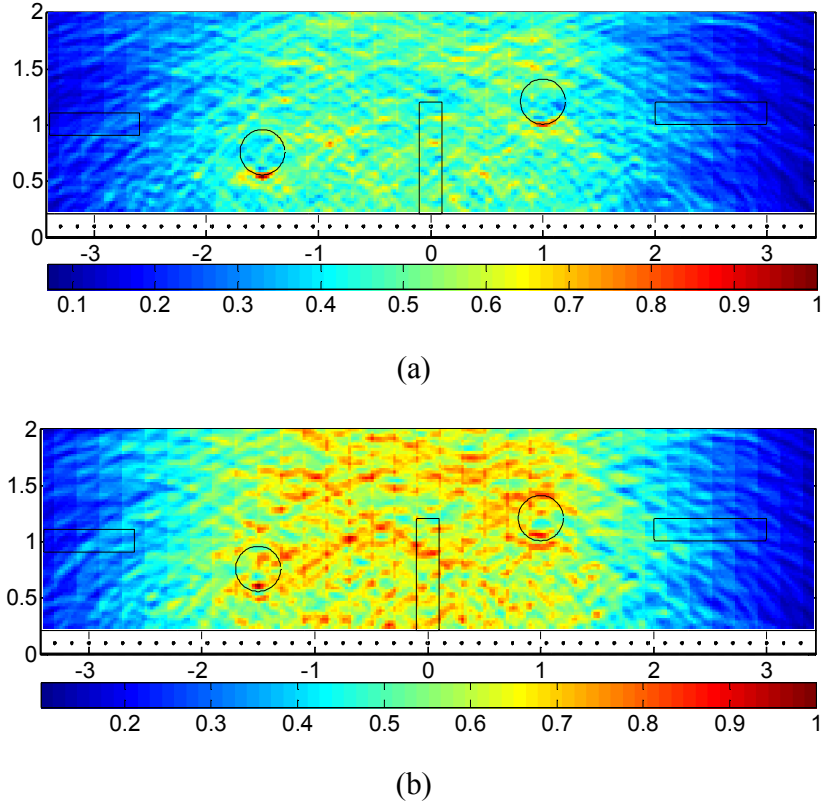
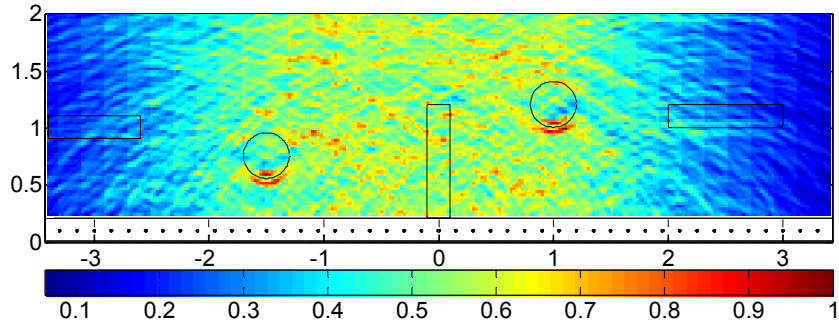


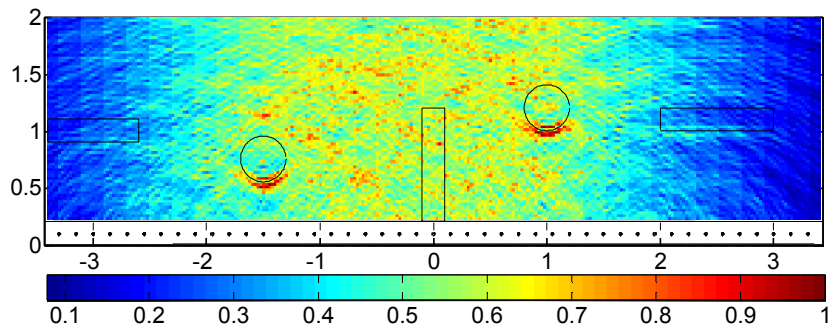
Fig. 4.8: Scene consisting of two metal targets (circles) placed behind the reinforced wall and clutter objects (rectangles). Image was computed for  $SNR = 10$  dB,  $\epsilon_r = 3$ ,  $w = 0.2$ ,  $d_{\text{bar}} = 0.15$  m, and  $f_0 = 0$ . The waveform distortion was (a) taken into account, and (b) not taken into account.

The significance of the waveform correction was more apparent for low  $SNR$ . We computed the image of the same scene for  $SNR = 10$  dB, which was anticipated as the  $SNR$  threshold in this example. The target traces are clearly visible if the bar parameters are known (Fig. 4.8a). In contrast, for low  $SNR$ , the targets cannot be discerned without waveform correction (Fig. 4.8b).

Transmission and reflection coefficients of the reinforced wall are greatly influenced by



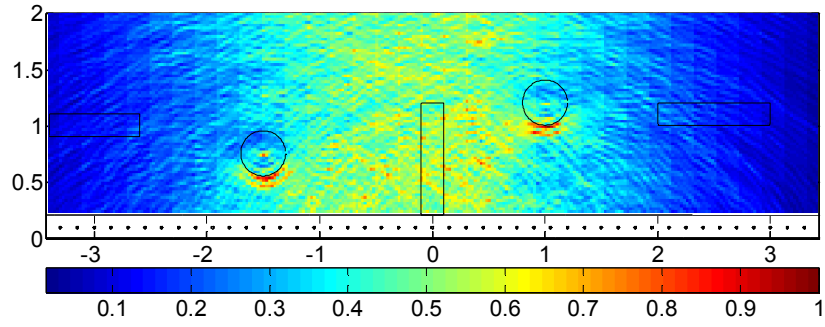
(a)



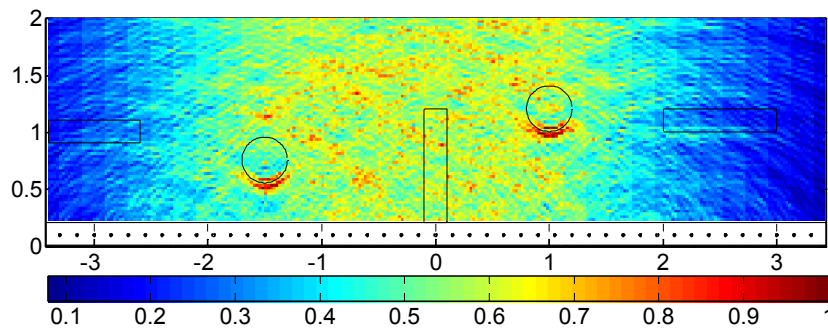
(b)

Fig. 4.9: Scene consisting of two metal targets (circles) placed behind the reinforced wall and clutter objects (rectangles). Image was computed for  $SNR = 10$  dB,  $\epsilon_r = 3$ ,  $w = 0.2$ ,  $d_{\text{bar}} = 0.15$  m, and (a)  $f_0 = 0.5$  GHz and (b) and  $f_0 = 1$  GHz. The waveform distortion was not taken into account.

the ratio of the signal wavelength in the dielectric ( $\lambda_c$ ) and the bar spacing. The investigations in [109], [110] showed that when the ratio  $d_{\text{bar}}/\lambda_c$  is larger than 0.7–0.8, the influence of the bars is reduced. Hence, if the central frequency of the pulse is sufficiently high, the position of the targets can be estimated even in the case for which the bar parameters are unknown. However, the losses in the wall dielectric increase with the frequency. In Fig. 4.9 we show the results obtained without the correction, for  $f_0 = 0.5$  GHz and  $f_0 = 1$  GHz.



(a)

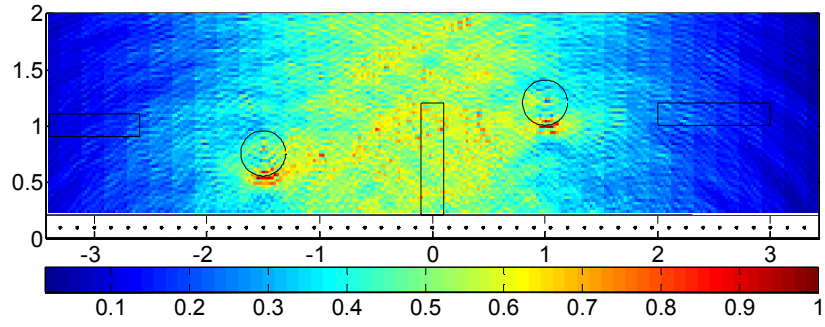


(b)

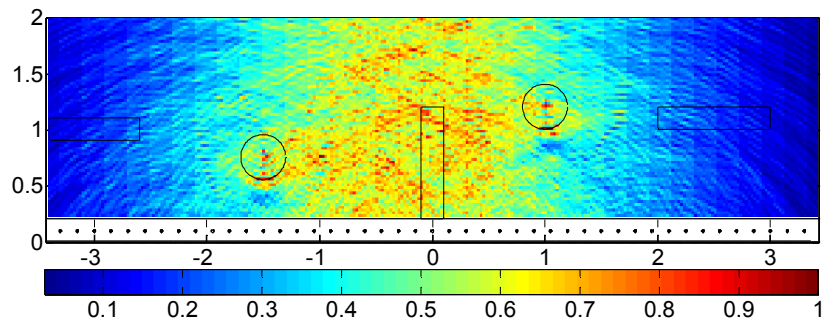
Fig. 4.10: Scene consisting of two metal targets (circles) placed behind the reinforced wall and clutter objects (rectangles). Image was computed for  $SNR = 15$  dB,  $\epsilon_r = 3$ ,  $w = 0.2$ ,  $d_{\text{bar}} = 0.1$  m, and  $f_0 = 0.75$  GHz. The waveform distortion was (a) taken into account, and (b) not taken into account.

We repeated the experiment for  $d_{\text{bar}} = 10$  cm and  $SNR = 15$  dB. According to [109], in this case the rebar would have a major influence for frequencies smaller than 0.7 GHz. We show in Fig. 4.10 the results obtained for  $f_0 = 0.75$  GHz. The improvement is still visible, whereas there is almost no difference at  $f_0 = 1$  GHz.





(a)



(b)

Fig. 4.11: Scene consisting of two metal targets (circles) placed behind the reinforced wall and clutter objects (rectangles). Image was computed for  $SNR = 20$  dB,  $\epsilon_r = 3$ ,  $w = 0.2$ ,  $d_{\text{bar}} = 6$  cm, and  $f_0 = 1$  GHz. The waveform distortion was (a) taken into account, and (b) not taken into account.

Finally, for  $d_{\text{bar}} = 6$  cm, the improvements due to bar modeling should be evident for  $f_0 \leq 1$  GHz. In Fig. 4.11 we show the images computed for  $f_0 = 1$  GHz and  $SNR = 20$  dB, with and without correction.

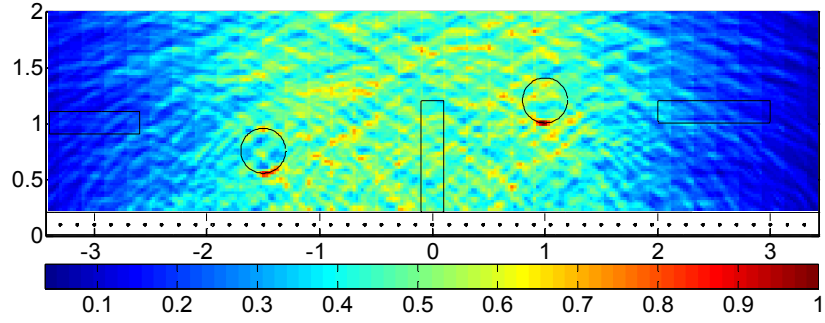


Fig. 4.12: Scene consisting of two metal targets (circles) placed behind the reinforced wall and clutter objects (rectangles). Image was computed for  $SNR = 10$  dB,  $\epsilon_r = 3$ ,  $w = 0.2$ ,  $d_{\text{bar}} = 15$  cm, and  $f_0 = 0$  GHz. Waveform distortion was modeled using an erroneous bar period ( $d_{\text{bar}} = 10$  cm).

We examined the robustness of the algorithm to errors in bar parameters. In Fig. 4.12 we present the results obtained assuming that the bar period was  $d_{\text{bar}} = 10$  cm, while the true value was  $d_{\text{bar}} = 15$  cm. The image does not differ significantly from the image obtained with real wall parameters (Fig. 4.8a).

## 4.7 Summary

We have addressed the important problem in urban warfare of estimating moving targets, such as personnel, behind a reinforced wall, using radar measurements. Reinforced walls significantly attenuate low frequencies and distort the transmitted waveforms. The signals reflected from the objects behind reinforced walls are oscillating in nature and are of long duration because of the bar periodic arrangement. First, we considered the case in which the reinforced wall parameters were completely unknown. We added coherently measured electric fields in various time gates to estimate wall thickness and concrete

permittivity independently. We assumed the availability of measurements of the static scene behind the wall (walls, furniture, etc.) and measurements altered by the appearance of people. The difference between these two measurements is associated with the electromagnetic field scattered from the moving targets. We applied beamforming to the field reflected from the targets to estimate their number and locations. The algorithm performed satisfactorily in the case in which the bar diameter and period were both unknown. However, due to multiple echoes, the target spreads were large. We also analyzed the problem in which the characteristics of the metal rebar were known. We improved the estimation by modeling the waveform distortion due to the bars. The resulting images are focused and accurately represent the contours of the targets. The algorithm is robust to ambiguities in bar parameter values. In addition, the minimal necessary *SNR* is lower compared with the case than in the case where the influence of the bars on the signal shape is ignored.

## **Chapter 5**

# **Electromagnetic Imaging of Hidden 2D**

# **PEC Targets Using Sparse Signal**

# **Modeling**

## **5.1 Introduction**

Electromagnetic scattering has been widely used to infer the properties of concealed objects. Many applications benefit from the research in this field, such as nondestructive testing and subsurface probing. Here, we consider the reconstruction of perfectly conducting targets hidden in a homogeneous medium [42]-[44]. Because of the high contrast, the general algorithms for restoring dielectric profiles, such as the distorted Born iterative method (DBIM) and equivalent Gauss-Newton methods, either do not converge or else converge slowly in this case [3]-[5]. For this reason, many algorithms have been developed particularly for imaging metallic targets, e.g., [45]-[47] and [67]-[71].

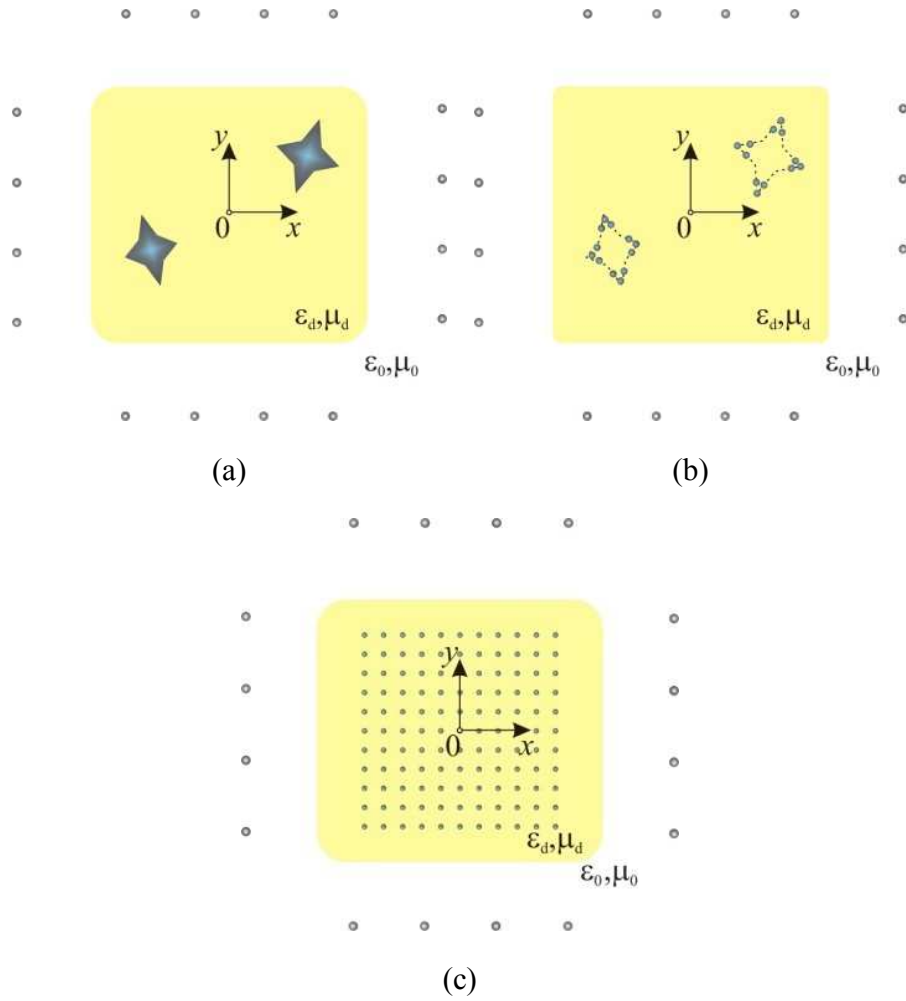


Fig. 5.1: (a) Hidden PEC objects inside dielectric body and sensor array, (b) equivalent sources representing the target, and (c) grid of equivalent sources.

We developed an inverse algorithm that is based on the equivalent-source method [45]-[47] and the surface formulation of the electric-field integral equation described in Chapter 2. We employ  $l_1$  regularization to exploit the sparsity of the induced currents on the surfaces of the targets. We consider a two-dimensional (2D) case; however, the analysis is easily generalized for three-dimensional (3D) geometries.

The original problem with the hidden targets and surrounding sensor array is depicted in

Fig. 5.1a. We assume that, in terms of the scattered field, the targets may be substituted by a few equivalent sources located close to the target contours (Fig. 5.1b). We model the equivalent sources as infinitely long filament currents. In the inverse problem, the goal is to find the locations of the equivalent sources. For this purpose, we define a grid of the equivalent sources uniformly spread in the dielectric interior, as shown in Fig. 5.1c. We derive a linear measurement model and employ  $l_1$  regularization to emphasize the equivalent sources in the vicinity of the target surfaces and thus provide information about their shape.

The other common regularization in inverse scattering problems is  $l_2$  regularization, known for stabilizing the solution. When  $l_2$  regularization is applied, almost every element in the solution is non-zero, even if there are only a few significant elements in the true solution [114]. Hence, because of its smoothing effect,  $l_2$  regularization cannot capture abrupt changes in the shape of the targets. On the other hand,  $l_1$  regularization spots the details in the targets' shape because the induced currents are concentrated close to the wedges and other irregularities. The limitations of  $l_1$  regularization occur in the case of large number of unknowns, particularly when there is strong correlation among the unknown variables. In this case,  $l_1$  regularization tends to select randomly only one variable from the group [114]. Therefore,  $l_1$  regularization reveals the isolated scattering centers rather than the continuous target contours. However, we derive a two-step algorithm to expand the length of the reconstructed portions of the contours.

Sparse localization of buried targets and targets behind walls was considered in [72] and

[22]-[25], respectively. The underlying electromagnetic models assumed far-field measurements and point-like targets. In contrast, we use more detailed models that allow target shape reconstruction.

## 5.2 Electromagnetic Modeling

We consider several perfectly conducting targets hidden inside a homogeneous dielectric body with known permittivity  $\epsilon_d$  and permeability  $\mu_d$ , as illustrated in Fig. 5.1a. The dielectric body is located in a vacuum. The body is interrogated by an array of electromagnetic sensors. We assume electrically thin, perfectly conducting sensors. The sensors are excited by an axial electric field, and the magnetic field is transverse to the  $z$ -axis.

In the inverse problem, instead of real targets, we consider the equivalent sources depicted in Fig. 5.1c. To compute the currents in the equivalent sources, we adapt the electromagnetic model of Chapter 2. We begin by applying the surface equivalence theorem as illustrated in Fig. 5.2.

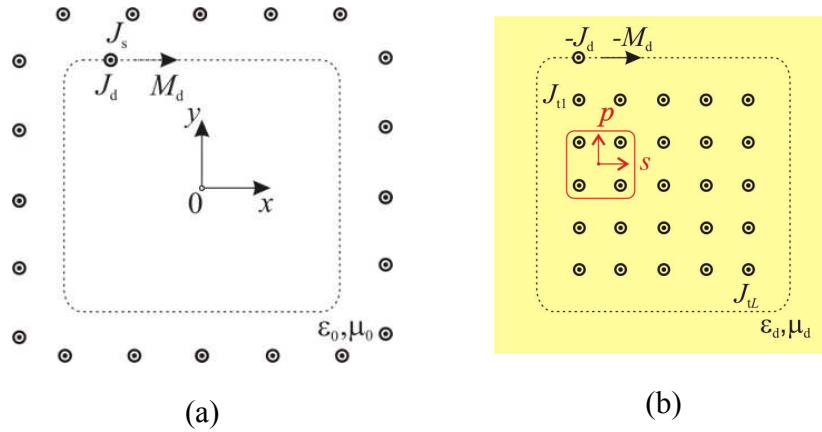


Fig. 5.2: Equivalence theorem: (a) exterior problem and (b) interior problem.

In the exterior problem, we replace the dielectric body (along with the equivalent sources within it) with equivalent surface electric and magnetic currents. The field sources are the electric currents on the sensors, of surface densities  $J_{s,1}, \dots, J_{s,M}$  ( $M$  is the number of the sensors), and the equivalent surface electric and magnetic currents on the dielectric body ( $\mathbf{J}_d, \mathbf{M}_d$ ). The currents are located in a vacuum. (For better readability we use separate notations for the surface currents induced on different bodies.)

In the interior problem, we consider the equivalent surface currents on the interface with reversed direction ( $-\mathbf{J}_d, -\mathbf{M}_d$ ) and the currents on the equivalent sources. The surface densities of the electric currents on the equivalent sources are  $J_{t,1}, \dots, J_{t,L}$ , where  $L$  is the size of the grid. The currents are now located in a homogeneous medium with parameters  $(\epsilon_d, \mu_d)$ .

We divide the dielectric surface into a number of strips (segments) and assume that the current distribution is constant on each strip. We define the vectors of the surface electric



and magnetic current densities on the strips as  $\mathbf{j}_d = [J_{d,1} \ \dots \ J_{d,P}]^T$ ,  $\mathbf{m}_d = [M_{d,1} \ \dots \ M_{d,P}]^T$ , respectively, where  $P$  is the number of strips. Similarly, we define the vectors of the current densities on the sensors and targets as  $\mathbf{j}_s = [J_{s,1} \ \dots \ J_{s,M}]^T$  and  $\mathbf{j}_t = [J_{t,1} \ \dots \ J_{t,L}]^T$ , respectively, where the superscript T denotes transpose.

We use the point-matching technique to derive a set of linear equations from the electric-field integral equations. The integral equations are associated with the exterior and interior cases depicted in Fig. 5.2. In the exterior problem, we use the constraint that the tangential component of the electric field is zero (EFIE constraint) on the surfaces of the sensors and on the inner side of the surface of the dielectric body. In the interior problem, we impose the EFIE constraint on the outer side of the surface of the dielectric body. (We do not impose the EFIE constraint on the equivalent sources, since we do not know *a priori* which of them belong to the targets.) The number of matching points is  $M + P$  in the first case and  $P$  in the second case. The system of equations in matrix form reads

$$\mathbf{e} = -\mathbf{G}\mathbf{j}, \quad (5.1)$$

$$\mathbf{j} = [\mathbf{j}_s \ \mathbf{j}_d \ \mathbf{m}_d \ \mathbf{j}_t]_{N \times 1}^T, \quad N = M + 2P + L, \quad (5.2)$$

$$\mathbf{e} = [E_i(\mathbf{r}_1) \ \dots \ E_i(\mathbf{r}_K)]_{K \times 1}^T, \quad K = M + 2P, \quad (5.3)$$

where  $\mathbf{j}$  is the stacked vector with the current densities,  $\mathbf{G}$  is the system matrix,  $\mathbf{e}$  is the excitation vector,  $\mathbf{r}_k$  is the matching point,  $E_i(\mathbf{r}_k)$  is the impressed electric fields at the

$k$ th matching point, and  $k = 1, \dots, K$ .  $\mathbf{G}(k, n)$  is the electric field at the  $k$ th matching point due to the  $n$ th element of  $\mathbf{j}$ :

$$\mathbf{G}(k, n) = \begin{cases} -j\omega\mu \int_{S_n} g(r) ds & \text{if } \mathbf{j}(n) \in \mathbf{j}_t, \mathbf{j}_d, \mathbf{j}_s \\ \int_{S_n} \frac{dg}{dr} (\mathbf{u}_i \times \mathbf{u}_r) \cdot \mathbf{u}_z ds & \text{if } \mathbf{j}(n) \in \mathbf{m}_d, \end{cases}$$

$$r = |\mathbf{r}'(s) - \mathbf{r}_k|, \quad n = 1, \dots, N, \quad (5.4)$$

where the definitions of all variables are given in Chapter 2.

In the exterior problem,  $\varepsilon = \varepsilon_0$  and  $\mu = \mu_0$ ; in the interior problem,  $\varepsilon = \varepsilon_d$  and  $\mu = \mu_d$ .

We assume that one sensor is excited at a time with a unit impressed electric field. Hence,  $E_i(\mathbf{r}_k)$  is one if  $\mathbf{r}_k$  is on the excited sensor (transmitter),  $k = 1, \dots, K$ ; otherwise it is zero.

## 5.3 Sparse Signal Processing

### 5.3.1 Measurement Model

The current distribution on the targets varies with the different excitations (i.e., incident angles). Therefore, we cannot exploit simultaneously data collected under different illumination directions (multiview measurement configuration). However, we can superimpose the images of the targets obtained for different incident angles and thus

enlarge the reconstructed portion of the target contours. Hence, we first consider the case in which only one sensor in the array transmits the incident field and all sensors receive the scattered field (singleview/multistatic configuration) and later proceed to the case in which several sensors are the transmitters (multiview/multistatic configuration).

We rearrange (5.3) in order to separate the currents on the sensors from the currents on the equivalent sources and the dielectric:

$$\mathbf{e}_i = -[\mathbf{G}_s \quad \mathbf{G}_2] \begin{bmatrix} \mathbf{j}_s \\ \mathbf{j}_2 \end{bmatrix}, \quad \mathbf{j}_2 = [\mathbf{j}_d^T \quad \mathbf{m}_d^T \quad \mathbf{j}_t^T]^T, \quad i=1, \dots, M, \quad (5.5)$$

where  $\mathbf{G}_s \in C^{K \times M}$  is the matrix composed of the first  $M$  columns of the matrix  $\mathbf{G}$  defined in (5.4), and  $\mathbf{G}_2 \in C^{K \times (2P+L)}$  is the matrix composed of the remaining  $L+2P$  columns of  $\mathbf{G}$ . The subscript  $i$  in the excitation vector denotes the index of the transmitting sensor. (The dependence of the currents on  $i$  is assumed and suppressed.)

In the implementation of the inverse algorithm,  $\mathbf{j}_s$  is the vector of the known current densities in the sensors due to the real targets (instead of the equivalent sources). Hence, (5.3) is only approximately satisfied:

$$\mathbf{G}_2 \mathbf{j}_2 \approx -\mathbf{e}_i - \mathbf{G}_s \mathbf{j}_s. \quad (5.6)$$

The unknowns are the densities of the currents on the equivalent sources ( $\mathbf{j}_t$ ) and the densities of the currents on the dielectric surface ( $\mathbf{j}_d, \mathbf{m}_d$ ). If we suppose that the equivalent sources are removed from the dielectric, (5.6) becomes

$$\mathbf{G}_2 \mathbf{j}_{20} = \mathbf{e}_i - \mathbf{G}_s \mathbf{j}_{s0}, \quad \mathbf{j}_{20} = \begin{bmatrix} \mathbf{j}_{d0}^T & \mathbf{m}_{d0}^T & \mathbf{0}^T \end{bmatrix}^T, \quad (5.7)$$

where  $\mathbf{j}_{s0}$  is the vector of the electric current densities on the sensors,  $\mathbf{j}_{d0}$  is the vector of the equivalent electric current densities, and  $\mathbf{m}_{d0}$  is the vector of the equivalent magnetic current densities. We subtract (5.7) from (5.6) to obtain the measurement model. After inclusion of additive noise, the measurement model reads

$$\mathbf{y} = \mathbf{G}_2 \mathbf{x} + \mathbf{w}, \quad (5.8)$$

$$\mathbf{y} = -\mathbf{G}_s (\mathbf{j}_s - \mathbf{j}_{s0}), \quad (5.9)$$

$$\mathbf{x} = \begin{bmatrix} (\Delta \mathbf{j}_d)^T & (\Delta \mathbf{m}_d)^T & (\mathbf{j}_t)^T \end{bmatrix}^T, \quad (5.10)$$

and

$$\Delta \mathbf{j}_d = \mathbf{j}_d - \mathbf{j}_{d0}, \quad \Delta \mathbf{m}_d = \mathbf{m}_d - \mathbf{m}_{d0}. \quad (5.11)$$

Here,  $\mathbf{y}$  is the known measurement vector because  $\mathbf{j}_{s0}$  is numerically computed from (5.11),  $\mathbf{x}$  is the unknown parameter vector, and  $\mathbf{w}$  is the noise term that includes both the measurement noise and modeling errors.

We are interested in the unknown current densities on the equivalent sources ( $\mathbf{j}_t$ ). The vectors  $\Delta \mathbf{j}_d$  and  $\Delta \mathbf{m}_d$  are considered as nuisance parameters.

### 5.3.2 Current Distribution Model

If the electrical size of the dielectric is large and/or it has complex shape, the number of the unknowns ( $\Delta \mathbf{j}_d$ ,  $\Delta \mathbf{m}_d$ ) necessary to adequately model the dielectric may be large. In order to reduce the number of unknowns, we take advantage of polynomial expansion. We define the polynomials as follows:

$$\Delta J_d(s) \approx \sum_{r=0}^R \alpha_r s^r, \quad \Delta M_d(s) \approx \sum_{r=0}^R \beta_r s^r, \quad 0 \leq s \leq 1, \quad (5.12)$$

where  $\Delta J_d(s)$  and  $\Delta M_d(s)$  are the respective differences in the surface densities of the equivalent electric and magnetic currents due to the presence of the targets,  $R$  is the polynomial order,  $\alpha_r$  is the  $r$ th coefficient of the electric current approximation,  $\beta_r$  is the  $r$ th coefficient of the magnetic current approximation, and  $s$  is the length coordinate along the dielectric contour. (Depending on the size of the dielectric, it may be necessary to first divide the contour into several segments and then define a polynomial for each of the segments.) The elements of the vectors  $\Delta \mathbf{j}_d$  and  $\Delta \mathbf{m}_d$  are, respectively, samples of the polynomials  $\Delta J_d(s)$  and  $\Delta M_d(s)$  at the matching points. Their relationship in matrix form reads

$$\begin{bmatrix} \Delta \mathbf{j}_d \\ \Delta \mathbf{m}_d \end{bmatrix} = \begin{bmatrix} \mathbf{H}_d & 0 \\ 0 & \mathbf{H}_d \end{bmatrix} \begin{bmatrix} \boldsymbol{\alpha} \\ \boldsymbol{\beta} \end{bmatrix}, \quad (5.13)$$

$$\mathbf{H}_d = [\mathbf{h}_1 \quad \dots \quad \mathbf{h}_P]_{P \times (R+1)}^T, \quad (5.14)$$

$$\mathbf{h}_p = [s_p^0 \quad \dots \quad s_p^R]^\top, \quad s_p = (p-0.5)/P, \quad p = 1, \dots, P, \quad (5.15)$$

and

$$\boldsymbol{\alpha} = [\alpha_0 \quad \dots \quad \alpha_R]^\top, \quad \boldsymbol{\beta} = [\beta_0 \quad \dots \quad \beta_R]^\top, \quad (5.16)$$

where  $\mathbf{H}_d$  is the transformation matrix,  $s_p$  is the length coordinate of the  $p$ th matching point, and  $\boldsymbol{\alpha}$  and  $\boldsymbol{\beta}$  are the vectors of the polynomial coefficients.

We use the currents on the equivalent sources to model the induced currents on the contours of the targets. It is expected that equivalent sources with significant currents will appear in groups around the scattering centers. Hence, we divide the equivalent sources into small groups, where each group is associated with a potential scattering center. Groups are identical, consisting of  $V \times V$  equivalent sources. An example of a  $2 \times 2$  group enclosed by a solid line is given in Fig. 5.2b. We assume that the currents on the equivalent sources in each group are the samples from the unknown 2D polynomial distribution

$$J_t^{(k)}(s, p) \approx \sum_{i=0}^{V-1} \sum_{j=0}^{V-1} \sigma_{ij}^{(k)} s^i t^j, \quad -1 \leq s, t \leq 1,$$

$$k = 1, \dots, N_g, \quad N_g = L/V^2, \quad (5.17)$$

where  $J_t^{(k)}(s, p)$  is the 2D polynomial of the  $k$ th group;  $\sigma_{ij}^{(k)}$  are the polynomial coefficients in the  $k$ th group,  $i, j = 0, \dots, V-1$ ;  $s$  and  $t$  are the local coordinates defined

in Fig. 5.2b; and  $N_g$  is total number of groups. The matrix relationship between the current densities on the equivalent sources and the polynomial coefficients reads

$$\mathbf{j}_t^{(k)} = U\boldsymbol{\sigma}^{(k)}, \quad (5.18)$$

$$U = [\mathbf{u}_1 \quad \dots \quad \mathbf{u}_{V^2}]_{V^2 \times V^2}^T, \quad (5.19)$$

$$\mathbf{u}_i = [s_i^0 t_i^0 \quad s_i^0 t_i^1 \quad \dots \quad s_i^{V-1} t_i^{V-1}]_{V^2 \times 1}^T, \quad i = 1, \dots, V^2, \quad (5.20)$$

and

$$\boldsymbol{\sigma}^{(k)} = [\sigma_{00}^{(k)} \quad \sigma_{01}^{(k)} \quad \dots \quad \sigma_{V-1 V-1}^{(k)}]_{V^2 \times 1}^T, \quad (5.21)$$

where  $\mathbf{j}_t^{(k)}$  is the vector of the electric current densities on the equivalent sources in the  $k$ th group,  $\boldsymbol{\sigma}^{(k)}$  is the vector of the polynomial coefficients in the  $k$ th group,  $(s_i, t_i)$  are the local coordinates of the  $i$ th equivalent source,  $i = 1, \dots, V^2$ , in the  $k$ th group, and  $U$  is the transformation matrix. The currents in all groups are stacked in a vector

$$\mathbf{j}_t = H_t \boldsymbol{\sigma}, \quad (5.22)$$

$$\mathbf{j}_t = \left[ (\mathbf{j}_t^{(1)})^T \quad \dots \quad (\mathbf{j}_t^{(N_g)})^T \right]^T, \quad (5.23)$$

$$\boldsymbol{\sigma} = \left[ (\boldsymbol{\sigma}^{(1)})^T \quad \dots \quad (\boldsymbol{\sigma}^{(N_g)})^T \right]^T, \quad (5.24)$$

and

$$\mathbf{H}_t = \text{blkdiag} \left( \underbrace{\mathbf{U}, \dots, \mathbf{U}}_{\times N_g} \right). \quad (5.25)$$

### 5.3.3 Single Step Algorithm

We substitute the current approximations (5.13) and (5.22) in (5.8). The measurement model in the single-step algorithm reads

$$\mathbf{y} = \mathbf{G}_2 \boldsymbol{\Psi} \mathbf{z} + \mathbf{w}, \quad \mathbf{x} = \boldsymbol{\Psi} \mathbf{z}, \quad (5.26)$$

$$\mathbf{z} = [\boldsymbol{\alpha}^\top \quad \boldsymbol{\beta}^\top \quad \boldsymbol{\sigma}^\top]^\top, \quad \boldsymbol{\Psi} = \begin{bmatrix} \mathbf{H}_d & \mathbf{0} & \mathbf{0} \\ \mathbf{0} & \mathbf{H}_d & \mathbf{0} \\ \mathbf{0} & \mathbf{0} & \mathbf{H}_t \end{bmatrix}, \quad (5.27)$$

where  $\mathbf{z}$  is the new unknown vector and  $\boldsymbol{\Psi}$  is the transformation matrix.

The scattering centers are parsimonious on the target surface; therefore we want to reduce the number of groups with non-zero currents. In addition, to better estimate the contours of the targets, we want the polynomials to decrease quickly in the direction normal to the target surface. Hence, we aim to reduce the number the significant elements of  $\mathbf{j}_t^{(k)}$ . These two desired characteristics are obtained by minimizing the  $l_1$  norm of the vector  $\mathbf{j}_t$ . Hence, we look for the solution

$$\hat{\mathbf{z}} = \arg \min_z \left\{ \|\mathbf{G}_2 \boldsymbol{\Psi} \mathbf{z} - \mathbf{y}\|_2^2 + \gamma^{(1)} \|\mathbf{j}_t\|_1 \right\}, \quad (5.28)$$



where the  $l_2$ -norm on the right-hand side is the data fidelity term and the  $l_1$ -norm is the sparsity constraint. The scalar  $\gamma^{(i)}$  is the regularization parameter in a single-step algorithm that balances the tradeoff between those two constraints. We discuss the selection of the regularization parameter in detail in Section 5.4. To solve (5.28), we use CVX [115], a package for specifying and solving convex programs [116]. We compute the corresponding image as

$$I(l) = |\hat{\mathbf{j}}_i(l)| / \max(|\hat{\mathbf{j}}_i|), \quad (5.29)$$

where  $I(l)$  is the  $l$ th pixel of the image and  $\hat{\mathbf{j}}_i(l)$  is the  $l$ th element of the solution vector. In the case of multiple incidences (i.e., multiple transmitters), we compute the images obtained for each transmitting sensor separately (5.29), and then we add those images.

### 5.3.4 Two-Step Algorithm

We now consider a two-step extension of the algorithm. We refer to the solution of (5.28), i.e.,  $\hat{\mathbf{j}}_i$ , as the first-step estimate (due to the  $i$ th incidence). Because of the  $l_1$  regularization, most elements of  $\hat{\mathbf{j}}_i$  are negligible. If the targets are electrically large, the one-step procedure may not be sufficient to estimate their shapes. The purpose of the two-step algorithm is to enlarge the reconstructed portion of the target surfaces.

As in the single-step algorithm, we assume that the  $i$ th sensor is excited. We denote by  $\mathcal{Q}_i$  the subset of indices corresponding to the non-zero elements of  $\hat{\mathbf{j}}_i$ ; i.e.,

$Q_1 = \{l \in Q \mid \hat{j}_t(l) > \delta\}$ , where  $\delta$  is the adopted threshold and  $Q = \{1, 2, \dots, L\}$ . We denote by  $Q_2$  the complementary set of indices, i.e.;  $Q_2 = Q \setminus Q_1$ . We formulate the system of linear equations in the same manner as in the single-step algorithm. The only difference is that, in addition to the boundary surfaces of the sensors and dielectric, we also enforce the EFIE constraint on the equivalent sources with indices in  $Q_1$ . Hence, we rewrite (5.6) as

$$\mathbf{G}_2 \mathbf{j}_2^{(2)} \approx -\mathbf{e}_i - \mathbf{G}_s \mathbf{j}_s, \quad \mathbf{j}_2^{(2)} = \left[ \left( \mathbf{j}_d^{(2)} \right)^T \quad \left( \mathbf{m}_d^{(2)} \right)^T \quad \left( \mathbf{j}_t^{(2)} \right)^T \right]^T, \quad (5.30)$$

where  $\mathbf{G}_s \in C^{(K+|Q_1|) \times M}$  and  $\mathbf{G}_2 \in C^{(K+|Q_1|) \times (2P+L)}$  are the submatrices of the system matrix  $\mathbf{G} \in C^{(K+|Q_1|) \times N}$  (the symbol  $|\cdot|$  stands for the cardinality of the set). The definitions of the vectors  $\mathbf{j}_d^{(2)}$ ,  $\mathbf{m}_d^{(2)}$  and  $\mathbf{j}_t^{(2)}$  are identical to those as in (5.6), except that (2) in the superscript refers to the second iteration. The size of the excitation vector is now  $\mathbf{e}_i \in C^{(K+|Q_1|) \times 1}$ . The observed vector  $\mathbf{j}_s$  remains the same as in the first step.

We now model the response of the system consisting of the dielectric body and the equivalent sources from  $Q_1$ , i.e., the first estimate of the targets. The equivalent sources from  $Q_2$  have been removed. As in (5.7), we define

$$\mathbf{G}_2 \mathbf{j}_{20}^{(2)} = -\mathbf{e}_i - \mathbf{G}_s \mathbf{j}_{s0}^{(2)}, \quad \mathbf{j}_{20}^{(2)} = \left[ \left( \mathbf{j}_{d0}^{(2)} \right)^T \quad \left( \mathbf{m}_{d0}^{(2)} \right)^T \quad \left( \tilde{\mathbf{j}}_{t0}^{(2)} \right)^T \right]^T, \quad (5.31)$$

and

$$\tilde{\mathbf{j}}_{i_0}^{(2)}(i) = \begin{cases} \mathbf{j}_{i_0}^{(2)}(i), & \text{if } i \in Q_1 \\ 0, & \text{if } i \in Q_2 \end{cases}. \quad (5.32)$$

Here,  $\mathbf{j}_{s_0}^{(2)}$  is the vector of the electric current densities on the sensors,  $\mathbf{j}_{d_0}^{(2)}$  and  $\mathbf{m}_{d_0}^{(2)}$  are the vectors of the respective densities of the equivalent electric and magnetic currents on the dielectric, and  $\mathbf{j}_{i_0}^{(2)} \in C^{|Q_1| \times 1}$  is the vector of the electric current densities on the equivalent sources from  $Q_1$ . The vector  $\tilde{\mathbf{j}}_{i_0}^{(2)} \in C^{|Q| \times 1}$  has the same non-zero elements as the vector  $\mathbf{j}_{i_0}^{(2)}$ . We introduce  $\tilde{\mathbf{j}}_{i_0}^{(2)}$  to insure that vectors  $\mathbf{j}_{2_0}^{(2)}$  and  $\mathbf{j}_2^{(2)}$  are the same size.

To derive the measurement model in the second step, we follow the same procedure as in the single-step algorithm. We subtract (5.31) from (5.30) and apply the polynomial expansion described in Section 5.3.2. We obtain

$$\mathbf{y}^{(2)} = \mathbf{G}_2 \Psi \mathbf{z}^{(2)} + \mathbf{w}^{(2)}, \quad (5.33)$$

where  $\mathbf{y}^{(2)}$  is the known measurement vector in the second step,

$$\mathbf{y}^{(2)} = -\mathbf{G}_s (\mathbf{j}_s^{(2)} - \mathbf{j}_{s_0}^{(2)}), \quad (5.34)$$

and vector  $\mathbf{j}_{s_0}^{(2)}$  is numerically computed from (5.31). The unknown vector in the second step is

$$\mathbf{z}^{(2)} = \left[ \left( \boldsymbol{\alpha}_d^{(2)} \right)^T \quad \left( \boldsymbol{\beta}_d^{(2)} \right)^T \quad \left( \Delta \mathbf{j}_t^{(2)} \right)^T \right]^T, \quad (5.35)$$

with

$$\Delta \mathbf{j}_t^{(2)} = \mathbf{j}_t^{(2)} - \tilde{\mathbf{j}}_{t0}^{(2)}, \quad (5.36)$$

$$\mathbf{x}^{(2)} = \left[ \left( \Delta \mathbf{j}_d^{(2)} \right)^T \quad \left( \Delta \mathbf{m}_d^{(2)} \right)^T \quad \left( \Delta \mathbf{j}_t^{(2)} \right)^T \right]^T, \quad (5.37)$$

and

$$\mathbf{x}^{(2)} = \Psi_{\mathbf{z}} \mathbf{z}^{(2)}. \quad (5.38)$$

All variables have already been defined in Section 5.3.2, except that the superscript (2) again refers to the second step. The minimization function now reads

$$\hat{\mathbf{z}}^{(2)} = \arg \min_z \left\{ \left\| \mathbf{G}_2 \Psi_{\mathbf{z}} \mathbf{z}^{(2)} - \mathbf{y}^{(2)} \right\|_2^2 + \gamma^{(2)} \left\| \Delta \mathbf{j}_t^{(2)} \right\|_1 \right\}, \quad (5.39)$$

where  $\gamma^{(2)}$  is the regularization parameter in the second step. The computed image for a single incidence in the two step algorithm is

$$I(l) = \left| \hat{\mathbf{j}}_t(l) \right| / \max \left( \left| \hat{\mathbf{j}}_t \right| \right) + \left| \Delta \hat{\mathbf{j}}_t^{(2)}(l) \right| / \max \left( \left| \Delta \hat{\mathbf{j}}_t^{(2)} \right| \right), \quad l = 1, \dots, L, \quad (5.40)$$

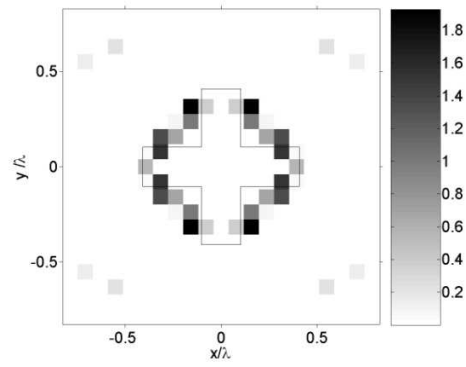
where  $\Delta \hat{\mathbf{j}}_t^{(2)}$  is the vector with the estimated currents on the equivalent sources in the second step. The complete image is obtained as in the first step, by superimposing images computed for different incidences.

## 5.4 Numerical Experiments

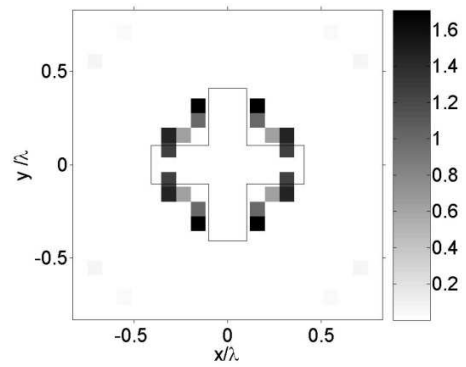
### 5.4.1 One-Step Estimation

We examined the ability of the algorithm to reconstruct the geometrical features of hidden PEC targets with various shapes. We considered an embedding dielectric body with a square cross-section and side length 30 cm. The relative permittivity of the dielectric was assumed to be  $\epsilon_r = 3 - j0.3$ . The operating frequency was  $f = 1$  GHz. The scene was interrogated by an array of 16 transducers, as in Fig. 5.1. The standoff distance of the array from the dielectric surface was 45 cm. The separation between the adjacent sensors was 30 cm.

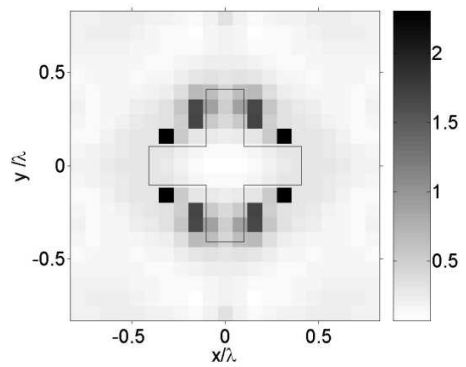
For the first example, we considered a single target with the cross-section in the shape of a cross. The target contour is denoted by the solid line in Fig. 5.3. Because the circumference of the dielectric was electrically large, we defined the polynomials that approximated the equivalent currents on each side of the dielectric body separately. The order of the polynomials depends primarily on the electrical length of the segments. Hence, it can be determined in advance without knowing the target. We adopted  $R = 7$ .



(a)



(b)



(c)

Fig. 5.3: Reconstruction of cross-like cylinder (“noiseless” model). Results were computed using (a)  $\gamma^{(1)} = 1.4$ , (b)  $\gamma^{(1)} = 1.8$ , and (c)  $\gamma^{(1)} = 2$ .

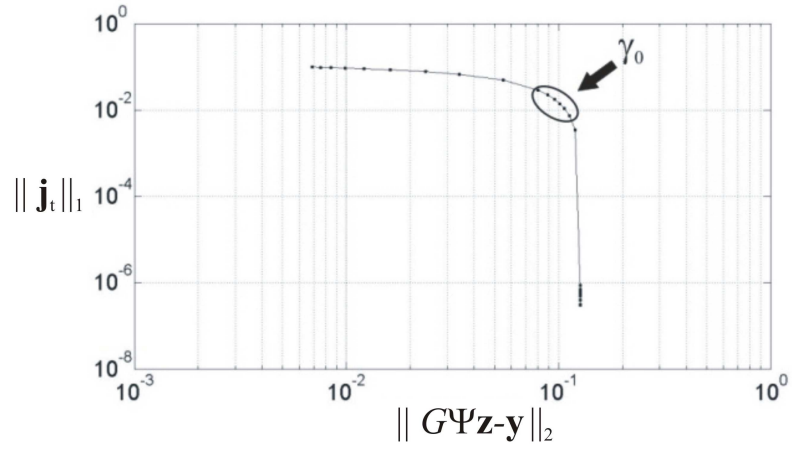
We studied the influence of the regularization parameter  $\gamma^{(1)}$  on the target reconstruction. We divided the interior of the dielectric into a uniform grid with equal steps in the  $x$  and  $y$  directions:  $\Delta_x = \Delta_y = 0.075\lambda$ . (The number of the grid nodes was  $L = 21^2 = 441$ .) We first considered a trivial case in which each group of the equivalent sources consisted of a single source ( $V = 1$ ).

A common way to compute the regularization parameter is by means of the L-curve [117]. The knee of the L-curve determines a trade-off between the stability (represented by the solution norm  $\|\hat{\mathbf{j}}_t\|_1$ ) and accuracy (measured by the discrepancy  $\|\mathbf{G}_2\Psi\mathbf{z} - \mathbf{y}\|_2$ ) of the reconstruction. We show in Fig. 5.4a the L-curve computed for the cross-like target when the sensor in the lower left corner was excited. The shape of the curve is typical for inverse scattering problems. The values of the regularization parameter corresponding to the knee of the L-curve are labeled  $\gamma_0$ . We also computed the number of non-zero elements (i.e.,  $l_0$ -norm) of the solution vector  $\hat{\mathbf{j}}_t$  versus the regularization parameter. Our numerical experiments showed that this curve also exhibits the typical shape as illustrated in Fig. 5.4b. We observed three distinctive regions:  $\gamma_0$  (the same as in the case of the L-curve), in which the minimal  $l_0$ -norm was achieved;  $\gamma^{(1)} > \gamma_0$ , in which the  $l_0$ -norm diverged (i.e., the solution was not sparse anymore); and  $\gamma^{(1)} < \gamma_0$ , in which the  $l_0$ -norm was large but the solution was still sparse. We obtained the best reconstructions for  $\gamma^{(1)} \in \gamma_0$  and for the values that were slightly less than  $\min(\gamma_0)$ . Hence, both curves identically determined the “optimal” parameter value, although we found the utilization of  $l_0$ -norm to be more practical. The selected parameter  $\gamma^{(1)}$  was approximately

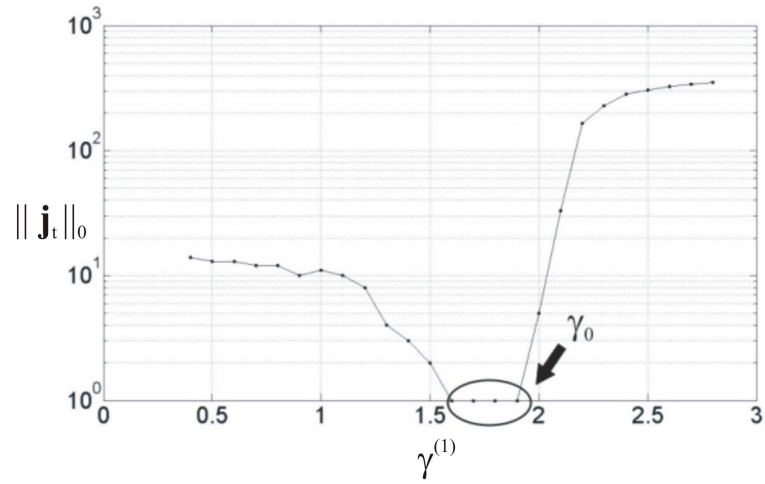
the same for all excitations, which reduced the computational cost. In Fig. 5.3, we plot the target images computed for several characteristic values of parameter  $\gamma^{(i)}$ : (a)  $\gamma^{(i)} = 1.4 < \gamma_0$ , (b)  $\gamma^{(i)} = 1.8 \in \gamma_0$ , and (c)  $\gamma^{(i)} = 2 > \gamma_0$ . We assumed no additional noise.

As predicted by the  $l_0$ -norm, the most compact solution was obtained for  $\gamma^{(i)} = 1.8 \in \gamma_0$ . If the value of the regularization parameter was slightly less than  $\min(\gamma_0)$ , a few additional points on the target contour were revealed. If  $\gamma^{(i)}$  was further decreased, the solution became meaningless. Similarly, if  $\gamma^{(i)}$  was larger than  $\max(\gamma_0)$  we obtained a blurred image with no additional information about the target's shape.





(a)



(b)

Fig. 5.4: (a) L-curve and (b)  $l_0$ -curve for target of Fig. 5.3.

For comparison purposes, we also reconstructed the target shape using LSM [51]-[59] and MUSIC [60]-[66]. In LSM one tries to focus the scattered fields obtained for different incident angles as they emanate from the equivalent source in the interior of the target. Mathematically, one seeks to solve the matrix equation

$$\mathbf{F}\mathbf{g}(t_l) = \mathbf{f}(t_l), \quad l = 1, \dots, L, \quad (5.41)$$

$$\mathbf{F} = \begin{bmatrix} E_s(\mathbf{r}_1, \mathbf{r}_1) & \cdots & E_s(\mathbf{r}_1, \mathbf{r}_M) \\ \vdots & \ddots & \vdots \\ E_s(\mathbf{r}_M, \mathbf{r}_1) & \cdots & E_s(\mathbf{r}_M, \mathbf{r}_M) \end{bmatrix}, \quad (5.42)$$

$$\mathbf{f}(\mathbf{t}_l) = \begin{bmatrix} G(\mathbf{r}_1, \mathbf{t}_l) \\ \vdots \\ G(\mathbf{r}_M, \mathbf{t}_l) \end{bmatrix}, \quad (5.43)$$

where  $\mathbf{r}_i$ ,  $i=1, \dots, M$ , are the locations of the sensors,  $E_s(\mathbf{r}_i, \mathbf{r}_j)$  is the scattered field at the  $i$ th sensor when the  $j$ th sensor is excited,  $\mathbf{t}_l$ ,  $l=1, \dots, L$ , are the locations of the equivalent sources,  $G(\mathbf{r}_i, \mathbf{t}_l)$  is the scattered field (Green's function) at  $\mathbf{r}_i$  due to the equivalent sources located at  $\mathbf{t}_l$ , and  $\mathbf{F}$  is the multistatic measurement matrix. The norm of the solution vector  $\mathbf{g}(\mathbf{t}_l)$  is the so-called indicator function, which is shown to be finite for the points inside scatterers and infinite for the points that are outside scatterers. Here, we assume that the observed values are the induced currents instead of the scattered electric field. Hence, in this case  $\mathbf{F}$  reads

$$\mathbf{F} = \begin{bmatrix} \Delta J_s(\mathbf{r}_1, \mathbf{r}_1) & \cdots & \Delta J_s(\mathbf{r}_1, \mathbf{r}_M) \\ \vdots & \ddots & \vdots \\ \Delta J_s(\mathbf{r}_M, \mathbf{r}_1) & \cdots & \Delta J_s(\mathbf{r}_M, \mathbf{r}_M) \end{bmatrix}, \quad (5.44)$$

$$\Delta J_s(\mathbf{r}_i, \mathbf{r}_j) = J_s(\mathbf{r}_i, \mathbf{r}_j) - J_{s0}(\mathbf{r}_i, \mathbf{r}_j), \quad (5.45)$$

$$\mathbf{f}(\mathbf{t}_l) = \begin{bmatrix} J_s(\mathbf{r}_1, \mathbf{t}_l) \\ \vdots \\ J_s(\mathbf{r}_M, \mathbf{t}_l) \end{bmatrix}, \quad (5.46)$$

where  $J_s(\mathbf{r}_i, \mathbf{r}_j)$  and  $J_{s0}(\mathbf{r}_i, \mathbf{r}_j)$  are the currents in the  $i$ th sensor when the  $j$ th sensor is excited, with and without targets, respectively. Likewise,  $J_s(\mathbf{r}_i, \mathbf{t}_l)$  is the current in the  $i$ th sensor due to the equivalent source at  $\mathbf{t}_l$  (excited by the impressed electric field).

We computed (5.44)-(5.46) using our forward model of Chapter 2. We solved (5.41) by means of the singular value decomposition (SVD), where we applied the regularization from [58]. The target image was obtained by plotting the reciprocal value of  $\|\mathbf{g}(\mathbf{t}_l)\|$  for all sampling points. We show the result in Fig. 5.5a. As opposed to the sparse processing algorithm which recovered the target shape, the LSM recovered only its complex hull. However, LSM estimated better the ending points of the target. We note that we did not use the standard formulation of LSM in which electric fields are focused ((5.44)-(5.46)). Instead, we focused the observed currents ((5.41)-(5.43)) which might slightly worsen the performance. However, similar performance of the standard LSM was reported in [53] where a cross-like cylinder in free space was considered.

The MUSIC algorithm employs the singular vectors associated with the vanishing (or small) singular values of the multistatic data matrix  $\mathbf{F}$ . The target image is computed as

$$I(\mathbf{t}_l) = 1 / \left( \sum_{\sigma_m < \delta} (\mathbf{f}(\mathbf{t}_l)^H \mathbf{u}_m)^2 \right), \quad (5.47)$$

where  $\sigma_m$ ,  $m = 1, \dots, M$ , are the singular values,  $\mathbf{u}_m$  are the associated singular vectors of matrix  $\mathbf{F}$  (given by (5.44)),  $\delta$  is the threshold, and  $\mathbf{f}$  is defined in (5.46). We determined the optimal value for  $\delta$  empirically. The image obtained using MUSIC is

shown in Fig. 5b, and very accurately represents the target.

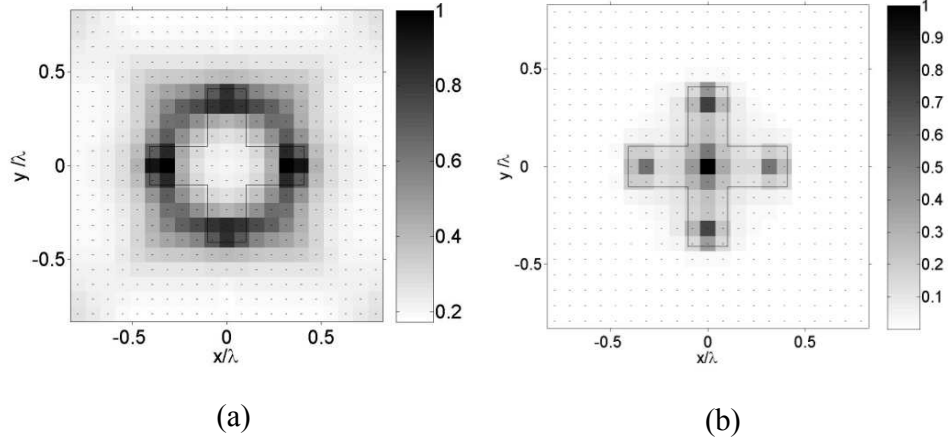


Fig. 5.5: Reconstruction of cross-like cylinder computed using (a) LSM and (b) MUSIC. “Noiseless” model.

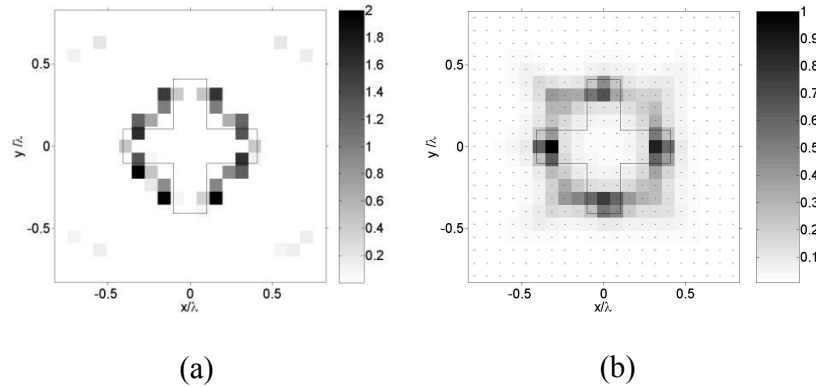
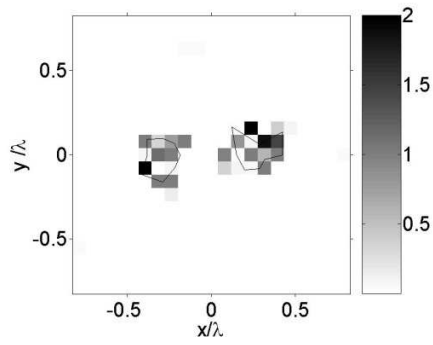


Fig. 5.6: Reconstruction of cross-like cylinder computed using (a) sparse signal processing and (b) MUSIC for  $SNR = 20$  dB.

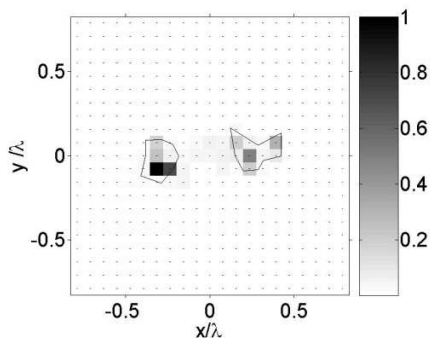
We further assumed that the observed data ( $\mathbf{j}_s - \mathbf{j}_{s_0}$ ) in the sparse processing, as well as the elements of the multistatic matrix  $\mathbf{F}$  in LSM or MUSIC, were corrupted by CAWGN. Fig. 5.6 shows the images computed for  $SNR = 20$  dB. The sparse processing proved robust with respect to the noise, whereas the performance of MUSIC was strongly

deteriorated.

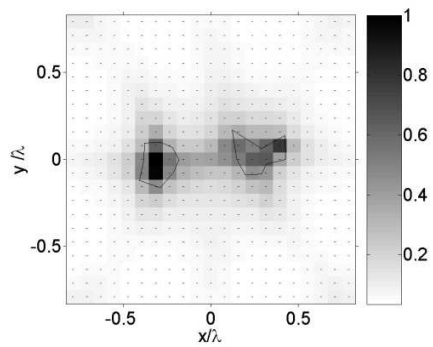
We considered two metallic targets in close proximity, denoted by the solid lines in Fig. 5.7. We show the results for the “noiseless” case in Fig. 5.7 and for  $SNR = 10$  dB in Fig. 5.8. If no noise is added, both MUSIC and sparse processing correctly estimated the number of the targets, whereas the number of the targets was ambiguous in the LSM image. The results were aggravated if the measurements were corrupted by CAWGN; yet the targets were well resolved if sparse processing or MUSIC is applied.



(a)

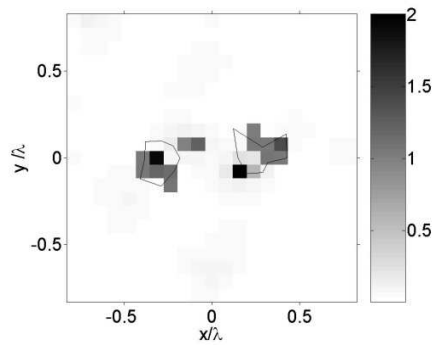


(b)

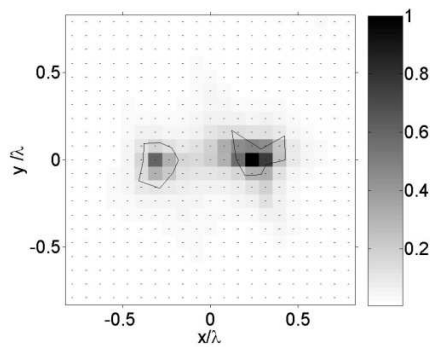


(c)

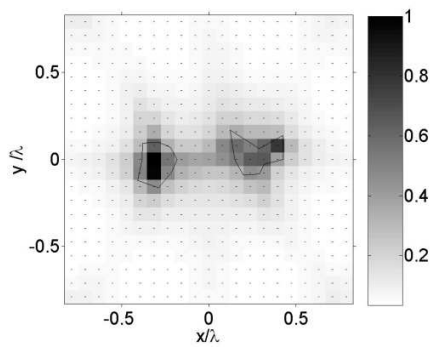
Fig.5.7: Reconstruction of two metallic targets computed using (a) sparse signal processing ( $\gamma^{(1)} = 1.4$ ,  $L = 21^2$ ,  $V = 1$ ), (b) MUSIC, and (c) LSM. “Noiseless” model.



(a)



(b)



(c)

Fig.5.8: Reconstruction of two metallic targets computed using (a) sparse signal processing ( $\gamma^{(1)} = 1.4$ ,  $L = 21^2$ ,  $V = 1$ ), (b) MUSIC, and (c) LSM for  $SNR = 10$  dB.

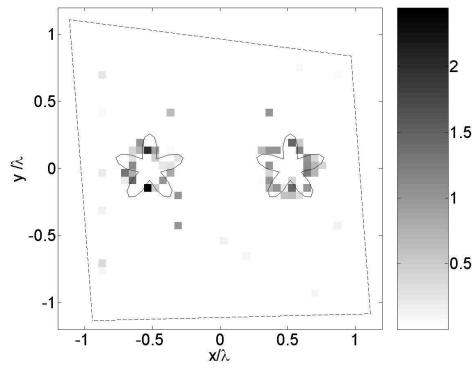
We also tested the algorithm against the irregularities of the dielectric body. Fig. 5.9 shows the shape of the dielectric and two targets. In this case, we used the array with  $M = 20$  sensors. The separation between the adjacent sensors was 20 cm. Because of small details in the shape of the targets, we increased the number of the equivalent sources ( $L = 32^2$ ).

Without grouping ( $V = 1$ ), the performance of the sparse algorithm was numerically instable. Consequently, the computation time increased considerably. The polynomial model for the currents of the equivalent sources stabilized the solution. We show in Fig. 5.9a the reconstruction obtained for ( $L = 32^2$ ,  $V = 4$ ).

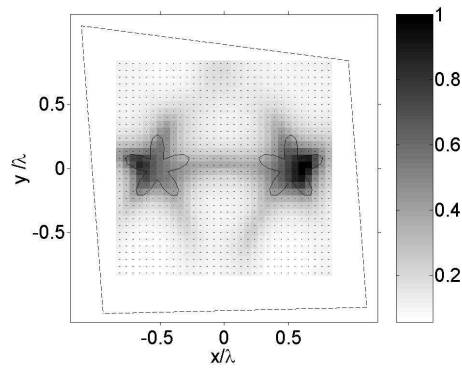
The reconstructions obtained using LSM and MUSIC are given in Fig. 5.9b and Fig. 5.9c respectively. Whereas sparse processing revealed parts of the targets' contours, the LSM and MUSIC gave insight into the targets' shape. However, when LSM was applied the edges of the targets were unclear.

In Tab. 1, we compared computational times of the algorithms. The results were similar. However, the computational speeds of LSM and MUSIC are dictated by the efficacy of the electromagnetic solver because the forward calculations are repeated for each point in the grid. In contrast, the computational speed of the sparse algorithm is influenced by the convex optimization which is solved for each sensor. However, the convex optimization may become slow if the number of the unknowns is too large.

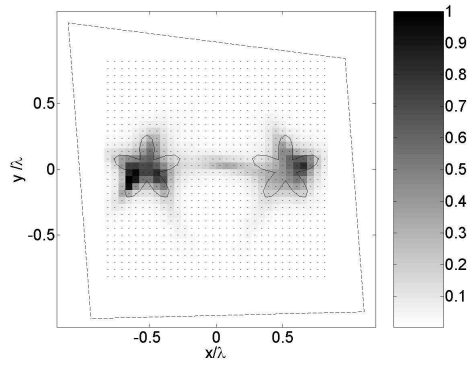




(a)



(b)



(c)

Fig.5.9: Reconstruction of two star-shaped cylinders computed using (a) single-step sparse processing ( $\gamma^{(1)} = 1.4, L = 32^2, V = 4$ ), (b) LSM, (c) and MUSIC for  $SNR = 20$  dB.

TABLE I  
COMPUTATIONAL TIMES OF INVERSE ALGORITHMS

Number of grid points ( $L$ )	Number of sensors ( $M$ )	LSM time [min]	MUSIC time [min]	SPARSE ( $V = 1$ ) time [min]	SPARSE ( $V = 4$ ) time [min]
$21^2 = 441$	16	28	28	21	20
$24^2 = 576$	16	36	36	60	25
$28^2 = 784$	16	52	52	70	40

## 5.4.2 Two-Step Estimation

We considered a metallic cylinder in the shape of a thick letter U. The target is denoted by the solid line in Fig. 5.10. The difficulties in LSM imaging of a dielectric cylinder of the same shape were observed in [58]. It was expected that these problems would become more severe in the case of a metallic cylinder because of the multiple scattering. In Fig. 5.10, we show the results obtained for  $SNR = 20$  dB,  $L = 21^2$ ,  $V = 1$ ,  $\gamma^{(1)} = 1.4$  and  $\gamma^{(1)} = 1.8$ . The estimated scattering centers were around the target surfaces; however some parts of the target's contour were not revealed. Next, we used the data obtained in the first-step estimation (Fig. 5.10b) as the feed for the second-step estimation. We applied the EFIE constraint to the equivalent sources found in the first step whose currents exceed the adopted threshold:  $\delta = 0.5 \max(\hat{\mathbf{j}}_t)$ . As shown in Fig. 5.11, the second-step estimation yielded much better results. We selected values for the regularization parameter ( $\gamma^{(2)} = 1.4, 1.6$ ) that were slightly less than the values of the

regularization parameter in the first step (inferred from the solution's  $l_0$ -norm). In Fig. 5.12, we show the computations performed for  $L = 21^2$ ,  $V = 1$  and  $L = 24^2$ ,  $V = 3$ , We set  $SNR = 10$  dB (anticipated as the minimal necessary SNR).

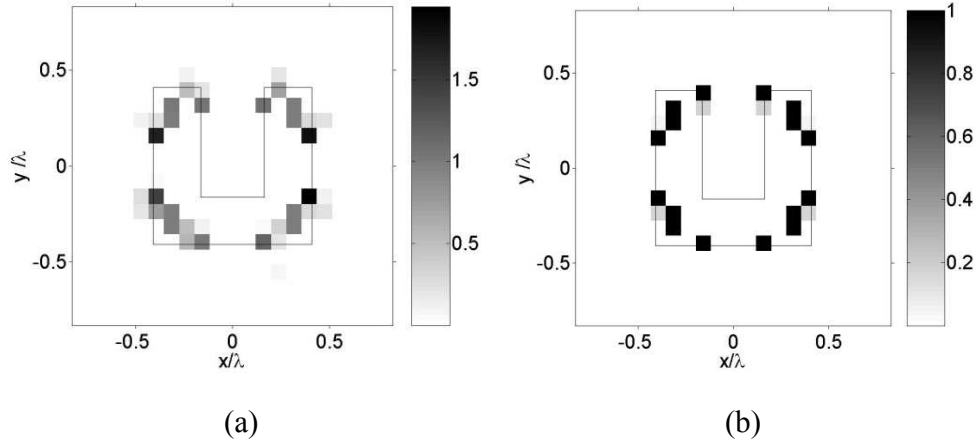


Fig. 5.10: Reconstruction of U-shaped target computed using single-step sparse processing for (a)  $\gamma^{(1)} = 1.4$ ,  $L = 21^2$ ,  $V = 1$  and (b)  $\gamma^{(1)} = 1.8$ ,  $L = 21^2$ ,  $V = 1$  ( $SNR = 20$  dB).

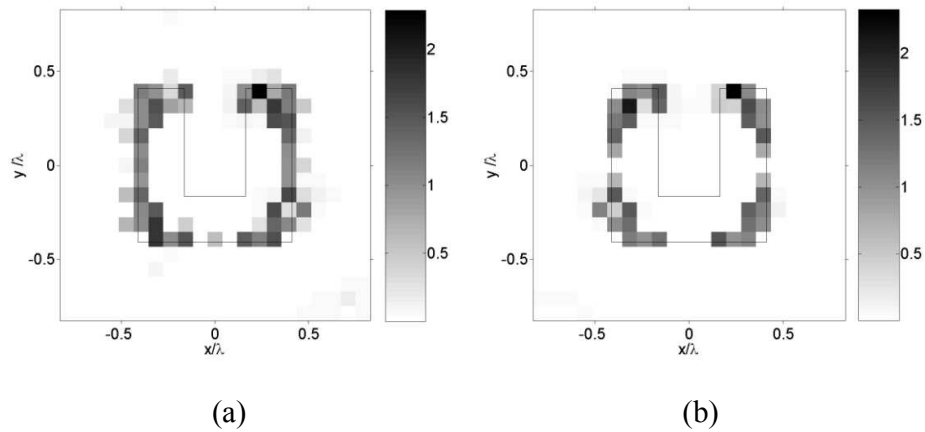


Fig. 5.11: Reconstruction of U-shaped target computed using two-step sparse processing for  $\gamma^{(1)} = 1.8$ ,  $L = 21^2$ ,  $V = 1$  and (a)  $\gamma^{(2)} = 1.4$  and (b)  $\gamma^{(2)} = 1.6$  ( $SNR = 20$  dB).

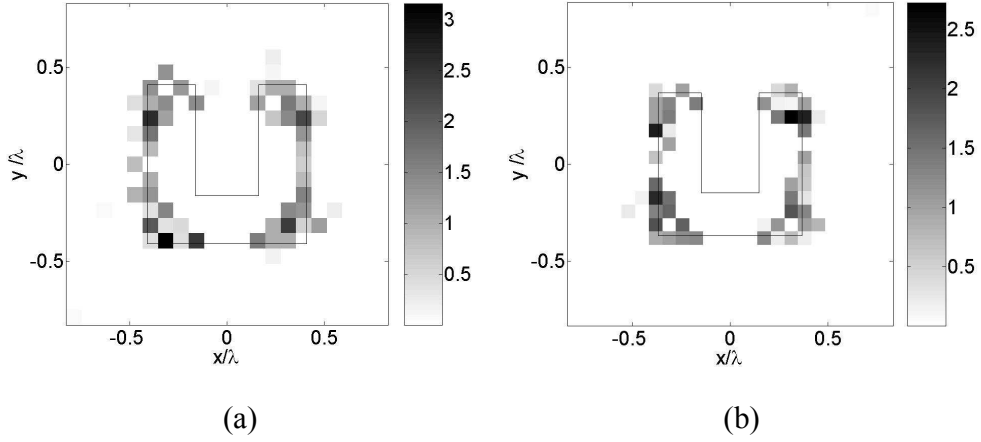


Fig. 5.12: Reconstruction of U-shaped target computed using two-step sparse processing for  $\gamma^{(1)} = 1.8$ ,  $\gamma^{(2)} = 1.4$  and (a)  $L = 21^2, V = 1$  and (b)  $L = 24^2, V = 3$  ( $SNR = 10$  dB).

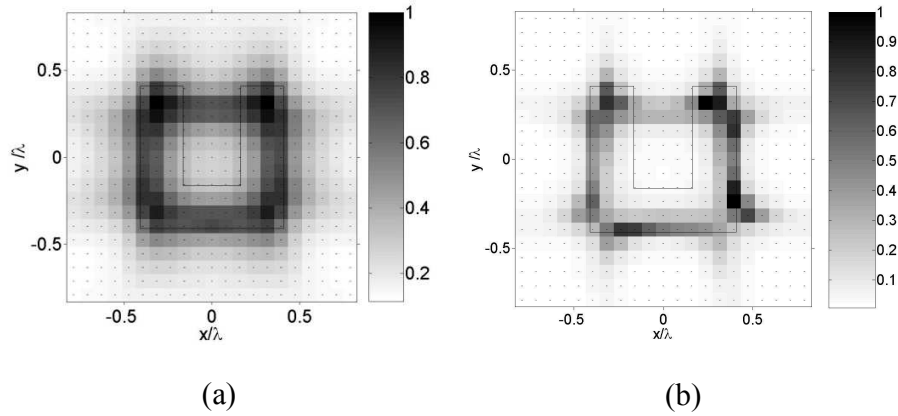
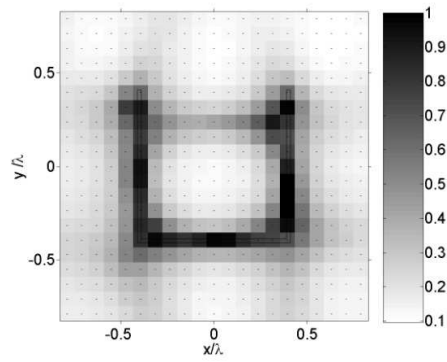


Fig. 5.13: Image of thick U-shaped cylinder computed using (a) LSM and (b) MUSIC ( $SNR = 20$  dB).

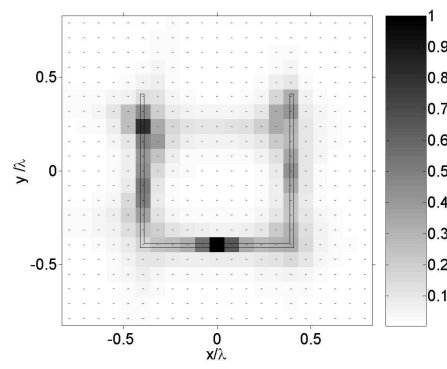
For comparison, we applied LSM and MUSIC. As depicted in Fig. 5.13a, LSM failed to recover the non-convex shape of the target. This is in accordance with [58] where the imaging of a dielectric cylinder of the same shape was studied. The performance of MUSIC was similar to that of LSM (Fig. 5.13b).

We also investigated the reconstruction of a thin U-shaped cylinder. The LSM

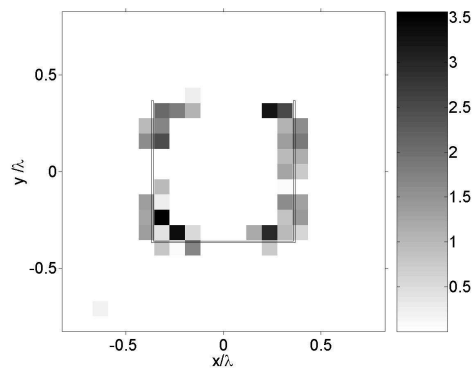
algorithm yielded an excellent estimate of the target (Fig. 5.14a), as also observed in [58]. The MUSIC estimate was also accurate, as shown in Fig. 5.14b. In Fig. 5.14c, we present the result of the two-step estimation ( $L = 24^2$ ,  $V = 3$ ). In this case, the images of the thin and thick U-shaped targets were very similar. Hence, the LSM predicts the thickness of the target, whereas the sparse processing assesses the target's contour. In Fig. 5.15, we illustrate the robustness against noise of the sparse algorithm ( $SNR = 10$  dB).



(a)

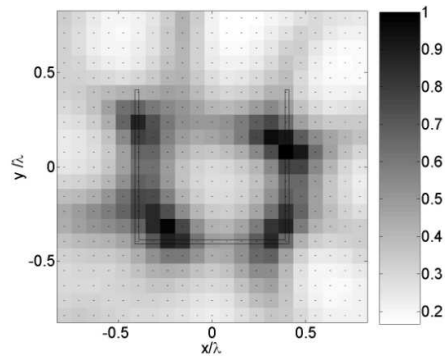


(b)

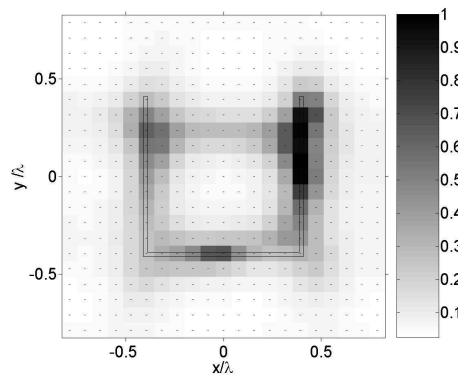


(c)

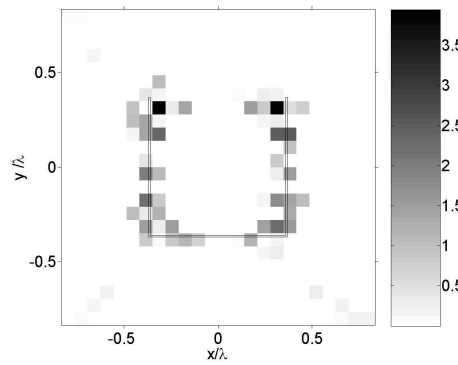
Fig. 5.14: Image of thin U-shaped cylinder computed using (a) LSM, (b) MUSIC, and (c) two-step sparse processing ( $L = 24^2, V = 3$ ) for SNR = 20 dB.



(a)

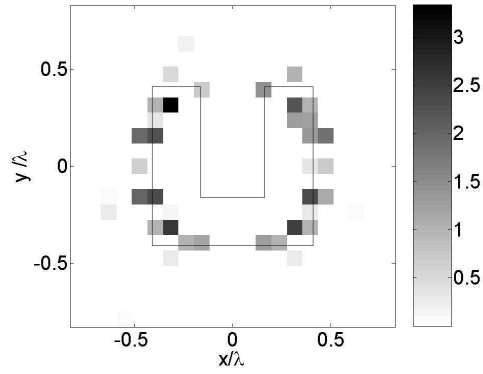


(b)

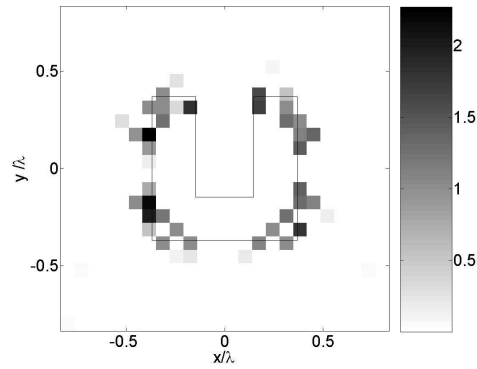


(c)

Fig. 5.15: Image of thin U-shaped cylinder computed using (a) LSM, (b) MUSIC, and (c) two-step sparse processing ( $L = 24^2, V = 3$ ) for SNR = 10 dB.



(a)



(b)

Fig. 5.16: Reconstruction of thick U-shaped cylinder computed using erroneous dielectric permittivity ( $\epsilon_r = 3.3 - 0.33j$ ) in the two-step sparse algorithm for  $\gamma^{(1)} = 1.8$ ,  $\gamma^{(2)} = 1.4$ ,  $SNR = 20$  dB, and (a)  $L = 21^2$ ,  $V = 1$  and (b)  $L = 24^2$ ,  $V = 3$ .

Finally, we studied the sensitivity of the algorithm to the errors in the permittivity of the background medium. In Fig. 5.16, we present the reconstructions obtained for  $\epsilon_r = 3.3(1 - 0.1j)$ , which was 10% larger than the true permittivity. The quality of the reconstruction was worse than that obtained using the real dielectric permittivity, however the target shape could be discerned.



## 5.5 Experiment

In this section, we discuss the experimental verification of the proposed imaging method. We first explain a 3D electromagnetic model that is equivalent to the considered 2D problem. We use this equivalent model to validate both the forward and inverse method, as we detail below.

### 5.5.1 Theoretical Model

We show in Fig. 5.17 an example of 2D electromagnetic system consisting of infinitely long conductors and dielectric bodies of arbitrary cross-section. We assume that the conductors are excited by an axial impressed electric field ( $E_i$ ) which is independent of the  $z$ -coordinate.

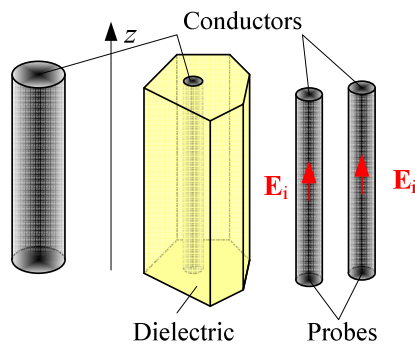


Fig. 5.17: An example of a 2D electromagnetic system.

As a response to the excitation, the axial currents are induced in the dielectric and conducting bodies. The currents are independent of the  $z$ -coordinate. We take a short horizontal section of the system of Fig. 5.17 and place it between two PEC

planes, as illustrated in Fig. 5.18. After multiple mirroring from PEC planes, the system in Fig. 5.18 becomes infinitely long.

We assume that the conductors in the 3D model are excited by voltage delta-generators. If the height of the system is electrically small, i.e.,  $h < 0.05\lambda_0$  ( $\lambda_0$  is the wavelength in the air), the induced currents are practically constant along the  $z$ -axis. Setting the electromotive force of the generators to  $V = E_i h$  provides that the currents in both systems are approximately the same. This yields a simple relationship between the admittance parameters ( $Y$ ) of the 3D system and the per-unit-length admittance parameters ( $\bar{Y}$ ) of the 2D system:  $\bar{Y} = Yh$ .

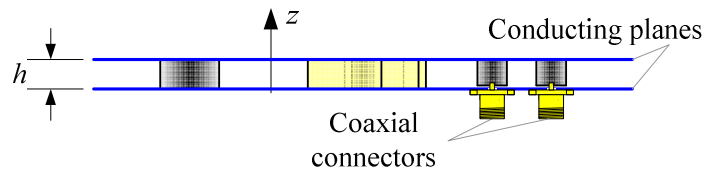


Fig. 5.18: The equivalent 3D model of the electromagnetic system of Fig. 5.17.

In the experiment, instead of PEC planes, we use finite metallic plates. In order to achieve good mirroring, it is necessary that the electric and magnetic fields are negligible at the edges of the plates. Otherwise, a substantial radiation from the edges occurs which does not exist in the 2D model. To avoid this unwanted radiation, the plates must be wavelengths large. An alternative is to close the vertical sides of both systems by metallic walls.

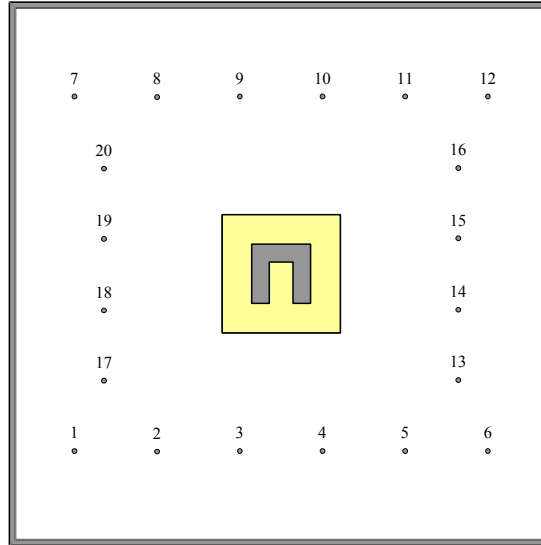


Fig. 5.19: The measurement setup.

In Fig. 5.19, we depict the 3D experimental model. The system was shielded by vertical aluminum walls, located along the sides of the square plates. The plates were also made of the aluminum with the side length 900 mm. The sensors were thin wires with the diameter  $D = 3$  mm. A dielectric cylinder with the immersed target was located in the center of the structure. The dielectric had a square cross-section with the side length 200 mm. The permittivity of the dielectric was  $\epsilon_r = 4,5$  and the loss tangent  $\tan \delta = 0.025$ . The target was the thick U-shaped cylinder, described in Section 5.4.2. The height of the system was  $h = 12$  mm. The operating frequency was about 1 GHz.

We used the forward model of Chapter 2 to compute the response of the corresponding 2D system. We calculated the admittance parameters of the 3D system by means of WIPL-D Pro software [118]. We measured the scattering parameters of the experimental model, and then obtained the admittance parameters using the relationship as given in

[119],

$$\mathbf{Y} = \sqrt{\mathbf{Y}_c} (\mathbf{I}_M - \mathbf{S}) (\mathbf{I}_M + \mathbf{S})^{-1} \sqrt{\mathbf{Y}_c}, \quad (5.48)$$

where  $\mathbf{S}$  is the measured scattering matrix,  $M$  is the number of the sensors,  $\mathbf{Y}_c$  is the diagonal matrix whose elements are the characteristic admittances of the ports, and  $\mathbf{I}_M$  is the identity matrix. In our case:  $M = 20$ ,  $\mathbf{Y}_c = (1/50\Omega)\mathbf{I}_M$ . We show in Fig. 5.20 the results for the admittance parameter  $\bar{Y}_{56}$  associated with the coupling between two adjacent sensors. The excellent agreement among the results validated the proposed measurement model. The results for other parameters were similar.

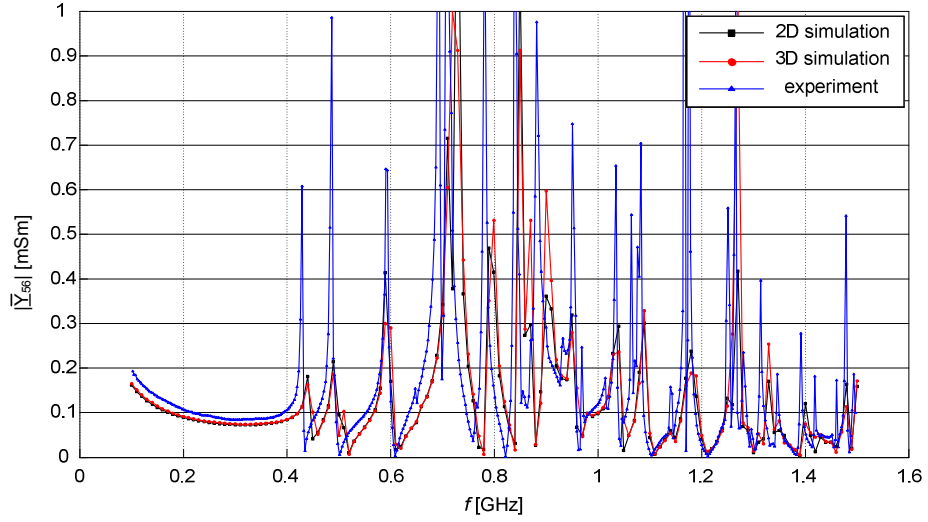


Fig. 5.20: Admittance parameter  $\bar{Y}_{56}$  obtained by 2D simulation, 3D simulation, and measurements.

## 5.5.2 Inverse Method

In the experimental model, the induced electric currents appear on the inner surfaces of

the metallic walls. We include those currents in the measurement model (5.8)-(5.11)

$$\mathbf{y} = \mathbf{G}_2 \mathbf{x} + \mathbf{w}, \quad (5.49)$$

where now

$$\mathbf{y} = -\mathbf{G}_s (\mathbf{j}_s - \mathbf{j}_{s0}), \quad (5.50)$$

$$\mathbf{x} = \left[ (\Delta \mathbf{j}_d)^T \quad (\Delta \mathbf{m}_d)^T \quad (\Delta \mathbf{j}_w)^T \quad (\Delta \mathbf{j}_t)^T \right]^T, \quad (5.51)$$

$$\Delta \mathbf{j}_w = \mathbf{j}_w - \mathbf{j}_{w0}. \quad (5.52)$$

Here,  $\mathbf{j}_w \in C^J$  is the unknown vector of the electric current densities on the metallic walls when the equivalent sources are in the dielectric,  $\mathbf{j}_{w0} \in C^J$  is the unknown vector of the electric current densities on the metallic walls with the equivalent sources being removed from the dielectric, and  $J$  is the number of the unknown current coefficients on the metallic walls. The matrices  $\mathbf{G}_s \in C^{(K+J) \times M}$  and  $\mathbf{G}_2 \in C^{(K+J) \times (2P+J+L)}$  are expanded to account for the currents and matching points on the walls.

Again, we use polynomial expansion to model the induced electric currents on the walls,

$$\Delta J_w(s) \approx \sum_{i=0}^I \tau_i s^i, \quad 0 \leq s \leq 1, \quad (5.53)$$

where  $\Delta J_w(s)$  is the difference in the electric current density due to the presence of the targets,  $\tau_i$  is the  $i$ th coefficient of the approximation,  $i = 0, \dots, I$ , and  $s$  is the length

coordinate along the contour of the walls. (Depending on the electrical size of the walls, it may be necessary to divide the wall contour into smaller segments.) The elements of the vector  $\Delta \mathbf{j}_w$  are samples of the polynomial (5.53) at the matching points. We relate the unknown current densities with the polynomial coefficients as

$$\Delta \mathbf{j}_w = \mathbf{H}_w \boldsymbol{\tau}, \quad (5.54)$$

with

$$\mathbf{H}_w = [\mathbf{s}_1 \quad \dots \quad \mathbf{s}_J]_{J \times (l+1)}^T, \quad (5.55)$$

$$\mathbf{s}_j = [s_j^0 \quad \dots \quad s_j^l]^T, \quad s_j = (j - 0.5)/J, \quad j = 1, \dots, J, \quad (5.56)$$

$$\boldsymbol{\tau} = [\tau_0 \quad \dots \quad \tau_l]^T. \quad (5.57)$$

Here,  $\boldsymbol{\tau}$  is the vector of the polynomial coefficients,  $\mathbf{H}_w$  is the transformation matrix, and  $s_j$  is the length coordinate of the  $j$ th matching point. The final measurement model reads

$$\mathbf{y} = \mathbf{G}_2 \boldsymbol{\Psi} \mathbf{z} + \mathbf{w}, \quad \mathbf{x} = \boldsymbol{\Psi} \mathbf{z}, \quad (5.58)$$

$$\mathbf{z} = [\boldsymbol{\alpha}^T \quad \boldsymbol{\beta}^T \quad \boldsymbol{\tau}^T \quad \boldsymbol{\sigma}^T]^T, \quad \boldsymbol{\Psi} = \begin{bmatrix} \mathbf{H}_d & \mathbf{0} & \mathbf{0} & \mathbf{0} \\ \mathbf{0} & \mathbf{H}_d & \mathbf{0} & \mathbf{0} \\ \mathbf{0} & \mathbf{0} & \mathbf{H}_w & \mathbf{0} \\ \mathbf{0} & \mathbf{0} & \mathbf{0} & \mathbf{H}_t \end{bmatrix}, \quad (5.59)$$

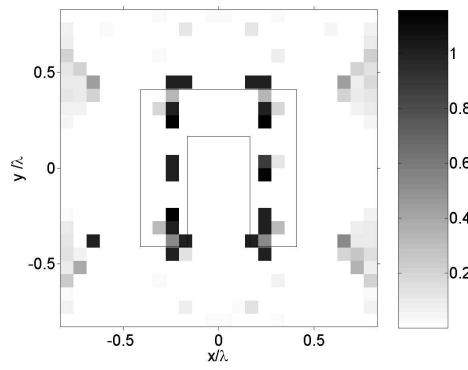
where  $\mathbf{z}$  is the new unknown parameter vector and  $\boldsymbol{\Psi}$  is the transformation matrix. The

model (5.59) is further substituted into the one-step (5.28) and two-step cost functions (5.39).

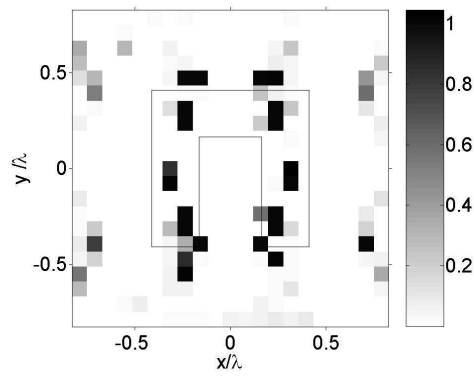
We obtained the vector of the current densities on the sensors ( $\mathbf{j}_s$ ) from the admittance parameters which are related to the measured scattering parameters by (5.48). When  $i$ th the sensor was excited, we computed the  $j$ th element of the vector  $\mathbf{j}_s$  as

$$j_s(j; i) = \mathbf{Y}(i, j) \frac{h}{\pi D}.$$

Fig. 5.21a shows the single-step reconstruction computed using the synthetic data and Fig. 5.21b shows the reconstruction computed using the measurements. The agreement was excellent. The operating frequency was  $f = 1.2$  GHz and the algorithm parameters were  $\gamma^{(1)} = 1.4$ ,  $V = 3$ ,  $L = 21^2$ . We also present in Fig. 5.22 the results obtained at  $f = 1.1$  GHz. The agreement was also good; however the target image was somewhat ambiguous in this case. Because of the multiple scattering from the metallic enclosure, the induced currents on the targets varied significantly with the frequency. Hence, the images Fig. 5.21 and Fig. 5.22 recovered different parts of the target's contour.



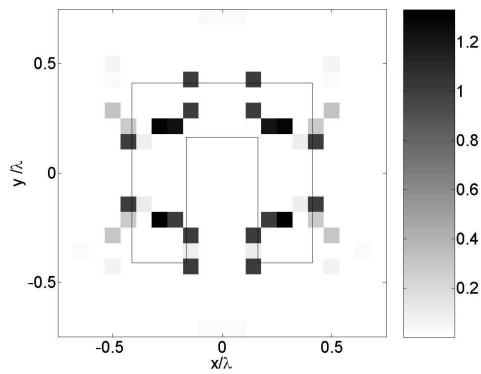
(a)



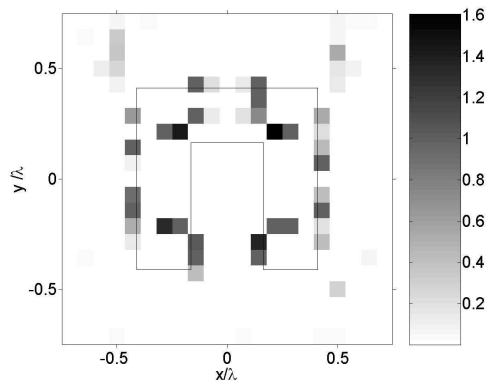
(b)

Fig. 5.21: Reconstruction of the U-shape target using the system of Fig. 20. Results are obtained using (a) synthetic data and (b) measured data at  $f = 1.2$  GHz for  $\gamma^{(1)} = 1.4$ .





(a)



(b)

Fig. 5.22: Reconstruction of the U-shape target using the system of Fig. 20. Results are obtained using (a) synthetic data and (b) measured data at  $f = 1.1$  GHz for  $\gamma^{(1)} = 1.4$ .

We did not observe the significant improvement due to another iteration (neither in numerical nor in experimental reconstructions) as we did in the system without the metallic enclosure (Fig. 5.11). The reason for this may be the fact that the currents are not truly sparse in the presence of the enclosure.

## 5.6 Summary

We proposed a method for estimating obscured 2D PEC targets based on the equivalent-source method and  $l_1$  regularization. We used the surface equivalence theorem to derive a linear measurement model with respect to the unknown equivalent sources. The application of the sparsity constraint emphasized the equivalent sources located on the scatterer surfaces (in particular, the scattering centers). Exploiting the information content of a multiview/multistatic configuration, the method reliably reconstructed the target shapes using monochromatic scattered data. We considered both single-step and two-step versions of the method. We tested the performance of the algorithm on the examples of non-convex targets with pronounced wedges and on closely spaced targets. The performance of the method was compared to that of LSM and MUSIC. The examinations showed that sparse processing was able to recover the target shapes in cases for which both MUSIC and LSM failed, typically bulky non-convex targets. Nevertheless, LSM and MUSIC inferred about the target's interior, whereas the sparse imaging recovered only the target contour. Hence, sparse imaging and LSM (MUSIC) provided the complimentary pieces of data. We examined the accuracy of the proposed inverse method experimentally. We designed the 3D model that is equivalent to the 2D problem using the mirroring theory. The obtained experimental results were in agreement with the numerical experiments. However, in the experimental model, the system under investigation was inside the metallic box. The multiple scattering from the box significantly influenced the target reconstruction. Unlike in the case without the box, the target images significantly varied with the frequency. Hence, the target images obtained

at different frequencies provided the complimentary pieces of information. However, because of the multipath, the currents on the target surfaces were not entirely sparse. The reflections from the metallic walls enlarged the illuminated portion of the target surface, and therefore the induced currents became significant almost everywhere on the target's surface. In order to take advantage of both the multipath and sparse processing, it is necessary to find the basis functions in which the currents on the targets are sparser.

## Chapter 6

# Estimating Direction of Arrival Using Multipath from Array Platforms

### 6.1 Introduction

Electromagnetic scattering from environment poses difficulties in target estimation, but also provides additional information about the targets. Sensor arrays are often mounted on platforms, which are significant sources of scattering (multipath). In this Chapter, we study the exploitation of the multipath information *from sensing systems* in the direction of arrival estimation (DOA) [120]. This is in contrast to recent investigations in which the multipath *from the target's surroundings* is utilized for improving the localization characteristics of sensing arrays [74]-[79].

We consider an example of a realistic airborne platform, the Unmanned Aerial Vehicle (UAV) Predator. Because of the low profile of the Predator, diffraction is the main source of the multipath. We show that employing the multipath allows estimating both the azimuth and elevation of multiple unknown incident signals, even at a single frequency, which would otherwise be impossible with uniform linear arrays. Interestingly, human and similar auditory systems use the diffraction of sound waves to enable

three-dimensional (3D) direction finding [121].

We use the Cramer-Rao bound (CRB) to study the performance improvement due to the multipath. We verify the proposed approach experimentally, by considering the DOA estimation using a linear array mounted on a plate. To provide physical insight on the influence of the multipath on the effective array aperture, we show that the performance of arrays on platforms is similar to that of arrays with parasitic elements [122]-[126].

## 6.2 Measurement Model

We assume that  $K$  plane-wave signals impinge on a sensor array mounted on a platform.

The output of the array element located at  $\mathbf{r}$  is given in [127] as

$$x(\mathbf{r}, f) = \sum_{k=1}^K s_k(f) \cdot \mathbf{l}(\mathbf{r}, f, \theta_k, \phi_k) \exp(-j\beta \mathbf{r} \cdot \mathbf{r}_{0k}) + e(\mathbf{r}, f), \quad (6.1)$$

$$\mathbf{l} = l_\theta \mathbf{i}_\theta + l_\phi \mathbf{i}_\phi, \quad (6.2)$$

$$\mathbf{s}_k = s_{k,\theta} \mathbf{i}_\theta + s_{k,\phi} \mathbf{i}_\phi, \quad (6.3)$$

and

$$\mathbf{r}_{0k} = [\sin\theta_k \cos\phi_k \quad \sin\theta_k \sin\phi_k \quad \cos\theta_k]^\top, \quad (6.4)$$

where  $\mathbf{l}$  is the effective length of the sensor that encompasses mutual coupling, reflections, and diffractions on the platform;  $\theta_k$  is the elevation of the  $k$ th signal;  $\phi_k$  is the

azimuth of the  $k$ th signal;  $s_{k,\theta}$  and  $s_{k,\phi}$  are the complex magnitudes of the signal at the operating frequency that are associated with the  $\theta$  and  $\phi$  components of the incident electric field, respectively;  $\mathbf{r}_{0k}$  is the unit vector in the direction of propagation of the  $k$ th signal; and the operator T stands for transpose. Finally,  $\beta$  is the propagation coefficient,  $f$  is the operating frequency, and  $e$  is the complex additive white Gaussian noise (CAWGN) of unknown variance  $\sigma^2$ .

We consider linearly polarized arrays. Without loss of generality, we assume that  $\theta$  is the co-polar component of the array response and  $\phi$  is the cross-polar component. The locations of the sensors in the array are given by  $\mathbf{r}_m$ ,  $m = 1, \dots, M$ . The induced voltage in the  $m$ th sensor is

$$x(\mathbf{r}_m, f_n) = \sum_{k=1}^K s_{k,\theta}(f_n) h_{\theta}(\mathbf{r}_m, f_n, \theta_k, \phi_k) + \sum_{k=1}^K s_{k,\phi}(f_n) h_{\phi}(\mathbf{r}_m, f_n, \theta_k, \phi_k) + e(\mathbf{r}_m, f_n), \quad (6.5)$$

and

$$h_p(\mathbf{r}_m, f_n, \theta_k, \phi_k) = l_p(\mathbf{r}_m, f_n, \theta_k, \phi_k) \exp(-j\beta \mathbf{r}_m \cdot \mathbf{r}_{0k}), \quad (6.6)$$

$$m = 1, \dots, M, \quad n = 1, \dots, N,$$

where  $f_n$  is the  $n$ th frequency and the subscript  $p$  in (6.6) stands for either  $\theta$  or  $\phi$ . We put the array output in compact form:

$$\mathbf{x} = \mathbf{H}\mathbf{s} + \mathbf{e}, \quad (6.7)$$

$$\mathbf{x} = [\mathbf{x}_1^T \quad \mathbf{x}_2^T \quad \dots \quad \mathbf{x}_N^T]_{NM \times 1}^T, \quad (6.8)$$

$$\mathbf{x}_n = [x(\mathbf{r}_1, f_n) \quad x(\mathbf{r}_2, f_n) \quad \dots \quad x(\mathbf{r}_M, f_n)]_{M \times 1}^T, \quad n = 1, \dots, N, \quad (6.9)$$

where  $\mathbf{x}$  is the stacked measurement vector. Further,

$$\mathbf{H} = [\mathbf{H}_\theta \quad \mathbf{H}_\phi]_{NM \times 2K}, \quad (6.10)$$

and

$$\mathbf{H}_p = \text{blkdiag}(\mathbf{H}_{1,p}, \mathbf{H}_{2,p}, \dots, \mathbf{H}_{N,p})_{NM \times K}, \quad (6.11)$$

where  $\mathbf{H}$  is the measurement matrix;  $\mathbf{H}_\theta$  and  $\mathbf{H}_\phi$  are the submatrices associated with the co-polar and cross-polar array response, respectively; blkdiag denotes the block-diagonal matrix; and  $p$  denotes either  $\theta$  or  $\phi$ .  $\mathbf{H}_\theta$  and  $\mathbf{H}_\phi$  are the block-diagonal matrices where each non-zero block is

$$\mathbf{H}_{n,p} = [\mathbf{h}_p(f_n, \theta_1, \phi_1) \quad \mathbf{h}_p(f_n, \theta_2, \phi_2) \quad \dots \quad \mathbf{h}_p(f_n, \theta_K, \phi_K)]_{M \times K}, \quad (6.12)$$

and

$$\mathbf{h}_p(f, \theta, \phi) = [h_p(\mathbf{r}_1, f, \theta, \phi) \quad h_p(\mathbf{r}_2, f, \theta, \phi) \quad \dots \quad h_p(\mathbf{r}_M, f, \theta, \phi)]_{M \times 1}^T. \quad (6.13)$$

The samples of the complex magnitudes in the frequency domain are stacked in vector  $\mathbf{s}$ , defined by

$$\mathbf{s} = \begin{bmatrix} \mathbf{s}_\theta^\top & \mathbf{s}_\phi^\top \end{bmatrix}_{2NK \times 1}^\top, \quad (6.14)$$

$$\mathbf{s}_p = \begin{bmatrix} \mathbf{s}_{1,p}^\top & \mathbf{s}_{2,p}^\top & \dots & \mathbf{s}_{N,p}^\top \end{bmatrix}_{NK \times 1}^\top, \quad (6.15)$$

$$\mathbf{s}_{n,p} = \begin{bmatrix} s_{1,p}(f_n) & s_{2,p}(f_n) & \dots & s_{K,p}(f_n) \end{bmatrix}_{K \times 1}^\top, \quad (6.16)$$

$$\mathbf{e} = \begin{bmatrix} \mathbf{e}_1^\top & \mathbf{e}_2^\top & \dots & \mathbf{e}_N^\top \end{bmatrix}_{NM \times 1}^\top, \quad (6.17)$$

and

$$\mathbf{e}_n = \begin{bmatrix} e(\mathbf{r}_1, f_n) & e(\mathbf{r}_2, f_n) & \dots & e(\mathbf{r}_M, f_n) \end{bmatrix}_{M \times 1}^\top. \quad (6.18)$$

The goal of the estimation is to compute the unknown angles  $\boldsymbol{\varphi} = [\phi_1, \dots, \phi_K]^\top$  and  $\boldsymbol{\theta} = [\theta_1, \dots, \theta_K]^\top$ . The signal coefficients ( $\mathbf{s}$ ) and the noise variance  $\sigma^2$  are also unknown, but they are considered to be nuisance parameters. The array response ( $\mathbf{H}$ ) depends only on the electromagnetic characteristics of the array and the platform; hence it is known. Finally, we consider the cases when the number of incident waves ( $K$ ) is known and when it is unknown.

### 6.3 Electromagnetic Model

Herein we consider a realistic airborne platform (Predator), shown in Fig. 6.1. The Predator is a medium-altitude, unmanned aerial vehicle system. The airplane is 8.1 m long with a 14.8 m wingspan. We assume that a uniform linear array of monopoles is



mounted on the Predator. The position of the array and the adopted coordinate system are depicted in Fig. 6.1. We study the passive case; i.e., all antennas in the array work as receivers. The antennas receive both direct signals and signals diffracted from the UAV chassis. Due to the non-dihedral shape of the platform, the signals reflected from the platform do not reach the antennas. The main sources of diffraction are the wings, tail, and wedges at the bottom of the aircraft. For comparison, we also consider the scenario without the multipath. These data are obtained when the arrays are placed on an infinite plane made of a perfect electric conductor (PEC).

The array takes the measurements in the frequency domain. We compute the electromagnetic response of the array on the UAV [128] using the full-wave electromagnetic solver WIPL-D Pro [118]. We assume that the Predator is perfectly conducting. We adopt the central frequency of the computations to be  $f = 1$  GHz. The height of the monopoles is 80 mm, the radius of the monopoles is 1.2 mm, and the distance between adjacent monopoles is 0.15 m.

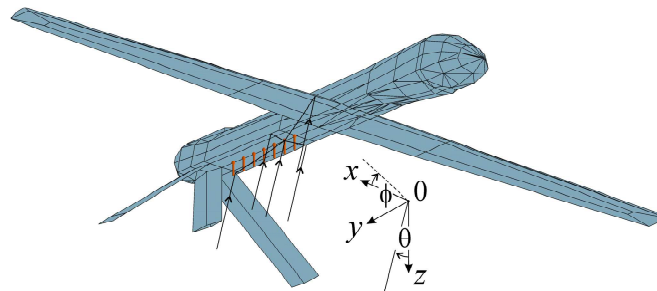


Fig 6.1: Geometrical model of the Predator with the adopted coordinate system. We show the uniform linear array of monopoles mounted on the bottom of the UAV and the multipath due to the diffraction (black arrows).

In general, the responses of the arrays should be modified to include the Doppler effect.

However, the maximal speed of the UAV Predator is about 60 m/s, yielding a Doppler shift of 0.2 kHz at 1 GHz, which is insignificant in the considered frequency range.

## 6.4 Cramer-Rao Bound

We compute the Cramer-Rao bound (CRB) on the variances of the spherical angles of the incident signals to demonstrate the estimation improvement due to the multipath. The covariance matrix of any unknown parameter vector is lower-bounded by the CRB, and it is attainable by statistically efficient unbiased estimators. For large data records, maximum likelihood (ML) asymptotically achieves the CRB. The CRB is obtained from the Fisher information matrix, which for a measurement model (6.7) reads as follows [129]:

$$[\mathbf{I}(\boldsymbol{\xi})]_{ij} = \text{tr} \left[ \mathbf{C}^{-1}(\boldsymbol{\xi}) \frac{\partial \mathbf{C}(\boldsymbol{\xi})}{\partial \xi_i} \mathbf{C}^{-1}(\boldsymbol{\xi}) \frac{\partial \mathbf{C}(\boldsymbol{\xi})}{\partial \xi_j} \right] + 2 \text{Re} \left\{ \frac{\partial (\mathbf{H}(\boldsymbol{\xi}) \mathbf{s}(\boldsymbol{\xi}))^H}{\partial \xi_i} \mathbf{C}^{-1}(\boldsymbol{\xi}) \frac{\partial (\mathbf{H}(\boldsymbol{\xi}) \mathbf{s}(\boldsymbol{\xi}))}{\partial \xi_j} \right\},$$

$$i, j = 1, \dots, \dim(\boldsymbol{\xi}), \quad \boldsymbol{\xi} = [\boldsymbol{\theta}^T \boldsymbol{\varphi}^T \mathbf{s}_r^T \mathbf{s}_i^T \sigma^2]^T, \quad (6.19)$$

where  $\mathbf{I}$  is the Fisher information matrix,  $\mathbf{C}$  is the covariance matrix of a Gaussian noise,  $\boldsymbol{\xi}$  is the vector of unknown parameters,  $\mathbf{s}_r$  is the real part of  $\mathbf{s}$ ,  $\mathbf{s}_i$  is the imaginary part of  $\mathbf{s}$ ,  $\text{tr}$  denotes the trace operator, the superscript H denotes the conjugate transpose,  $\text{Re}$  denotes the real part, and  $\dim$  denotes the dimension of a vector. The considered noise covariance matrix is  $\mathbf{C} = \sigma^2 \mathbf{I}_{MN}$ , where  $\mathbf{I}_{MN}$  is the identity matrix of size  $MN$ . We

assume that the noise is independent of the signal; hence the Fisher information matrix is given by

$$\mathbf{I}(\xi) = \begin{bmatrix} A(\boldsymbol{\eta}) & 0 \\ 0 & B \end{bmatrix}, \quad (6.20)$$

and

$$[A(\boldsymbol{\eta})]_{ij} = \frac{2 \operatorname{Re}}{\sigma^2} \left\{ \frac{\partial(\mathbf{H}(\boldsymbol{\eta})\mathbf{s}(\boldsymbol{\eta}))^H}{\partial \eta_i} \frac{\partial(\mathbf{H}(\boldsymbol{\eta})\mathbf{s}(\boldsymbol{\eta}))}{\partial \eta_j} \right\}, \quad B = \frac{\sigma^2}{MN},$$

$$i, j = 1, \dots, \dim(\boldsymbol{\eta}), \quad \boldsymbol{\eta} = [\boldsymbol{\theta}^T \boldsymbol{\varphi}^T \mathbf{s}_r^T \mathbf{s}_i^T]^T, \quad (6.21)$$

where  $\boldsymbol{\eta}$  is the vector of unknown parameters apart from  $\sigma^2$ . The CRB matrix is the inverse of the Fisher information matrix

$$\mathbf{CRB} = \mathbf{I}^{-1}. \quad (6.22)$$

The elements on the main diagonal of the CRB matrix contain the theoretical, lower bound on the parameter variances. Due to the block diagonal nature of the Fisher matrix (6.20), the CRB for the parameter vector  $\boldsymbol{\eta}$  is the same when  $\sigma^2$  is known and when it is unknown.

The derivatives with respect to azimuth and elevation of the  $k$ th wave are computed as

$$\begin{aligned} \frac{\partial(\mathbf{H}\mathbf{s})}{\partial p_k} &= \text{diag}\left[\frac{\partial h_\theta(f_1, \theta_k, \phi_k)}{\partial p_k}, \dots, \frac{\partial h_\theta(f_N, \theta_k, \phi_k)}{\partial p_k}\right] \tilde{\mathbf{s}}_{k,\theta} \\ &+ \text{diag}\left[\frac{\partial h_\phi(f_1, \theta_k, \phi_k)}{\partial p_k}, \dots, \frac{\partial h_\phi(f_N, \theta_k, \phi_k)}{\partial p_k}\right] \tilde{\mathbf{s}}_{k,\phi}, \end{aligned} \quad (6.23)$$

$$\frac{\partial h_q(f, \theta_k, \phi_k)}{\partial p_k} = \left[ \frac{\partial h_q(\mathbf{r}_1, f, \theta_k, \phi_k)}{\partial p_k} \quad \dots \quad \frac{\partial h_q(\mathbf{r}_M, f, \theta_k, \phi_k)}{\partial p_k} \right]^T, \quad (6.24)$$

$$\frac{\partial h_q(\mathbf{r}, f, \theta_k, \phi_k)}{\partial p_k} = \exp(-j\beta \mathbf{r} \cdot \mathbf{r}_{0k}) \left( \frac{\partial l_q(\mathbf{r}, f, \theta_k, \phi_k)}{\partial p_k} - l_q(\mathbf{r}, f, \theta_k, \phi_k) \frac{\partial(j\beta \mathbf{r} \cdot \mathbf{r}_{0k})}{\partial p_k} \right), \quad (6.25)$$

where both  $p$  and  $q$  stand for either  $\theta$  or  $\phi$ , and

$$\tilde{\mathbf{s}}_{k,q} = [s_{k,q}(f_1) \quad \dots \quad s_{k,q}(f_N)]^T \quad (6.26)$$

is the vector containing the complex magnitudes of the co-polar or cross-polar component of the  $k$ th signal at the frequencies  $f_1, \dots, f_N$ . Finally,

$$\frac{\partial(\mathbf{H}\mathbf{s})}{\partial \mathbf{s}_t} = -j \frac{\partial(\mathbf{H}\mathbf{s})}{\partial \mathbf{s}_i} = \mathbf{H}. \quad (6.27)$$

Since there are no closed-form expressions for the derivatives in (6.25), we resort to numerical differentiation. To obtain numerically stable results, we first use polynomials to approximate the expressions for the effective length with respect to the azimuth and elevation [130]. Then, we compute analytical derivatives of the polynomial approximation.

## 6.5 DOA Estimation

We estimate the unknown parameters using the ML approach [93] when the number of waves is *a priori* known. Otherwise, we use the minimum description length (MDL) [94].

We also consider another application of the MDL for model-selection. In Fig. 6.2, we show the ratio of the co-polar and cross-polar components of the radiated electric field at 1 GHz for one of the sensors in the array on the platform. For many incident angles, the cross polarization is negligible (below 10 dB). However, there are also directions of arrival for which the cross-polar and co-polar components of the array response are comparable. Including the cross-polarized component of the received signal in the measurement model, in the case when it is actually insignificant, may cause erroneous estimation due to “over-fitting” the data. Similarly, ignoring the cross-polarization in cases when it is truly pronounced will also deteriorate the estimation [131]. Hence, we need a tool to decide whether to include the cross-polarization in the model. The decision, made for each incident signal, depends on the signal polarization and the DOA.

It is well known that ML is not suitable for model selection problems. ML gives favor to more complex models, which may lead to overfitting. In contrast, from a set of candidate models, MDL selects a model that balances the data fidelity and compactness of the representation.

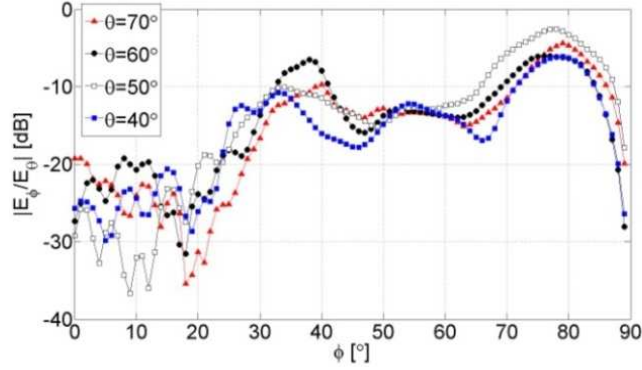


Fig. 6.2: Ratio of cross-polar and co-polar components of the radiation pattern of a sensor mounted on the UAV, computed using WIPL-D Pro at 1 GHz.

The cross-polar components of the array response are contained in the columns of the submatrix  $H_\phi$  (6.10). Each column of  $H_\phi$  corresponds to a different incident wave. We decide for each impinging wave whether to take into account the cross-polarization. If the maximal number of incident waves is  $K$ , and we assume that there is at least one incident wave, the total number of possible hypotheses is  $k_{\max} = \sum_{k=1}^K 2^k = 2^{K+1} - 2$ . We select one of the  $k_{\max}$  hypotheses for which the MDL criterion is minimal [94]:

$$MDL_\gamma = \frac{MN}{2} \log \|\mathbf{x} - \mathbf{H}_\gamma \hat{\mathbf{s}}_\gamma\|^2 + \frac{\dim(\mathbf{s}_\gamma)}{2} \log(MN), \quad \gamma = 1, 2, \dots, k_{\max}, \quad (6.28)$$

where  $MDL_\gamma$  is the MDL criterion for hypothesis  $\gamma$ ,  $\|\cdot\|^2$  denotes the Euclidian norm,  $\mathbf{H}_\gamma$  is the measurement matrix of hypothesis  $\gamma$ ,  $\mathbf{s}_\gamma$  is the vector of unknown complex coefficients, and  $\hat{\mathbf{s}}_\gamma$  is ML estimate of  $\mathbf{s}_\gamma$ .  $\mathbf{H}_\gamma$  is obtained from  $\mathbf{H}$  by eliminating the columns corresponding to the cross-polar responses of the waves for which we neglect the cross-polarization in this hypothesis. The second term in (6.28) penalizes long

representations of data, i.e., the inclusion of a large number of incident waves or addition of cross-polarization in the model.

We assume that the additive noise is spatially white and that the noise power is equal in each frequency bin. The ML solution for the complex amplitudes is

$$\hat{\mathbf{s}}_\gamma = \left( \mathbf{H}_\gamma^H \mathbf{H}_\gamma \right)^{-1} \mathbf{H}_\gamma^H \mathbf{x}. \quad (6.29)$$

We perform a simplex optimization [97] to compute the angle estimates from the concentrated likelihood:

$$\hat{\boldsymbol{\theta}}_\gamma, \hat{\boldsymbol{\phi}}_\gamma = \arg \min_{\boldsymbol{\theta}_\gamma, \boldsymbol{\phi}_\gamma} \left\| \mathbf{x} - \mathbf{H}_\gamma(\boldsymbol{\theta}, \boldsymbol{\phi}) \hat{\mathbf{s}}_\gamma \right\|^2, \quad (6.30)$$

where  $\hat{\boldsymbol{\theta}}_\gamma$  and  $\hat{\boldsymbol{\phi}}_\gamma$  are the estimated azimuth and elevation angles associated with model  $\gamma$ .

### 6.5.1 Single Source

We first assume there is only one incident wave impinging on the array. We study the angular error ( $\delta$ ) between the unknown source direction  $\mathbf{r}_0$  and its estimate  $\hat{\mathbf{r}}_0$ . For small angular errors,  $\delta$  is given by

$$\delta^2 = (\sin \theta \cdot \Delta \phi)^2 + (\Delta \theta)^2, \quad (6.31)$$

where  $\Delta \phi$  and  $\Delta \theta$  are the angular errors in the azimuth and elevation, respectively. The asymptotic mean-square angular error (MSAE) of a DOA estimator is defined [132] as

$$\text{MSAE} = E(\delta^2), \quad (6.32)$$

where  $E$  stands for the expectation. The Cramer-Rao lower bound for MSAE that is asymptotically attainable by ML is [132]

$$\text{MSAE}_{\text{CRB}} = (\sin \theta)^2 \text{CRB}(\phi) + \text{CRB}(\theta). \quad (6.33)$$

Fig. 6.3a shows the CRB on the MSAE computed for the array of monopoles on the UAV, and Fig. 3b shows the computation for the same array on the PEC. Here,  $SNR = 15$  dB and  $N = 1$ . (We define  $SNR$  as the ratio of the average power received by the array and the noise power.) The lower bound on the MSAE for the array on the UAV is reasonably small. Hence, because of the multipath, the linear array on the UAV is able to estimate separately both azimuth and elevation using single-frequency data. If there is no multipath, the CRB grows extremely large, confirming that the uniform linear array is not capable of resolving both spherical angles of the incident wave. Fig. 6.4 shows the lower bound on the MSAE computed using  $N = 15$  frequency samples. In the case of the array on the UAV, the frequency-swept measurements improved the estimation accuracy. In the case without the multipath, the improvement was negligible.

The response of the antennas varies with the frequency. This variation is not the same for all directions, particularly for antennas in complex environments such as platforms.



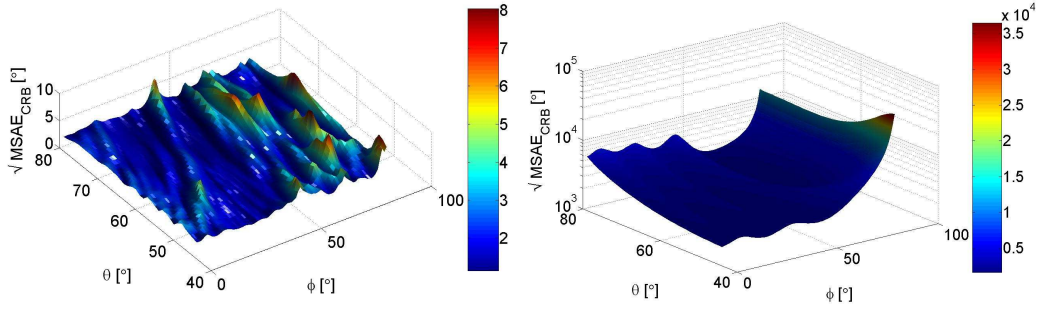


Fig. 6.3: The lower bound for MSAE computed for a uniform linear array of seven monopoles mounted on the (a) Predator and (b) PEC using  $N = 1$  frequency sample. The adopted  $SNR$  is 15 dB.

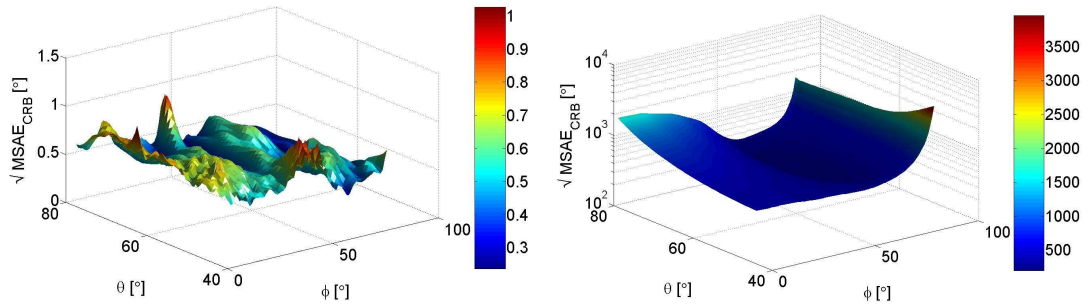


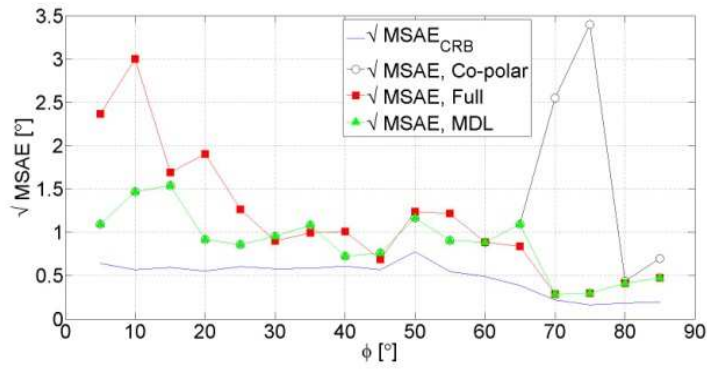
Fig. 6.4. The lower bound for MSAE computed for a uniform linear array of seven monopoles mounted on the (a) Predator and (b) PEC using  $N = 15$  frequency samples. The adopted  $SNR$  is 15 dB.

When the number of frequency samples is increased, the CRB decreases because new pieces of information are added. However, this decrease is not the same for all DOAs because the response of the array on the UAV changes with both the DOA and frequency. In contrast, the radiation pattern of the array on the PEC changes with the frequency in *almost* the same way for all directions. (The coupling among antennas is the only source of this spatial variation.) Hence, in this case the CRB *almost* uniformly decreases for all

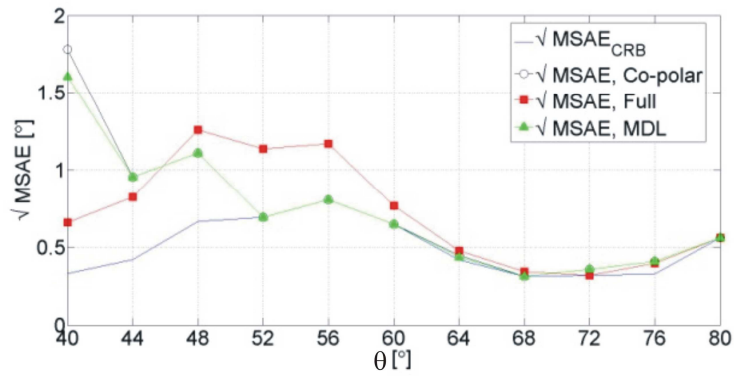
DOAs with increased frequency samples.

We further investigate the influence of the multipath by performing an ML estimation of the unknown parameters. We compare two measurement models for the array of monopoles on the UAV: (a) a model that takes into account both the co-polar and the cross-polar components of the array response (full model) and (b) a model that neglects the cross-polarization (co-polar model). The measurement matrix for the full model is  $\mathbf{H}$  given by (6.10), and the measurement matrix for the co-polar model is  $\mathbf{H}_0$  defined in (6.10). We use MDL (6.28) in deciding between these two models.

We compute MSAE numerically using Monte Carlo (MC) simulations and assuming  $N=15$  frequency measurements with  $SNR=15$  dB. In Fig. 6.5, we present results obtained by 200 independent numerical experiments. If the cross-polar component of the received signal is not significant, the co-polar model (white circles) yields smaller MSAE than the full model (red squares). This situation is illustrated in Fig. 6.5a for  $\phi < 70^\circ$ . Otherwise, the full model yields better results.



(a)



(b)

Fig. 6.5: Square root of MSAE for (a)  $\theta = 50^\circ$  and (c)  $\phi = 50^\circ$ . Results are obtained by 200 independent Monte Carlo simulations with  $SNR = 15$  dB.

## 6.5.2 Two sources

We now study the capability of the system with multipath to resolve two sources with closely spaced angles of arrival. In this case, we define  $SNR$  as the ratio of the average received power from one of the sources and the noise power. We suppose that the signals have equal power.

We first consider the scenario in which the number of the signals is known in advance

( $K = 2$ ) and compute the theoretical resolution by means of the CRB. In this approach, two signals are said to be resolvable in some parameter  $\delta = |\delta_1 - \delta_2|$  (e.g., frequency or angle) if

$$\delta > 2 \max(\sigma_{\delta_1}, \sigma_{\delta_2}), \quad (6.34)$$

where  $\delta_1$  and  $\delta_2$  are the parameter values corresponding to the first and second signal, respectively; and  $\sigma_{\delta_1}$  and  $\sigma_{\delta_2}$  are their respective standard deviations determined by the CRB [133]. Since both the azimuth and elevation of each signal are unknown, we define the resolution as

$$\delta(\theta_1, \phi_1, \theta_2, \phi_2) > 2 \max\left(\sqrt{\text{MSAE}_{\text{CRB1}}(\theta_1, \phi_1)}, \sqrt{\text{MSAE}_{\text{CRB2}}(\theta_2, \phi_2)}\right), \quad (6.35)$$

where  $(\theta_1, \phi_1)$  and  $(\theta_2, \phi_2)$  are the respective DOAs of the first and the second wave, and the  $\text{MSAE}_{\text{CRB1}}$  and  $\text{MSAE}_{\text{CRB2}}$  are the respective Cramer-Rao bounds on the MSAE of the first and the second wave. We determine these bounds assuming that both waves are present. In this way, we take into account the correlation between the estimation errors.

Performing computations (6.35) for every incident direction, assuming  $\theta_2 = \theta_1$ ,  $\phi_2 = \phi_1 + \delta$ , we obtain that  $\max(\delta(\theta_1, \phi_1, \theta_2, \phi_2)) = 8^\circ$  is the worst-case theoretical limit for resolving two waves using the array on monopoles on the UAV, under the given  $SNR$ . We show in Fig. 6.6 the CRB for the MSAE of the first wave for  $\delta = 8^\circ$ . Due to the increase of the number of the unknown parameters, the MSAE is now larger than the MSAE obtained for a single incident wave. The results for the second wave are similar.

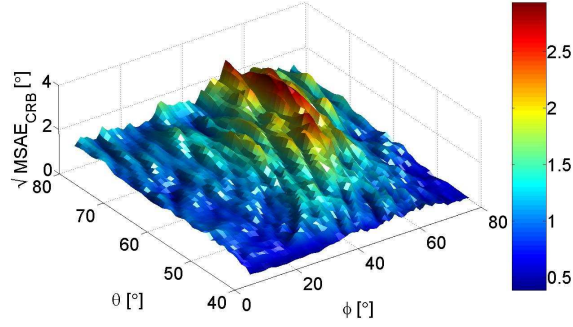


Fig. 6.6: Square root of lower bound for MSAE of the first wave as a function of its DOA. The DOA of the second wave is  $\theta_2 = \theta_1$ ,  $\phi_2 = \phi_1 + \delta$ ,  $\delta = 8^\circ$ . Computations are performed for the array of monopoles on the UAV with  $SNR = 15$  dB and  $N = 20$ .

We now consider the scenario in which the number of the waves is unknown. In this case we study the resolution of the system empirically by means of MDL, letting MDL decide whether one signal or two signals are present. (At reasonably high  $SNR$ , the probability that MDL will decide that three signals are present or no signal is present is negligible). Hence, MDL chooses among six hypotheses: one co-polarized wave; one fully polarized wave; two co-polarized waves; two fully polarized waves; two waves, with the first being co-polarized and the second being fully polarized; and two waves, with the first being fully polarized and the second being co-polarized). The approximate success rate of MDL is [133]

$$P_d(\delta; \theta_1, \phi_1, \theta_2, \phi_2) \approx \frac{1}{N_{\text{exp}}} \sum_{i=1}^{N_{\text{exp}}/2} \sum_{K=1}^2 I_i(\hat{K} = K | \delta), \quad (6.36)$$

where  $K$  is the actual number of waves,  $\hat{K}$  is the estimated number of signals,  $N_{\text{exp}}$  is the number of experiments, and  $I_i(\hat{K} = K)$  is one if  $\hat{K} = K$  in the  $i$ th experiment and zero otherwise. For the first half of the experiments we assume only one incident

signal; for the second half we assume two incident signals. The empirical resolution is the value of  $\delta(\theta_1, \phi_1, \theta_2, \phi_2)$  for which  $P_d(\delta) = \alpha$ , where  $\alpha$  is the desired success rate. As an illustration, we present in Fig. 7 the empirical resolution limit for  $\phi_1 = 20^\circ$  and  $\phi_1 = 60^\circ$ . The results were computed in 200 experiments for  $\alpha \approx 0.99$ . In the same figure we also show the resolution predicted by the CRB. However, in the latter case the number of the waves is assumed to be known.

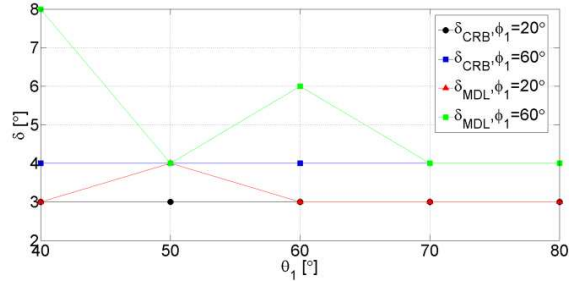


Fig. 6.7: Resolution of the array of monopoles on the UAV computed by CRB and MDL with  $SNR = 15$  dB and  $N = 20$ .

## 6.6 Experiment

We show experimentally that exploiting diffraction allows estimating both azimuth and elevation of the incident signal, using a uniform linear array of monopoles at a single frequency. Since we did not have a UAV Predator, we used a square metallic plate as the mounting platform. The side length of the plate was 1 m. The array was located along the diagonal of the plate as illustrated in Fig. 6.8. As in the case of the UAV, the only source of the multipath for the array in the experiment was the diffraction. The parameters of the array, except for the number of sensors, were the same as the ones used in Section 6.3.

For technical reasons, the array in the experiment had eight monopoles instead of seven. We took a folded dipole as the unknown radiation source. The distance between the feed of the folded dipole and the center of the plate was approximately 2.2 m. We acquire the measurements in the frequency domain with the Agilent E5062A Vector Network Analyzer.

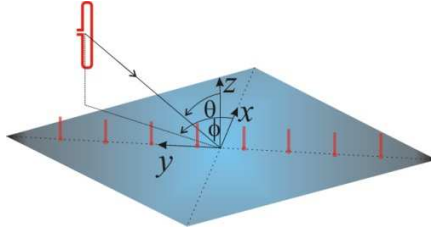


Fig. 6.8: The receiving array on the plate and the adopted coordinate system.

We used phase conjugation [81] to compute the signal spectrum from the measurements,

$$I(\theta, \phi, f_n) = \sum_{m=1}^M E^*(\theta, \phi, f_n, \mathbf{r}_m) V(f_n, \mathbf{r}_m), \quad (6.37)$$

where  $V(f_n, \mathbf{r}_m)$  is the measured signal at the  $n$ th frequency at the  $m$ th sensor,  $E(\theta, \phi, f_n, \mathbf{r}_m)$  is the embedded radiation pattern of the  $m$ th sensor at the  $n$ th frequency in the direction of  $(\theta, \phi)$ , and the asterisk stands for conjugation. The radiation pattern of the array on the plate (without the folded dipole) was obtained using WIPL-D Pro.

In the experiment, we kept the zenith angle fixed at  $\theta = 75^\circ$  and varied the azimuth so that  $\phi = 0^\circ$ ,  $\phi = 45^\circ$ , and  $\phi = 90^\circ$ . We computed the spectra at each of the frequencies:  $f = 0.75$  GHz,  $f = 1$  GHz,  $f = 1.5$  GHz, and  $f = 2$  GHz. We show the results in Figs. 6.9-11. In all considered directions and at all frequencies, the azimuth was

estimated accurately. Due to symmetry, the array could not resolve whether the signal impinged from the left or right side of its axis. However, this ambiguity could have been resolved by placing the array asymmetrically on the plate or by using a plate with an irregular shape. The estimated elevation was smaller than the real one at lower frequencies ( $f = 0.75$  GHz,  $f = 1$  GHz). As the frequency increased, the electrical size of the plate became larger and the error diminished.

In Fig. 12, we show the direct path (denoted by  $r$ ) and the diffracted paths (denoted by  $r_1$  and  $r_2$ ) for one of the sensors, computed using the geometrical theory of diffraction (GTD). The diffraction points (white circles) behave as variable parasitic elements that transform a linear array into an equivalent spatial array. In this way, it is possible to resolve both the azimuth and elevation using single-frequency data, unlike the case for which there is no diffraction (i.e., the array is mounted on the PEC). According to Keller's diffraction functions [127], the magnitude of the diffracted field varies as  $1/\sqrt{d/\lambda}$ , where  $d$  is the distance between the diffraction point and the sensor, and  $\lambda$  is the free-space wavelength at the operating frequency. Because of this slow decay, the effective aperture grows with the electrical size of the plate, as in the case of a standard spatial array. However, if the electrical size of the plate becomes very large, the diffraction becomes negligible, and the performance of the array becomes the same as for an array on the PEC.



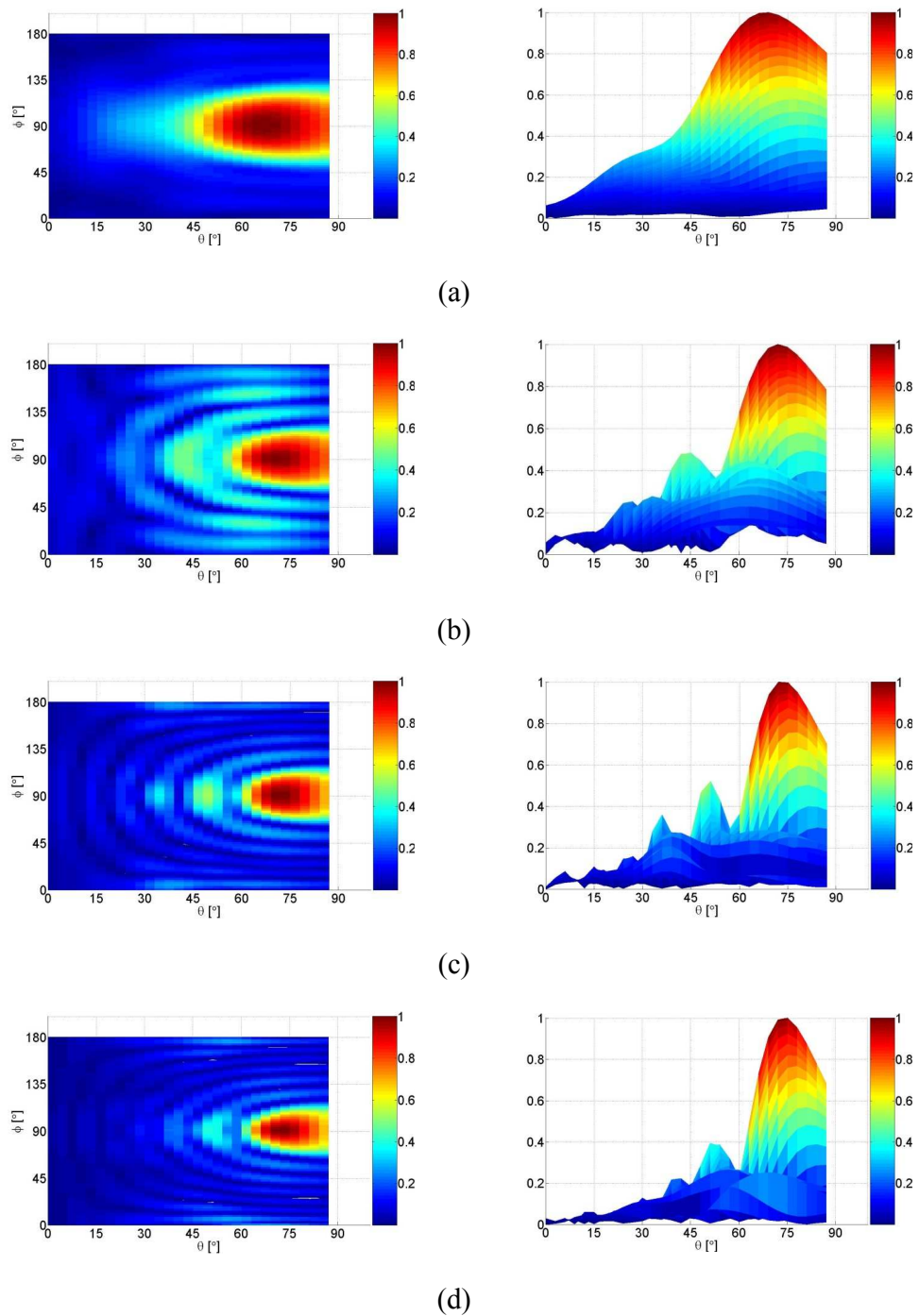
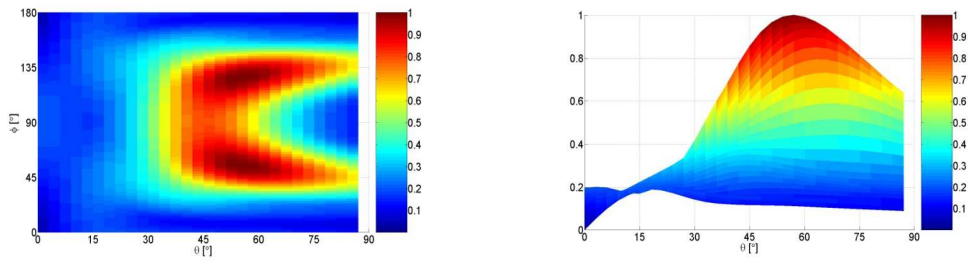
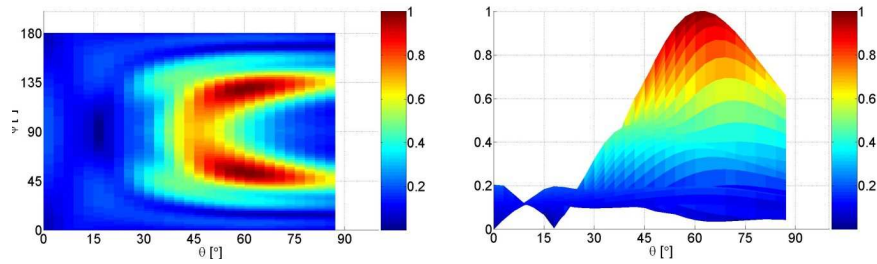


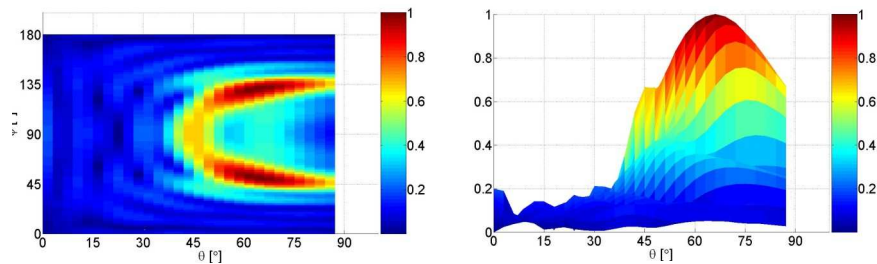
Fig. 6.9: The experimental verification of the 3D localization by means of diffraction. ( $\phi = 90^\circ$ ,  $\phi = 75^\circ$ ) was computed using single-frequency measurements at (a) 0.75 GHz, (b) 1 GHz, (c) 1.5 GHz, and (d) 2 GHz.



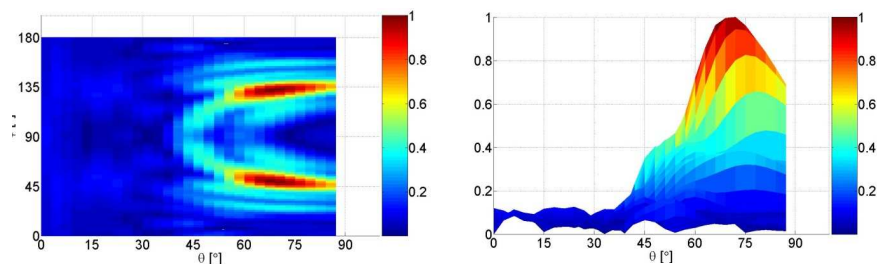
(a)



(b)



(c)



(d)

Fig. 6.10: The experimental verification of the 3D localization by means of diffraction. ( $\phi = 45^\circ$ ,  $\phi = 75^\circ$ ) was computed using single-frequency measurements at (a) 0.75 GHz, (b) 1 GHz, (c) 1.5 GHz, and (d) 2 GHz.

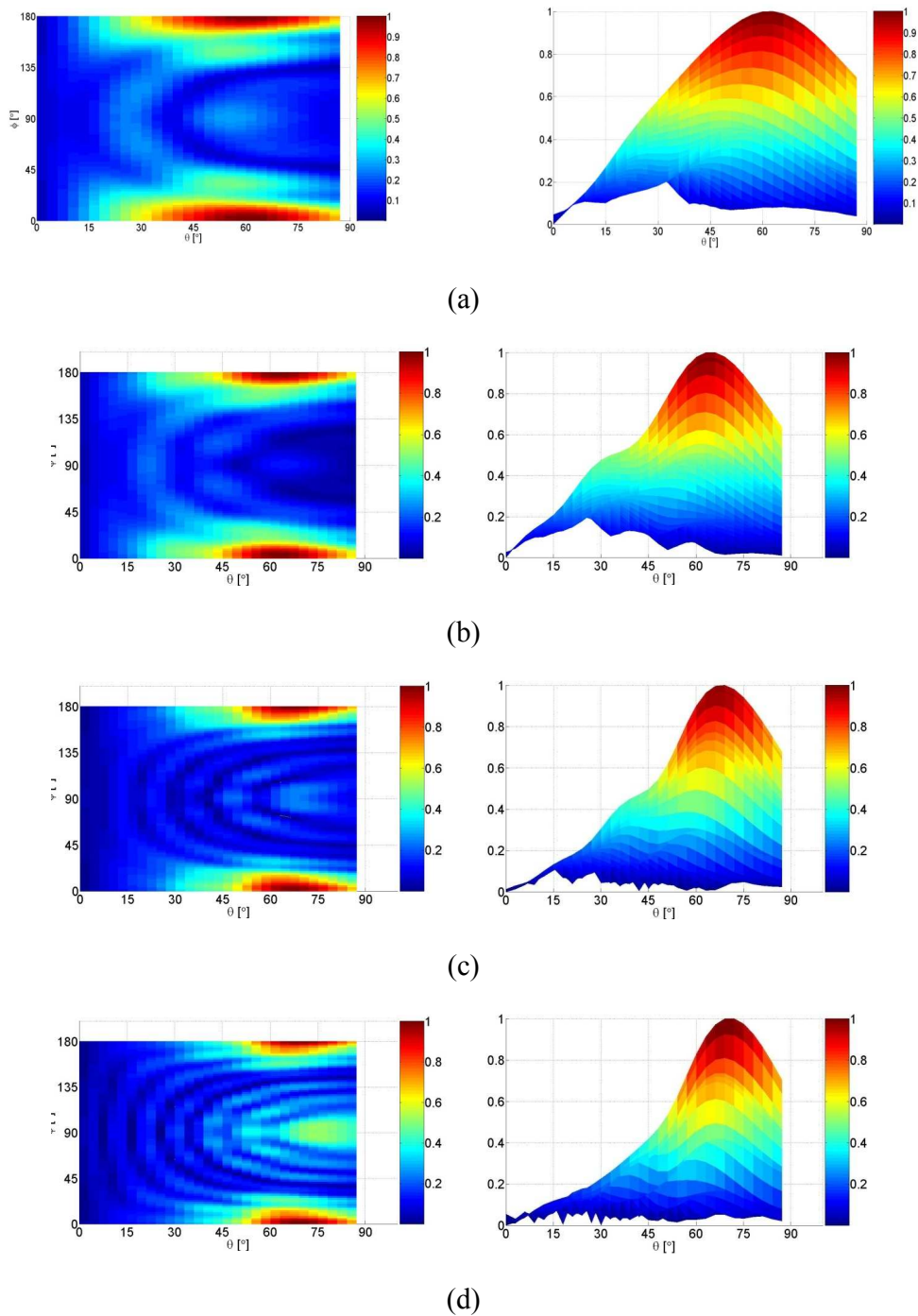


Fig. 6.11: The experimental verification of the 3D localization by means of diffraction. ( $\phi = 0^\circ, \phi = 75^\circ$ ) was computed using single-frequency measurements at (a) 0.75 GHz, (b) 1 GHz, (c) 1.5 GHz, and (d) 2 GHz.

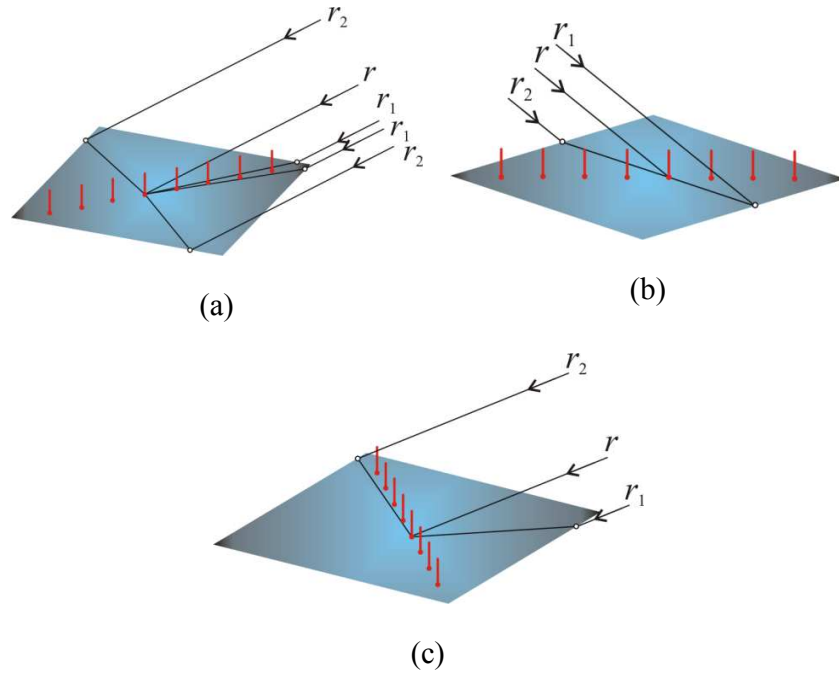


Fig. 6.12: Diffracted rays and direct ray for DOA: (a) ( $\phi = 90^\circ, \theta = 75^\circ$ ), (b) ( $\phi = 45^\circ, \theta = 75^\circ$ ), and (c) ( $\phi = 0^\circ, \theta = 75^\circ$ ).

## 6.7 Summary

We have demonstrated that the multipath due to the interaction between sensor arrays and the hosting platform enables 3D direction of arrival estimation with uniform linear arrays even at single frequency measurements. We considered, theoretically, the array mounted on the UAV Predator and, experimentally, the array mounted on a finite conducting plate. In both cases, the diffraction of the incident signals from the platform was the only source of multipath. In this way, the sensing arrays mimic the human auditory system, which exploits diffraction from the head.

We used the Cramer-Rao bound to compare the performance of the array with and

without the platform. The response of the array on the platform was similar to the response of the array consisting of driven elements (sensors) and several parasitic elements (diffraction centers). These parasitic elements enlarged the effective size of the sensing system and improved the ability of the system to resolve closely spaced signals.

# Chapter 7

## Conclusions

In real-life scenarios, targets are often obscured and can be inferred only indirectly by means of electromagnetic sensing. We used stochastic and deterministic methods to infer the unknown targets and their environment. To achieve better results, we employed physical models of the electromagnetic interaction among the targets, surroundings, and sensing arrays. Below, we summarize our key contributions.

### 7.1 Contributions

Using jump-diffusion algorithm and prior knowledge of typical building layouts, we have developed an iterative method that identified the number and positions of inner walls. To reduce the unknown parameter space, we regarded the interior as a collection of unknown rectangular walls. By means of stochastic geometry together with a physical model that accounted for the scattering among the walls, we optimized the characteristics of the walls. The method employed a wide frequency bandwidth; it used low-frequency estimates to initiate more accurate estimation at higher frequencies. The higher frequencies were chosen in an adaptive manner, based on the convergence rate in the

previous iteration. Efficient utilization of the frequency spectrum, as well as the inclusion of the multipath, made it possible to estimate building layouts using only a few frequencies.

To address the estimation of targets hidden behind reinforced concrete walls, we studied the influence of the reinforcement on target imaging. Unless the frequency was sufficiently high (depending on the distance between adjacent bars), neglecting the wall response yielded poor estimation results. We improved the estimation significantly by modeling the waveform distortion caused by the reinforced wall. We obtained focused images that accurately represented the contours of the targets. The algorithm was robust to ambiguities in bar parameter values.

Using the equivalent source method and  $l_1$  regularization, we derived a two-step method that estimated the number and shape of PEC targets concealed in a dielectric medium. The method determined positions of the equivalent sources close to the targets' contours, thus revealing their shape. Because of  $l_1$  regularization, a single step algorithm recovered only pieces of the targets' contours. Hence, we used the equivalent sources found in the first step to enlarge the reconstructed areas in the second step. By means of mirroring theory, we designed an experimental model to verify our numerical results. The agreement was excellent. However, a metal enclosure in the experimental model, created multiple scattering, so the induced currents on the targets were not sparse. Because of the enclosure, the induced currents varied significantly with the frequency. Hence, the images obtained at different frequencies recovered different parts of targets' contours,

unlike the case without the enclosure.

We have demonstrated that the multipath from sensor-array platforms allows 3D direction finding with uniform linear arrays, even with single-frequency measurements. To the best of our knowledge, the scattering from platforms has not been utilized in estimating direction of arrival. In contrast, the utilization of the multipath from the target surrounding has been widely studied. However, the multipath close to the sensors is known in advance, unlike the multipath close to the targets, which is only partially known. We used the Cramer-Rao bound to investigate the influence of the multipath. Moreover, we verified our approach experimentally by considering an array mounted on a finite conducting plate.

## **7.2 Future work**

In future work, we will extend our models to accommodate 3D space. Besides being more accurate, 3D models efficiently use polarization diversity, which is particularly important in cluttered environments.

We will adapt the sparse localization method for through-the-wall applications, applying a hybrid approach that combines electric field integral equations and geometrical optics. In this way, we will utilize the efficiency of geometrical optics, necessary for wall modeling, and the accuracy of the integral equations, helpful in target modeling. We will also introduce the equivalent magnetic sources. By using both types of equivalent sources, we will be able to infer the targets' material in addition to their shape.



We will also study the application of sparse electromagnetic imaging in scenarios with pronounced multipath.

# Appendix

In the appendix, we describe in detail the transformations from the jump-diffusion algorithm used in Chapter 3:

- Birth: A new wall is added to the current configuration. The parameters of the new wall are drawn as  $x' \sim \text{Unif}[x_{\min}, x_{\max}]$ ,  $y' \sim \text{Unif}[y_{\min}, y_{\max}]$ ,  $l' \sim \text{Unif}[l_{\min}, l_{\max}]$ , where  $x_{\min, \max}$ ,  $y_{\min, \max}$ , are the boundaries of the building, and  $l_{\min, \max}$  are adopted limits for the wall length. For the  $4 \text{ m} \times 4 \text{ m}$  building we set:  $x_{\min, \max} = \pm 2 \text{ m}$ ,  $y_{\min, \max} = \pm 2 \text{ m}$ ,  $l_{\min} = 0.5 \text{ m}$ ,  $l_{\max} = 2 \text{ m}$ .
- Death: A randomly selected inner wall is removed from the current configuration.
- Translation: New coordinates of the center of the wall are drawn as  $x' \sim N(x, \sigma_x^2 / i)$ ,  $y' \sim N(y, \sigma_y^2 / i)$ , where  $x, y$  are the current center coordinates,  $i$  is the frequency step, and  $\sigma_x, \sigma_y$  are the adopted constants. We set  $\sigma_x = \sigma_y = 1 \text{ m}$ .
- Elongation: The new length is drawn as  $l' \sim N(l, \sigma_l^2 / i)$ , where  $l$  is the length of the wall. We set  $\sigma_l = 0.5 \text{ m}$ .
- Rotation: The orientation of a randomly selected wall is flipped ( $\alpha'$ ). The

assumed wall orientations are  $0^\circ$ ,  $\pm 45^\circ$  or  $90^\circ$ .

- Regeneration: All parameters of the randomly selected wall are perturbed. The new wall parameters are drawn as  $x' \sim \text{Unif}[x_{\min}, x_{\max}]$ ,  $y' \sim \text{Unif}[y_{\min}, y_{\max}]$ ,  $l' \sim \text{Unif}[l_{\min}, l_{\max}]$ ,  $\alpha \sim \text{Unif}\{0, \pm 45^\circ, 90^\circ\}$ .
- Merge: A randomly selected inner wall is merged with a nearby wall of the same orientation. The center of the merged wall is the centroid of the tightest rectangle encompassing the original two walls, and its length is drawn as  $l' \sim \text{Uniform}[d_{\min}, d_{\max}]$ , where  $d_{\min}$  and  $d_{\max}$  are defined in Fig. 3.2.
- Optimization. The parameters of a randomly selected wall  $(x', y', l', \alpha')$  are optimized using simplex algorithm.
- We adopted the probabilities for the above transformations as in Tab. I, where  $k$  is the number of the walls in the layout ( $1 \leq k \leq 15$ ). In this table,  $c$  is a constant that assures  $\sum_i p_T(i) = 1$ .

TABLE II  
PROBABILITY DISTRIBUTIONS FOR TRANSFORMATIONS.

Transformation	Probabilities (step $i = 1$ )	Probabilities (step $i > 1$ )
Birth	$10\exp(-0.2k)c$	$4\exp(-0.2k)c$
Death	$c$	$c$
Translation	$2c$	$2c$
Elongation	$c$	$2c$
Rotation	$c$	$c$
Regeneration	$c$	0
Merge	0	$2c$
Optimization	0	$c$

## References

- [1] M. M. Nikolic, A. Nehorai, A. R. Djordjevic, "Radar estimation of building layout estimation using jump-diffusion," *Proc. 2nd IEEE Int. Workshop on Computational Advances in Multi-Sensor Adaptive Processing*, St. Thomas, U.S. Virgin Islands, Dec. 2007.
- [2] M. M. Nikolic, M. Ortner, A. Nehorai, and A. R. Djordjevic, "Estimating building layouts using radar and jump-diffusion algorithm," *IEEE Trans. Antennas Propagat.*, vol. 57, no. 3, pp. 768-776, March 2009.
- [3] W. C. Chew and Y. M. Wang, "Reconstruction of two-dimensional permittivity distribution using the distorted Born iteration method," *IEEE Trans. Med. Imag.*, vol. 9, no. 2, pp. 218-225, Jun. 1990.
- [4] Y. M. Wang and W. C. Chew, "An iterative solution of the two-dimensional electromagnetic inverse scattering problem," *Int. J. Imag. Syst. Technol.*, vol. 1, pp. 100-108, 1989.
- [5] N. Joachimowicz, C. Pichot, J. P. Hugonin, "Inverse scattering: an iterative numerical method for electromagnetic imaging," *IEEE Trans. Antennas Propagat.*, vol. 39, pp. 1742-1752, 1991.
- [6] A. G. Tijhuis, K. Belkebir, A. Litman, and B. P. de Hon, "Theoretical and computational aspects of 2-D inverse profiling," *IEEE Trans. Geosci. Remote*

*Sens.*, vol. 39, no. 6, pp. 316–1330, June 2001.

- [7] O. M. Bucci and T. Isernia, “Electromagnetic inverse scattering: Retrievable information and measurement strategies,” *Radio Sci.*, vol. 32, no. 6, pp. 2123-2137, November 1997.
- [8] O. M. Bucci, L. Crocco, T. Isernia, and V. Pascazio, “Inverse scattering problems with Multifrequency Data: Reconstruction Capabilities and Solution Strategies,” *IEEE Trans on Geosci. Remote sensing*, vol. 38, no 4, July 2000.
- [9] L. Garnero, A. Franchois, J.-P Hugonin, C. Pichot, N. Joachimowicz, “Microwave imaging-complex permittivity reconstruction-by simulated annealing,” *IEEE Transactions on Microwave Theory and Techniques*, vol. 39, no. 11, pp. 1801-1807, Nov 1991.
- [10] P. J. Green, “Reversible Jump Markov Chain Monte Carlo Computation and Bayesian Model Determination,” *Biometrika*, vol. 82, no. 4, pp. 711- 732, 1995.
- [11] U. Grenander and M. Miller, “Representation of Knowledge in Complex Systems,” *J. Royal Statistics Soc.*, vol. B56, pp. 97-109, 1994.
- [12] M. Ortner, Descombes X, Zerubia J, “Building Outline Extraction from Digital Elevation Models Using Marked Point Processes,” *International Journal of Computer Vision*, Vol. 72 , Issue 2, pp. 107-132, April 2007.
- [13] M. I. Miller, U. Grenander, J. A. O'Sullivan, D. L. Snyder: “Automatic target recognition organized via jump-diffusion algorithms,” *IEEE Transactions on Image Processing*, vol. 6 pp. 157-174, 1997.
- [14] E. M. Lavelly, Y. Zhang, E. H. Hill III, Y. Lai, P. Weichman, A. Chapman,

- “Theoretical and experimental study of through-wall microwave tomography inverse problems,” *Journal of the Franklin Institute*, vol. 345, no 6, pp. 592-617, Sep. 2008.
- [15] G. Hickman, J.L. Krolik, “A Graph-Theoretic Approach to Constrained Floor Plan Estimation From Radar Measurements,” *IEEE Transactions on Signal Processing*, vol.57, no.5, pp.1877-1888, May 2009.
- [16] F. Ahmad, M. G. Amin, and S. A. Kassam, “Synthetic aperture beamformer for imaging through a dielectric wall,” *IEEE Trans. Aerosp. Electron. Syst.*, vol. 41, no. 1, pp. 271–283, Jan. 2005.
- [17] F. Ahmad and M. G. Amin, “A noncoherent radar system approach for through-the-wall imaging,” *Proc. SPIE Symposium on Defense and Security, Sensors, and Command, Control, Communications, and Intelligence Technologies*, Vol. 5778, pp. 196-207, March-April 2005.
- [18] F. Soldovieri, R. Solimene, “Through-Wall Imaging via a Linear Inverse Scattering Algorithm,” *IEEE Geoscience and Remote Sensing Letters*, vol. 4, no. 4, pp. 513-517, Oct. 2007.
- [19] R. Solimene, F. Soldovieri, G. Prisco, “A Multiarray Tomographic Approach for Through-Wall Imaging,” *IEEE Transactions on Geoscience and Remote Sensing*, vol. 46, no. 4, pp. 1192-1199, April 2008.
- [20] G. Wang and M. Amin, “Imaging through unknown walls using different standoff distances,” *IEEE Transactions on Signal Processing*, Vol. 54, No. 10, pp. 4015–4025, Oct. 2006.
- [21] M. Dehmollaian and K. Sarabandi, “Simulation of through-wall

- microwave imaging: forward and inverse models,” in *Proc. of IEEE International Geoscience and Remote Sensing Symposium*, 2006.
- [22] Y.-S. Yoon and M. G. Amin, “Compressive sensing technique for high-resolution radar imaging,” *Proceedings of the SPIE Symposium on Defense and Security*, Orlando, Florida, March 2008.
- [23] Y. Yoon and M. G. Amin, “Through-the-wall radar imaging using compressive sensing along temporal frequency domain,” *International Conference on Acoustics, Speech, and Signal Processing (ICASSP)*, pp. 2806–2809, Dallas, Texas, USA, 2010.
- [24] H. Qiong, Q. Lele Qu, W. Bingheng, and F. Guangyou, “UWB through-wall imaging based on compressive sensing,” *IEEE Trans. Geosci. Remote Sens.*, vol. 48, no. 3, pp. 1408–1415, Mar. 2010.
- [25] M. Leigsnering, C. Debes and A. M. Zoubir, “Compressive sensing in through-the-wall radar imaging,” *International Conference on Acoustics, Speech, and Signal Processing (ICASSP)*, pp. 2806–2809, Prague, Czech Republic, 2011.
- [26] M. M. Nikolic, A. Nehorai, A. R. Djordjevic, “Estimating moving targets behind reinforced walls using radar,” *IEEE Trans. Antennas Propagat*, vol. 57, no. 11, pp. 3530-3538, Nov. 2009.
- [27] E. Richarlot, M. Bonilla, W. Wong, V. Fouad-Hanna, H. Baudrand, and J. Wiat, “Electromagnetic propagation into reinforced concrete walls,” *IEEE Trans. Microwave Theory Tech.*, vol. 48, pp. 357–366, Mar. 2000.
- [28] R. A. Dalke, C. L. Holloway, P. McKenna, M. Johansson, and A. S. Ali, “Effects of reinforced concrete structures on RF communications,” *IEEE Trans.*



*Electromagn. Compat.*, vol. 42, pp. 486–496, Nov. 2000.

- [29] R. Paknys, “Reflection and transmission by reinforced concrete-numerical and asymptotic analysis,” *IEEE Trans. Antennas Propagat.*, vol. 51, no. 10, pp. 2852-2861, Oct. 2003.
- [30] R. F. Harrington, *Field computation by moment methods*, Krieger Publishing Co., Malabar, FL, 1982.
- [31] A. R. Djordjević, T. K. Sarkar, and S. M. Rao “Analysis of finite conductivity cylindrical conductors excited by axially-independent TM electromagnetic field,” *IEEE Microwave Theory Techn.*, Vol. 33, No. 10, Oct. 1985, pp. 960–966.
- [32] R. Tibshirani, “Regression shrinkage and selection via lasso,” *J. Roy. Statist. Soc. Ser. B*, vol. 58, pp. 267–288, 1996.
- [33] S. Chen, D. L. Donoho, and M. A. Saunders, “Atomic decomposition by basis pursuit,” *SIAM J. Sci. Comp.*, vol. 20, no. 1, pp. 33–61, 1998.
- [34] D. M. Malioutov, M. Cetin, and A. S. Willsky, “Sparse signal reconstruction perspective for source localization with sensor arrays,” *IEEE Trans. Signal Process.*, vol. 53, no. 8, pp. 3010–3022, 2005.
- [35] H. Zou and T. Hastie, “Regularization and variable selection via the elastic net,” *J. R. Statist. Soc. B*, vol. 67, pp. 301–320, 2005.
- [36] R. G. Baraniuk, “Compressive sensing [lecture notes],” *IEEE Signal Process. Mag.*, vol. 24, no. 4, pp. 118-121, July 2007.
- [37] E. J. Candes and T. Tao, “The Dantzig selector: Statistical estimation when  $p$  is much larger than  $n$ ,” *Ann. Statist.*, vol. 35, pp. 2313–2351, 2007.

- [38] E. J. Candes and M. B. Wakin, "An introduction to compressive sampling," *IEEE Signal Process. Mag.*, vol. 25, no. 2, pp. 21–30, Mar. 2008.
- [39] L. Carin, D. Liu, W. Lin, and B. Guo, "Compressive sensing for multi-static scattering analysis," *Journal of Computational Physics*, vol. 228, no. 9, May, 2009.
- [40] L. Carin, "On the relationship between compressive sensing and random sensor arrays," *IEEE Antennas Propag. Mag.*, vol. 5, no. 5, pp. 72–81, Oct. 2009.
- [41] L. C. Potter, E. Ertin, J. T. Parker, M. Cetin, "Sparsity and compressed sensing in radar imaging," *Proc. IEEE*, vol. 98, no. 6, pp. 1006-1020, June 2010.
- [42] M. M. Nikolic, A. Nehorai, and A. Djordjevic, "Sparse Electromagnetic Imaging", *Proc. of EUCAP*, Rome, April 11-15.
- [43] M. M. Nikolić, G. Tang, and A. Nehorai, "Electromagnetic imaging using compressive sensing," *48th Allerton Conf. on Communication, Control and Computing*, 2010.
- [44] M. M. Nikolic, A. Nehorai, and A. Djordjevic, "Electromagnetic Imaging of Hidden 2D PEC Targets Using Sparse Signal Modeling," in revision for *IEEE Trans on Geosci. Remote sensing*.
- [45] A. Kirsch, R. Kress, P. Monk, and A. Zinn, "Two methods for solving the inverse acoustic scattering problem," *Inverse Problems*, vol. 4, pp. 749-770, 1988.
- [46] C. Lin and Y. Kiang, "Inverse scattering for conductors by the equivalent source method," *IEEE Trans. Antennas Propag.*, vol. 44, no. 3, pp. 310-316, Mar. 1996.
- [47] G. P. Otto and W. C. Chew: "Microwave inverse scattering - local shape

- function imaging for improved resolution of strong scatterers," *IEEE Microwave Theory Techn.*, vol. 42, no. 1, pp. 137-141, Jan 1994.
- [48] W.C. Chew, *Waves and fields in inhomogeneous media*, Wiley-IEEE Press, 1999.
- [49] S. Caorsi, G. Gragnani, and M. Pastorino, "Equivalent current density reconstruction for microwave imaging purposes, *IEEE Microwave Theory Techn.*, vol. 37, no. 5, pp. 910-916, May 1989.
- [50] Y. Álvarez, B. A. D. Casas, C. García, and F. Las-Heras, "The volumetric sources reconstruction method and its applications to geometry reconstruction," *EUCAP 2010*, Barcelona, Spain.
- [51] D. Colton, H. Haddar, and M. Piana, "The linear sampling method in inverse electromagnetic scattering theory," *Inv. Prob.*, vol. 19, no. 6, pp. S105–S137, Dec. 2003.
- [52] A. Kirsch, "The factorization method for Maxwell's equations," *Inv. Prob.*, vol. 20, no. 6, pp. 117–134, Dec. 2004.
- [53] A. Liseno and R. Pierri, "Shape reconstruction by spectral data of the far-field operator: Analysis and performances," *IEEE Trans. Antennas Propag.*, vol. 52, no. 3, pp. 899–903, Mar. 2004.
- [54] B. Gebauer, M. Hanke, A. Kirsh, W. Muniz, and C. Scheider, "A sampling method for detecting buried objects using electromagnetic scattering," *Inv.Prob.*, vol. 21, no. 6, pp. 2035–2050, Dec. 2005.
- [55] F. Cakoni, M'B. Fares, and H. Haddar, "Analysis of two linear sampling methods applied to electromagnetic imaging of buried objects," *Inv. Prob.*, vol.

- 22, no. 3, pp. 845–867, Feb. 2006.
- [56] R. Potthast, “A survey on sampling and probe methods for inverse problems,” *Inv. Prob.*, vol. 22, no. 2, pp. R1–R47, Apr. 2006.
- [57] C. Fischer, A. Herschlein, M. Younis, and W. Wiesbeck, “Detection of antipersonnel mines by using the factorization method on multistatic ground-penetrating radar measurements,” *IEEE Trans. Geosci. Remote Sens.*, vol. 45, no. 1, pp. 85–92, Jan. 2007.
- [58] I. Catapano, L. Crocco, and T. Isernia, “On simple methods for shape reconstruction of unknown scatterers,” *IEEE Trans. Antennas Propag.*, vol. 55, no. 5, pp. 1431–1436, May 2007.
- [59] I. Catapano, L. Crocco, and T. Isernia, “Improved sampling methods for shape reconstruction of 3-D buried targets,” *IEEE Trans. Geosci. Remote Sens.*, vol. 46, no. 10, pp. 3265–3173, Oct. 2008.
- [60] A. J. Devaney, “Time reversal imaging of obscured targets from multistatic data,” *IEEE Trans. Antennas Propag.*, vol. 53, no. 5, pp. 1600–1610, May 2005.
- [61] Y. Zhong and X. Chen, “MUSIC imaging and electromagnetic inverse scattering of multiple-scattering small anisotropic spheres,” *IEEE Trans. Antennas Propag.*, vol. 55, no. 12, Dec 2007.
- [62] K. Agarwal and X. Chen, “Applicability of MUSIC-type imaging in two-dimensional electromagnetic inverse problems,” *IEEE Trans. Antennas Propag.*, vol. 56, no. 10, pp. 3217–3223, Oct 2008.
- [63] H. Ammari, E. Iakovleva, D. Lesselier, and G. Perruson, “MUSIC-type

- electromagnetic imaging of a collection of small three-dimensional bounded inclusions,” *SIAM Sci. Comput.*, vol. 29, pp. 674–709, 2007.
- [64] E. Iakovleva, S. Gdoura, D. Lesselier, and G. Perrusson, “Multistatic response matrix of a 3-D inclusion in half space and MUSIC imaging,” *IEEE Trans. Antennas Propag.*, vol. 55, no. 9, pp. 2598–2609, Sep. 2007.
- [65] M. Cheney, “The linear sampling method and the MUSIC algorithm,” *Inverse Problem*, vol. 17, pp. 591–595, 2001.
- [66] A. J. Devaney, E. A. Marengo, and F. K. Gruber, “Time-reversal-based imaging and inverse scattering of multiply scattering point targets,” *J. Acoust. Soc. Am.*, vol. 118, pp. 3129–3138, 2005.
- [67] R. Pierri, A. Liseno, and F. Soldovieri, “Shape reconstruction from PO multifrequency scattered fields via the singular value decomposition approach,” *IEEE Trans. Antennas Propag.*, vol. 49, no. 9, pp. 1333–1343, Sep. 2001.
- [68] A. Brancaccio and G. Leone, “Multimonostatic shape reconstruction of two-dimensional dielectric cylinders by a Kirchhoff-based approach,” *IEEE Trans. Geosci. Remote Sens.*, vol. 48, no. 8, pp. 3152–3161, Aug. 2010.
- [69] R. Solimene, A. Buonanno, F. Soldovieri, and R. Pierri, “Physical optics imaging of 3-D PEC objects: vector and multipolarized approaches,” *IEEE Trans. Geosci. Remote Sens.*, vol. 48, no. 4, pp. 1799–1808, Apr. 2010.
- [70] A. Qing, “Electromagnetic imaging of two-dimensional perfectly conducting cylinders with transverse electric scattered field,” *IEEE Trans. Antennas Propag.*, vol. 50, no. 12, Dec. 2002.
- [71] A Qing, “Electromagnetic inverse scattering of multiple two-dimensional

- perfectly conducting objects by the differential evolution strategy,” *IEEE Trans. Antennas Propag.*, vol. 51, no. 6, pp. 1251-1262, June 2003.
- [72] A. C. Gurbuz, J.H. McClellan, and W.R. Scott, “A compressive sensing data acquisition and imaging method for stepped frequency GPRs,” *IEEE Trans. Signal Process.*, vol. 57, no. 7, pp. 2640–2650, July 2009.
- [73] D. W. Winters, B. D. Van Veen, and S. C. Hagness, “A sparsity regularization approach to the electromagnetic inverse scattering problem,” *IEEE Trans. Antennas Prop.*, vol. 58, no. 1, pp. 145-154, Jan. 2010.
- [74] T. Lo and J. Litva, “Use of a highly deterministic multipath signal model in low-angle tracking,” *IEE Proceedings-F Radar and Signal Processing*, vol. 138, no. 2, pp. 163-171, Apr. 1991.
- [75] S. Sen and A. Nehorai, “Adaptive OFDM radar for target detection in multipath scenarios,” *IEEE Trans. on Signal Processing*, vol. 51, no. 1, pp. 78-90, Jan. 2011.
- [76] D. Berube, P. R. Felcyn, K. Hsu, J. H. Latimer II, and D. B. Swanay, “Target height estimation using multipath over land,” *IEEE Radar Conference*, pp. 88-92, Boston, MA, 2007.
- [77] J. L. Krolik, J. Farrell, and A. Steinhardt, “Exploiting multipath propagation for GMTI in urban environments,” *IEEE Conference on Radar*, April 2006.
- [78] Multipath Exploitation Radar Industry Day, DARPA, August 2007.
- [79] C. J. Nolan, M. Cheney, T. Dowling, and R. Gaburro, “Enhanced angular resolution from multiply scattered waves,” *Inverse Problems*, vol. 22, pp. 1817-

1834, 2006.

- [80] S. Sen and A. Nehorai, "Exploiting close-to-the-sensor multipath reflections using a human-hearing-inspired model," *IEEE Trans. on Signal Processing*, vol. 57, no. 2, pp. 803-908, Feb. 2009.
- [81] B. Ya. Zel'dovich, N. F. Pilipetsky, and V. V. Shkunov, *Principles of Phase Conjugation*, Springer-Verlag, 1985.
- [82] G. Lerosey, J. de Rosny, A. Tourin, and M. Fink, "Focusing beyond the diffraction limit with far-field time reversal," *Science*, vol. 315, p. 1120, 2007.
- [83] M. Fink, "Time reversed acoustics," *Physics Today*, vol. 50, pp. 34-40, 1997.
- [84] Liu, S. Vasudevan, J. Krolik, G. Bal, and L. Carin, "Electromagnetic time-reversal source localization in changing media: Experiment and analysis," *IEEE Trans. Antennas Propagation*, vol. 55, pp. 344-354, Feb. 2007.
- [85] L. Carin, D. Liu, and Y. Xue, "In situ compressive sensing," *Inverse Probl.*, vol. 24, no. 1, pp. 15-23, Feb. 2008.
- [86] Golden, C. Foschini, R. Valenzuela, and P. Wolniansky, "Detection algorithm and initial laboratory results using VBLAST space-time communication architecture," *Electronic Letts.*, vol. 35, 1999. Steyskal, "Synthesis of antenna patterns with imposed near-field nulls," *Electron. Lett.*, vol. 30, no. 24, pp. 2000-2001, Nov. 1994.
- [87] L. Landesa, F. Obelleiro, J. L. Rodriguez, J. A. Rodriguez, F. Ares, and A. G. Pino, "Pattern synthesis of array antennas with additional isolation of near-field arbitrary objects," *Electronics Letters*, vol. 34, no. 16, pp. 1540-1542, Aug. 1998.

- [88] O. M. Bucci, A. Capozzoli, and G. D'Elia, "Power pattern synthesis of reconfigurable conformal arrays with near-field constraints," *IEEE Trans. Antennas Propag.*, vol. 52, no. 1, pp. 132–141, Jan. 2004.
- [89] F. Obelleiro, L. Landesa, J. L. Rodriguez, A. G. Pino, and M. R. Pino, "Directivity optimization of an array antenna with obstacles within its near field region," *Electron. Lett.*, vol. 33, no. 25, pp. 2087–2088, Dec. 1997.
- [90] L. Landesa, F. Obelleiro, J. L. Rodriguez, and A. G. Pino, "Pattern synthesis of array antennas in presence of conducting bodies of arbitrary shape," *Electron. Lett.*, vol. 33, no. 18, pp. 1512–1513, Aug. 1997.
- [91] F. Obelleiro, L. Landesa, J. M. Taboada, and J. L. Rodriguez, "Synthesis of onboard array antennas including interaction with the mounting platform and mutual coupling effects," *IEEE Antennas Propag. Mag.*, vol. 43, no. 2, pp. 76–82, Apr. 2001.
- [92] T. Su and H. Ling, "Array beamforming in the presence of a mounting tower using genetic algorithms," *IEEE Trans. Antennas Propag.*, vol. 53, no. 6, pp. 2011–2019, June 2005.
- [93] P. Stoica and K. C. Sharman, "Maximum likelihood methods for direction-of-arrival estimation," *IEEE Transactions on Acoustics, Speech and Signal Processing*, vol. 38, no. 7, pp. 1132–1143, July 1990.
- [94] M. H. Hansen and B. Yu, "Model selection and the principle of minimum description length," *Journal of the American Statistical Association*, vol. 96, no. 454, pp. 775–776, Jun 2001.
- [95] R. F. Harrington, *Time-Harmonic Electromagnetic Fields*, McGraw-Hill,



New York, 1961.

- [96] D. M. Pozar, *Microwave engineering*, Third Edition, John Wiley & Sons, 2005.
- [97] J. Nelder, R. Mead, "A simplex method for function minimization," *Computer Journal*, vol.7, no.4, pp. 308-313, 1965.
- [98] W.K. Hastings, "Monte Carlo sampling methods using Markov chains and Their Applications", *Biometrika*, vol. 57, no. 1, pp. 97-109, 1970.
- [99] N. Metropolis, A.W. Rosenbluth, M.N. Rosenbluth, A.H. Teller, and E. Teller, "Equations of state calculations by fast computing machines", *Journal of Chemical Physics*, vol. 21, no. 6, pp. 1087-1092, 1953.
- [100] W. C. Chew and J.H. Lin: "A frequency-hopping approach for microwave imaging of large inhomogeneous bodies," *IEEE Microwave Guided Wave Lett.*, vol. 5, no. 10, pp. 439-442, Dec 1995.
- [101] R. Pierri, R. Persico, and R. Bernini, "Information content of Born field scattered by an embedded slab: Multifrequency, multiview and multifrequency-multiview cases," *J. Opt. Soc. Amer. A*, vol. 16, pp. 2392–2399, 1999.
- [102] M. Lambert, D. Lesselier, and B. J. Kooij, "The retrieval of a buried cylindrical obstacle by a constrained modified gradient method in the H-polarization case and for Maxwellian materials," *Inv. Probl.*, vol. 14, pp. 1265–1283, 1998.
- [103] A. Litman, D. Lesselier, and F. Santosa, "Reconstruction of a two-dimensional binary obstacle by controlled evolution of a level set," *Inv. Probl.*, vol. 14, pp. 685–706, 1998.
- [104] A. G. Tijhuis, K. Belkebir, A. C. S Litman, and B. P. de Hon: "Multiple-

- frequency distorted-wave Born approach to 2D inverse profiling,” *Inv. Probl.*, vol. 17, pp. 1635-1644, 2001.
- [105] L. Song, C. Yu, Q.H Liu, Through-wall imaging (TWI) by radar: “2-D tomographic results and analyses, *IEEE Trans on Geosci. Remote sensing*, vol. 43, no. 12, pp. 2793-2798, Dec. 2005.
- [106] T. Isernia, V. Pascazio, and R. Pierri, “A nonlinear estimation method in tomographic imaging,” *IEEE Trans Geosci. Remote Sensing*, vol. 35, pp. 910–923, 1997.
- [107] J. Baker-Jarvis, M.D. Janezic, B.F. Riddle, R.T. Johnk, P. Kabos, C. L. Holloway, R.G. Geyer, C.A. Grosvenor, “Measuring the permittivity and permeability of lossy materials: solids, liquids, metals, building materials, and negative-index materials,” *NIST Technical Note 1536*.
- [108] A. Robert, “Dielectric permittivity of concrete between 50 MHz and 1 GHz and GPR measurements for building materials evaluation,” *Journal of Applied Geophysics*, vol. 40, pp. 89–94, 1998.
- [109] H. Chiba, Y. Miyazaki, ”Reflection and transmission characteristics of radio waves at a building site due to reinforced concrete slabs,” *Electronics and Communications in Japan (Part I: Communications)*, vol. 81, no. 8, pp. 68–80, 1998.
- [110] H. Chiba, Y. Miyazaki, ”Dependence of radio wave reflection and transmission characteristics of reinforced concrete slabs on frequency and angle of incidence,” *Electronics and Communications in Japan (Part I: Communications)*, vol. 85, no. 1., pp. 69–81, 2002.

- [111] R. H. Cole, J. G. Berberian, S. Mashimo, G. Chryssikos, A. Burns, and E. Tombary, "Time domain reflection methods for dielectric measurements to 10 GHz," *J. Appl. Phys.*, vol. 66, no. 2, July 1989.
- [112] N. E. Hager III, and R. C. Domszy, "Monitoring of cement hydration by broadband time-domain-reflectometry dielectric spectroscopy," *J. Appl. Phys.*, vol. 96, no 9, November 2004.
- [113] T. Chung, C. R. Carter, T. Masliwec, D. G. Manning, "Impulse radar evaluation of concrete, asphalt and waterproofing membrane," *IEEE Transactions on Aerospace and Electronic systems*, vol. 30, no. 2, April 1994.
- [114] H. Zou and T. Hastie, "Regularization and variable selection via the elastic net," *J. R. Statist. Soc. B*, vol. 67, pp. 301–320, 2005.
- [115] M. Grant and S. Boyd, *CVX: Matlab software for disciplined convex programming*, <http://stanford.edu/~boyd/cvx>, June 2009.
- [116] M. Grant and S. Boyd, Graph implementations for nonsmooth convex programs, *Recent Advances in Learning and Control* (a tribute to M. Vidyasagar), V. Blondel, S. Boyd, and H. Kimura, editors, pages 95-110, Lecture Notes in Control and Information Sciences, Springer, 2008.
- [117] P. C. Hansen and D. P. O'Leary, "The use of the L-curve in the regularization of discrete ill-posed problems," *SIAM J. Sci. Comput.*, vol. 14, no. 6, pp. 1487–1503, 1993.
- [118] [www.wipl-d.com](http://www.wipl-d.com).
- [119] P. Russer, *Electromagnetics, microwave circuit and antenna design for communications engineering*, Artech House, 2003.

- [120] M. M. Nikolic, A. Nehorai, and A. R. Djordjevic, "Estimation of direction of arrival using arrays on platforms," to appear in *IEEE Trans. Antennas Propagat.*
- [121] D. W. Batteau, "The role of the pinna in human localization," in *Proc. of the Royal Society of London, Series B, Biological Sciences*, vol. 168, no. 1011, Aug. 1967.
- [122] M. Alvarez-Folgueiras, J.A. Rodriguez-Gonzalez, F. Ares-Pena, "Low-sidelobe patterns from small, low-loss uniformly fed linear arrays illuminating parasitic dipoles," *IEEE Trans. Antennas Propagation*, vol. 57, no. 5, pp. 1584-1586, May 2009.
- [123] S. Chen, A. Hirata, T. Ohira, N.C. Karmakar, "Fast beamforming of electronically steerable parasitic array radiator antennas: theory and experiment," *IEEE Trans. Antennas Propagation*, vol.52, no.7, pp. 1819- 1832, July 2004
- [124] H. Kawakami, T. Ohira, "Electrically steerable passive array radiator (ESPAR) antennas," *IEEE Antennas and Propagation Magazine*, vol. 47, no. 2, pp. 43 - 50, April 2005.
- [125] E. Taillefer, A. Hirata, T. Ohira, "Direction-of-arrival estimation using radiation power pattern with an ESPAR antenna," *IEEE Transactions on Antennas and Propagation*, vol. 53, no. 2, pp. 678 - 684, Feb. 2005.
- [126] T. Svantesson, M. Wennstrom, "High-resolution direction finding using a switched parasitic antenna," *Proceedings of the 11th IEEE Signal Processing Workshop on Statistical Signal Processing*, pp. 508-511, Aug. 2001.
- [127] C.A. Balanis, *Antenna Theory: Analysis and Design*, Wiley, New York,

1997.

[128] [www.the3dstudio.com](http://www.the3dstudio.com)

[129] S. M. Kay, *Fundamentals of Statistical Signal Processing: Estimation Theory*, Prentice Hall PTR, New Jersey, 1993.

[130] H. M. Antia, *Numerical methods for scientists and engineers, Vol. 1*, pp. 160-164, Birkhasuer Verlag, Basel, 2002.

[131] M. Landmann, W. Kotterman, R.S. Thomä, “On the influence of incomplete data models on estimated angular distributions in channel characterization,” *European Conference on Antennas and Propagation, EUCAP*, Edinburgh, November, 2007.

[132] A. Nehorai and E. Paldi, “Vector-sensor array processing for electromagnetic source localization,” *IEEE Transactions on Signal Processing*, vol. 42, no. 2, pp. 376-398, Feb. 1994.

[133] A. Amar and A. J. Weiss, “Fundamental limitations on the resolution of deterministic signals,” *IEEE Transactions on Signal Processing*, vol. 56, no. 11, pp. 5309-5318, Nov. 2008.

# Vitae

## Marija Nikolic

- Date of Birth** June 5, 1976
- Place of Birth** Belgrade, Serbia
- Degrees** Ph.D., Washington University in St. Louis, MO, USA, December 2011.  
Ph.D., School of Electrical Engineering, University of Belgrade, Serbia, September 2007.  
M.Sc., Applied Electromagnetics and Optoelectronics, School of Electrical Engineering, University of Belgrade, Serbia, November 2003.  
Dipl. Ing., Electronics, Telecommunications, and Automatics, School of Electrical Engineering, University of Belgrade, Serbia, November 2000.

## List of Publications

### Journal Papers

- 1.1 Djordjević, A.R., Zajić, A.G., Steković, A.S., **Nikolic, M.M.**, Marićević, Z.A., Schemmann, M.F.C, "On a class of low-reflection transmission-line quasi-Gaussian low-pass filters and their lumped-element approximations," *IEEE Transactions on Microwave Theory and Techniques*, vol. MTT-51, no. 8, pp. 1871-1877, July 2003.
- 1.2 **Nikolic, M.M.**, Djordjević, A., Stefanović, I., Vrhovac, S., Petrović, Z.Lj, "Semi-analytical models of volt-ampere characteristics of diffuse low-current low-pressure discharge," *IEEE Transactions on Plasma Science*, Special issue on the modeling of collisional or near-collisionless low temperature plasmas, vol. 31, no. 4, pp. 717-723, August 2003.

- 1.3 **Nikolic, M.M.**, Djordjević, A.R., Nehorai, A., “Microstrip antennas with suppressed radiation in horizontal directions and reduced coupling,” *IEEE Transactions on Antennas and Propagation*, vol. AP-53, no. 11, pp. 3469-3476, November 2005.
- 1.4 **Nikolic, M.M.**, Ortner, M., Nehorai, A., Djordjevic, A.R., “An approach to estimating building layouts using radar and jump-diffusion algorithm,” *IEEE Transactions on Antennas and Propagation*, Vol. 57, No. 3, March 2009, pp. 768-776.
- 1.5 **Nikolic, M.M.**, Nehorai, A., Djordjevic, A.R., “Estimating moving targets behind reinforced walls using radar,” *IEEE Transactions on Antennas and Propagation*, Vol. 57, No. 11, Nov 2009, pp. 3530-3538.
- 1.6 **Nikolic, M.M.**, Nehorai, A., Djordjevic, A.R., “Estimation of direction of arrival using arrays on platforms,” to appear in *IEEE Trans. Antennas Propagat.*
- 1.7 **Nikolic, M.M.**, Nehorai, A., Djordjevic, A.R., “Electromagnetic imaging of hidden 2D PEC targets using sparse signal modeling,” in revision for *IEEE Trans. Geosci. Remote Sensing*.

#### **Software**

- 2.1 **Nikolic, M.M.**, Djordjević, A.R., Nikolić, M.M., ES3D: Electrostatic field solver for multilayer circuits, Artech House, Boston, 2007.

#### **Conference Papers**

- 3.1 **Nikolic, M.M.**, Djordjević, A.R., “Coupling among collocated loops,” *Proc. of EuCAP*, Nice, November 2006.
- 3.2 **Nikolic, M.M.**, Djordjević, A.R., “Improving radiation pattern of microstrip Antennas,” *Proc. of EuCAP*, Nice, November 2006.
- 3.3 **Nikolic, M.M.**, Nehorai, A., and Djordjević, A.R., “Estimating distributed objects inside buildings by moving sensors,” *Proc. of ACES 2007*, pp. 409-414, Verona, Italy, March 2007.
- 3.4 **Nikolic, M.M.**, Nehorai, A., Djordjević, A.R., “Radar estimation of building layout estimation using jump-Diffusion,” *Proc. 2nd IEEE Int. Workshop on Computational Advances in Multi-Sensor Adaptive Processing*, St. Thomas, U.S. Virgin Islands, Dec. 2007.
- 3.5 **Nikolic, M.M.**, Nehorai, A., Djordjevic, A.R., “Exploiting multipath from airborne platform for direction of arrival estimation”, *Proc. of EuCAP*, pp. 3131-3135, Berlin, Germany, 23-27 March 2009.
- 3.6 **Nikolic, M.M.**, Nehorai, A., Djordjević, A.R., “Sparse electromagnetic imaging,” *Proc. of EuCAP*, April 11-15, Rome, Italy, 2011.
- 3.7 **Nikolic, M.M.**, Nehorai, A., Djordjević, A.R., “Electromagnetic imaging of hidden 2D PEC targets using sparse signal modeling,” *Proc. of USNC/URSI*, Spokane, WA, July 3-8, 2011.
- 3.8 **Nikolic, M.M.**, Nehorai, A., Djordjević, A.R., “Biologically inspired sensing on UAV platform,” *Proc. of USNC/URSI*, Spokane, WA, July 3-8, 2011.

